JASMINE: Near-infrared astrometry and time-series photometry science

Daisuke Kawata [1,2,*] Hajime Kawahara [3,4] Naoteru Gouda [1,5] Nathan J. Secrest [6]
Ryouhei Kano [1,3] Hirokazu Kataza [1,3] Naoki Isobe [3] Ryou Ohsawa [1] Fumihiko Usui [3]
Yoshiyuki Yamada [7] Alister W. Graham [8] Alex R. Pettitt [9] Hideki Asada [10] Junichi Baba [1,11]
Kenji Bekki [12] Bryan N. Dorland [6] Michiko Fujii [4] Akihiko Fukui [13] Kohei Hattori [1,14]
Teruyuki Hirano [15] Takafumi Kamizuka [16] Shingo Kashima [1] Norita Kawanaka [17]
Yui Kawashima [3,18] Sergei A. Klioner [19] Takanori Kodama [20] Naoki Koshimoto [21,22]
Takayuki Kotani [5,15] Masayuki Kuzuhara [15] Stephen E. Levine [23,24] Steven R. Majewski [25]
Kento Masuda [26] Noriyuki Matsunaga [4] Kohei Miyakawa [1] Makoko Miyoshi [1]
Kumiko Morihana [27] Ryoichi Nishi [28] Yuta Notsu [29,30] Masashi Omiya [15] Jason Sanders [31]
Ataru Tanikawa [32] Masahiro Tsujimoto [3] Taihei Yano [1] Masataka Aizawa [33]
Ko Arimatsu [34] Michael Biermann [35] Celine Boehm [36] Masashi Chiba [37] Victor P. Debattista [38]
Ortwin Gerhard [39] Masayuki Hirabayashi [1] David Hobbs [40] Bungo Ikenoue [1] Hideyuki Izumiura [41]
Carme Jordi [42,43,44] Naoki Kohara [1] Wolfgang Löffler [35] Xavier Luri [42,43,44] Ichiro Mase [1]
Andrea Miglio [45,46] Kazuhisa Mitsuda [1] Trent Newswander [47] Shogo Nishiyama [48]
Yoshiyuki Obuchi [1] Takafumi Ootsubo [1] Masami Ouchi [1,49,50] Masanobu Ozaki [1]
Michael Perryman [51] Timo Prusti [52] Pau Ramos [1] Justin I. Read [53] R. Michael Rich [54]
Ralph Schönrich [2] Minori Shikauchi [55,56] Risa Shimizu [1] Yoshinori Suematsu [1] Shotaro Tada [5]
Aoi Takahashi [15] Takayuki Tatekawa [57,58] Daisuke Tatsumi [1] Takuji Tsujimoto [1] Toshihiro Tsuzuki [1]
Seitaro Urakawa [59] Fumihiro Uraguchi [1] Shin Utsunomiya [1] Vincent Van Eylen [2]
Floor van Leeuwen [60] Takehiko Wada [1] and Nicholas A. Walton [60]

1 National Astronomical Observatory of Japan, 2-21-1 Osawa, Mitaka, Tokyo 181-8588, Japan
2 Mullard Space Science Laboratory, University College London, Holmbury St Mary, Dorking, Surrey RH5 6NT, UK
3 Institute of Space and Astronautical Science, Japan Aerospace Exploration Agency, 3-1-1 Yoshinodai, Chuo-ku, Sagamihara, Kanagawa 252-5210, Japan
4 Department of Astronomy, Graduate School of Science, The University of Tokyo, 7-3-1 Hongo, Bunkyo-ku, Tokyo 113-0033, Japan
5 Astronomical Science Program, Graduate Institute for Advanced Studies, SOKENDAI, 2-21-1 Osawa, Mitaka, Tokyo 181-1855 Japan
6 US Naval Observatory, 3450 Massachusetts Ave NW, Washington, DC 20392-5420, USA
7 Department of Physics, Kyoto University, Kitashirakawa-oiwake-cho, Sakyo-ku, Kyoto, Kyoto 606-8502, Japan
8 Centre for Astrophysics and Supercomputing, Swinburne University of Technology, Hawthorn, VIC 3122, Australia
9 Department of Physics and Astronomy, California State University, Sacramento, 6000 J Street, Sacramento, CA 95819-6041, USA
10 Graduate School of Science and Technology, Hirosaki University, Aomori 036-8561, Japan
11 Graduate School of Science and Engineering, Kagoshima University, 1-21-35 Korimoto, Kagoshima, Kagoshima 890-0065, Japan
12 International Centre for Radio Astronomy Research, The University of Western Australia, 7 Fairway, Crawley, WA 6009, Australia
13 Department of Earth and Planetary Science, Graduate School of Science, The University of Tokyo, 7-3-1 Hongo, Bunkyo-ku, Tokyo 113-0033, Japan
14 Institute of Statistical Mathematics, 10-3 Midoricho, Tachikawa, Tokyo 190-8562, Japan
15 Astrobiology Center, 2-21-1 Osawa, Mitaka, Tokyo 181-8588, Japan
16 Institute of Astronomy, Graduate School of Science, The University of Tokyo, 2-21-1 Osawa, Mitaka, Tokyo 181-0015, Japan
17 Center for Gravitational Physics and Quantum Information, Yukawa Institute for Theoretical Physics, Kyoto University, Kitashirakawa-oiwake-cho, Sakyo-ku, Kyoto, Kyoto 606-8502, Japan
18 Cluster for Pioneering Research, RIKEN, 2-1 Hirosawa, Wako, Saitama 351-0198, Japan
19 Lohrmann Observatory, Technische Universität Dresden, 01062 Dresden, Germany
20 Earth-Life Institute (ELSI), Tokyo Institute of Technology, 2-12-1 Ookayama, Meguro, Tokyo 152-8550, Japan
21 Code 667, NASA Goddard Space Flight Center, Greenbelt, MD 20771, USA
22 Department of Astronomy, University of Maryland, College Park, MD 20742, USA
23 Lowell Observatory, 1400 W Mars Hill Rd, Flagstaff, AZ 86001, USA

[24] Massachusetts Institute of Technology, Department of Earth, Atmospheric and Planetary Sciences, 77 Massachusetts Ave., Cambridge, MA 02139, USA

[25] Department of Astronomy, University of Virginia, PO Box 400325, Charlottesville, VA 22904-4325, USA

[26] Department of Earth and Space Science, Osaka University, 1-1 Machikaneyama, Toyonaka, Osaka 560-0043, Japan

[27] Subaru Telescope, National Astronomical Observatory of Japan, Hilo, HI 96720, USA

[28] Department of Physics, Niigata University, 8050 Ikarashi-2, Nishi-ku, Niigata, Niigata 950-2181, Japan

[29] Laboratory for Atmospheric and Space Physics, University of Colorado Boulder, 3665 Discovery Drive, Boulder, CO 80303, USA

[30] National Solar Observatory, University of Colorado Boulder, 3665 Discovery Drive, Boulder, CO 80303, USA

[31] Department of Physics and Astronomy, University College London, London WC1E 6BT, UK

[32] Department of Earth Science and Astronomy, College of Arts and Sciences, The University of Tokyo, 3-8-1 Komaba, Meguro-ku, Tokyo 153-8902, Japan

[33] Tsung-Dao Lee Institute, Shanghai Jiao Tong University, Shengrong Road 520, 201210 Shanghai, China

[34] The Hakubi Center/Astronomical Observatory, Graduate School of Science, Kyoto University, Kitashirakawa-oiwake-cho, Sakyo-ku, Kyoto, Kyoto 606-8502, Japan

[35] Astronomisches Rechen-Institut, Zentrum für Astronomie der Universität Heidelberg, Mönchhofstr. 12–14, 69120 Heidelberg, Germany

[36] School of Physics, Faculty of Science, University of Sydney, NSW 2006, Australia

[37] Astronomical Institute, Tohoku University, Aoba-ku, Sendai, Miyagi 980-8578, Japan

[38] Jeremiah Horrocks Institute, University of Central Lancashire, Preston PR1 2HE, UK

[39] Max-Planck-Institut für extraterrestrische Physik, Giessenbachstraße, 85748 Garching, Germany

[40] Lund Observatory, Division of Astrophysics, Department of Physics, Lund University, Box 43, SE-221 Lund, Sweden

[41] Subaru Telescope Okayama Branch, National Astronomical Observatory of Japan, National Institutes of Natural Sciences, Honjo 3037-5, Kamogata, Asakuchi, Okayama 719-0232, Japan

[42] Institut de Ciències del Cosmos (ICCUB), Universitat de Barcelona (UB), Martí i Franquès 1, E-08028 Barcelona, Spain

[43] Departament de Física Quàntica i Astrofísica (FQA), Universitat de Barcelona (UB), Martí i Franquès 1, E-08028 Barcelona, Spain

[44] Institut d'Estudis Espacials de Catalunya (IEEC), c. Gran Capità, 2-4, 08034 Barcelona, Spain

[45] Dipartimento di Fisica e Astronomia "Augusto Righi", Università di Bologna, via Gobetti 93/2, 40129 Bologna, Italy

[46] INAF-Osservatorio di Astrofisica e Scienza dello Spazio di Bologna, via Gobetti 93/3, 40129 Bologna, Italy

[47] Utah State University Space Dynamics Laboratory, 416 East Innovation Avenue, North Logan, UT 84341, USA

[48] Miyagi University of Education, Aoba-ku, Sendai, Miyagi 980-0845, Japan

[49] Institute for Cosmic Ray Research, The University of Tokyo, 5-1-5 Kashiwanoha, Kashiwa, Chiba 277-8582, Japan

[50] Kavli Institute for the Physics and Mathematics of the Universe (Kavli IPMU, WPI), The University of Tokyo, 5-1-5 Kashiwanoha, Kashiwa, Chiba 277-8583, Japan

[51] School of Physics, University College Dublin, Belfield, Dublin 4, Ireland

[52] European Space Agency (ESA), European Space Research and Technology Centre (ESTEC), Keplerlaan 1, 2201 AZ Noordwijk, The Netherlands

[53] Department of Physics, University of Surrey, Guildford GU2 7XH, UK

[54] Department of Physics and Astronomy, University of California, Los Angeles, LA, CA 90095-1547, USA

[55] Department of Physics, The University of Tokyo, 7-3-1 Hongo, Bunkyo, Tokyo 113-0033, Japan

[56] Research Center for the Early Universe (RESCEU), The University of Tokyo, 7-3-1 Hongo, Bunkyo, Tokyo 113-0033, Japan

[57] National Institute of Technology (KOSEN), Kochi College, 200-1 Monobe, Nankoku, Kochi 783-8508, Japan

[58] Waseda Research Institute for Science and Engineering, Waseda University, 3-4-1 Okubo, Shinjuku, Tokyo 169-8555, Japan

[59] Japan Spaceguard Association, Bisei Spaceguard Center 1716-3 Okura, Bisei, Ibara, Okayama 714-1411, Japan

[60] Institute of Astronomy, University of Cambridge, Madingley Road, Cambridge CB3 0HA, UK

*Email: d.kawata@ucl.ac.uk

Abstract

The Japan Astrometry Satellite Mission for INfrared Exploration (JASMINE) is a planned M-class science space mission by the Institute of Space and Astronautical Science, the Japan Aerospace Exploration Agency. JASMINE has two main science goals. One is Galactic archaeology with a Galactic Center survey, which aims to reveal the Milky Way's central core structure and formation history from Gaia-level ($\sim$25 μas) astrometry in the near-infrared (NIR) $H_{\rm w}$ band (1.0–1.6 μm). The other is an exoplanet survey, which aims to discover transiting Earth-like exoplanets in the habitable zone from NIR time-series photometry of M dwarfs when the Galactic Center is not accessible. We introduce the mission, review many science objectives, and present the instrument concept. JASMINE will be the first dedicated NIR astrometry space mission and provide precise astrometric information on the stars in the Galactic Center, taking advantage of the significantly lower extinction in the NIR. The precise astrometry is obtained by taking many short-exposure images. Hence, the JASMINE Galactic Center survey data will be valuable for studies of exoplanet transits, asteroseismology, variable stars, and microlensing studies, including discovery of (intermediate-mass) black holes. We highlight a swath of such potential science, and also describe synergies with other missions.

Keywords: astrometry — Galaxy: Center — infrared: planetary systems — space vehicles: instruments — techniques: photometric

1 Introduction

Since the discovery that the Galaxy is one among hundreds of billions in a vast cosmic web—a gravitational framework set in place at the very first moments of the universe—it has been understood that it is an ancient record, carrying within it the products and imprints of the physics of the universe and the processes that eventually resulted in our Sun, Earth, and life itself. The near-infrared (NIR) astrometry space mission, the Japan Astrometry Satellite Mission for INfrared Exploration (JASMINE)[1] (figure 1; Gouda 2011), has been selected for an M-class space mission by the Institute of Space and

---

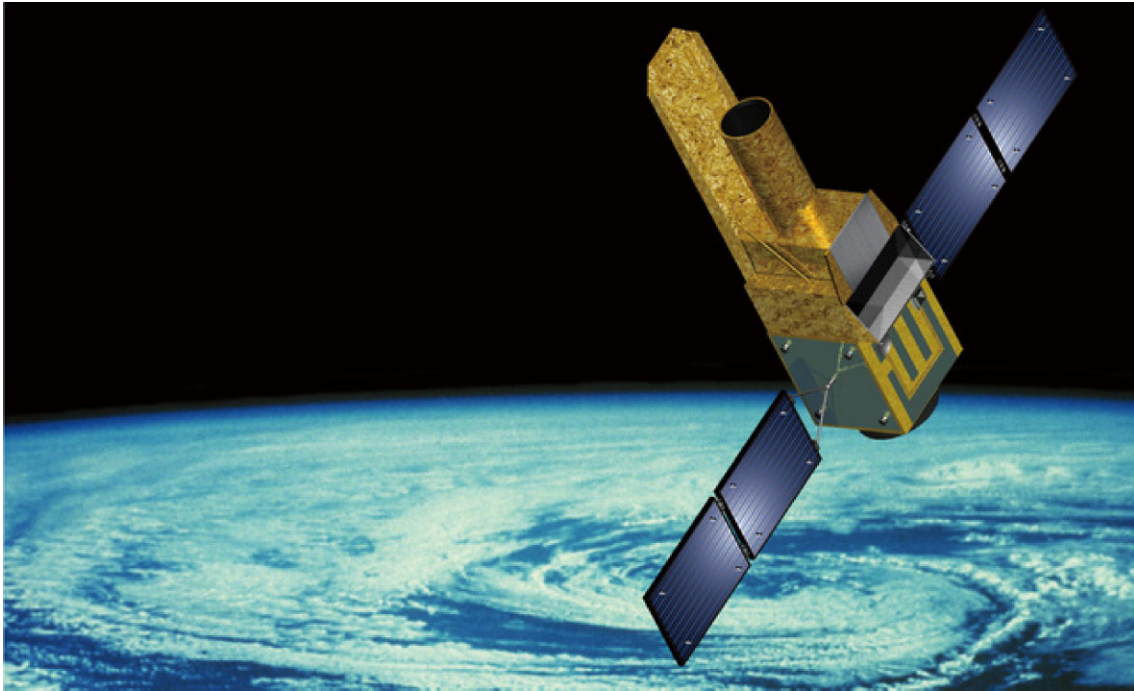[1] The JASMINE mission detailed in this paper was originally known as Small-JASMINE in previous documentation, but is now simply referred to as JASMINE (http://jasmine.nao.ac.jp/index-en.html).

Fig. 1. Artist's impression of JASMINE.

Astronautical Science (ISAS), the Japan Aerospace Exploration Agency (JAXA), with a planned launch in 2028. JASMINE has two main science goals. One is to decipher the ancient stellar fossil record: to reveal the Milky Way's central core structure and its formation history from Gaia-level ($\sim$25 μas) astrometry in the NIR H_w band [1.0–1.6 μm, $H_w \approx 0.9J + 0.1H - 0.06(J - H)^2$]. This is referred to as the Galactic Center survey (GCS), spanning 2.52 deg^2. The other goal is an exoplanet survey (EPS) to discover Earth-like habitable exoplanets from the NIR time-series photometry of M dwarf transits, obtained when the Galactic Center is not accessible to JASMINE. JASMINE will be the first dedicated NIR astrometry space mission and will provide precise astrometric information on the stars in the Galactic Center, taking advantage of the significantly lower extinction in the NIR band than in the visual band. The precise astrometry is obtained by taking many short-exposure ($\sim$12.5 s) images. Hence, JASMINE can also provide time-series NIR photometry data in addition to precise astrometry. The aim of this paper is to describe the novel science opened up by the unique new capabilities of the JASMINE mission.

1.1 Gaia revolution and next step: NIR astrometry

The European Space Agency's Gaia mission (launched in 2013, Gaia Collaboration 2016) made its second data release (DR2, Gaia Collaboration 2018a) in 2018 April, followed by a third data release (EDR3 in 2020 and DR3 in 2022, Gaia Collaboration 2021, 2023), which provided measurements of the positions, motions, and photometric properties for more than one billion stars with unprecedented precision. Gaia DR2 and DR3, in combination with ground-based spectroscopic surveys, such as the RAdial Velocity Experiment (RAVE, Steinmetz et al. 2006), the Sloan Digital Sky Survey (SDSS), the Sloan Extension for Galactic Understanding and Exploration (SEGUE, Yanny et al. 2009), the Apache Point Obser-

vatory Galactic Evolution Experiment (APOGEE, Majewski et al. 2017), the Large Sky Area Multi-Object Fiber Spectroscopic Telescope (LAMOST, Zhao et al. 2012), the Gaia-ESO survey (Gilmore et al. 2012), and the Galactic Archaeology with HERMES survey (GALAH, Martell et al. 2017), have revolutionized our view of the Galactic disk and halo, including their various stellar streams and the impact of satellite galaxies, and the interplay between the disks and stellar and dark halos.

For the Galactic disk, Gaia enabled us to analyze the 6D phase-space distribution (position, proper motion, radial velocity, parallax) of large samples of stars within a few kpc of the Sun for the first time, and revealed that the Galactic disk is heavily perturbed (Gaia Collaboration 2018b; Antoja et al. 2018; Kawata et al. 2018; Bland-Hawthorn et al. 2019b). These fine kinematic structures have provided insight into the origin of the spiral structure, possibly transient (e.g., Baba et al. 2018; Hunt et al. 2018, 2019), and the pattern speed of the bar, including the possibility of it slowing down (e.g., Monari et al. 2019b; Chiba & Schönrich 2021). In addition, the discovery of phase-space features correlating in and out of plane motion of the disk stars (e.g., Antoja et al. 2018; Hunt et al. 2022) opened up a heated discussion of the origin of these features, which have been attributed to various causes including: phase mixing after a tidal perturbation by a dwarf galaxy passing through the Galactic plane (e.g., Binney & Schönrich 2018; Laporte et al. 2019), bar buckling (Khoperskov et al. 2019), and/or a persistent dark matter wake (Grand et al. 2023).

Regarding the stellar Galactic halo, Gaia and ground-based spectroscopic data have revealed that a significant fraction of halo stars are moving on very radial orbits. This has been interpreted as a remnant of a relatively large galaxy, the so-called Gaia–Sausage–Enceladus, falling into the Milky Way about 10 Gyr ago (Belokurov et al. 2018; Helmi et al. 2018; Di Matteo et al. 2019; Gallart et al. 2019). This merger is

considered to have disrupted the proto-Galactic disk and created the inner metal-rich halo stars, which are suggested to be of the same population as the thick disk (Di Matteo et al. 2019; Gallart et al. 2019; Belokurov et al. 2020).

Future Gaia data releases will undoubtedly yield further discoveries pertaining to the Galactic disk and halo structures and provide an even deeper insight into the formation and evolution history of the Milky Way. However, due to the high dust extinction in the optical band where Gaia operates (∼0.6 μm), Gaia cannot provide reliable astrometry for stars near the Galactic nucleus. This is an unfortunate hindrance, as this is where the history of the first structure and the formation of the super-massive black hole (SMBH) of the Galaxy should be imprinted. The JASMINE GCS targets the Galactic Center field (spanning a projected Galactocentric radius of $R_{GC} \lesssim 100$ pc). JASMINE is designed to achieve Gaia-level astrometric accuracy toward the Galactic Center in the NIR H_w band. The JASMINE GCS will provide precise astrometric information on the stars in the Galactic Center. In this survey, for objects brighter than $H_w = 12.5$ mag, JASMINE will achieve a parallax accuracy of $\sigma_\pi \sim 25$ μas and a proper motion accuracy of $\sigma_\mu \sim 25$ μas yr^{-1}. JASMINE plans to downlink the data for all stars brighter than $H_w = 14.5$ mag. For stars as bright as $H_w = 14.5$ mag, JASMINE will achieve an accuracy of $\sigma_\mu = 125$ μas yr^{-1}. Section 2 describes the scientific details of the JASMINE GCS.

1.2 Habitable zone exoplanet search

A major ambition of modern astronomy is to identify the biosignatures of terrestrial exoplanets located in habitable zones (HZ). Directly imaged planets and transiting planets are the two primary targets for the astrobiological exploration of exoplanets. The space-based direct imaging missions, HabEx (Gaudi et al. 2020) and LUVOIR (The LUVOIR Team 2019) and its successor LUVEX (National Academies of Sciences, Engineering, & Medicine 2021), are capable of searching for metabolic gas biosignatures in the atmospheres of planets orbiting solar-type stars. The James Webb Space Telescope (JWST) and subsequent planned missions with larger telescopes, such as LUVEX, will characterize terrestrial planet atmospheres using stable low-dispersion spectroscopy of transiting exoplanets (e.g., Lustig-Yaeger et al. 2019). Extremely large ground-based telescopes, such as the Thirty Meter Telescope (TMT), the Giant Magellan Telescope (GMT), and the European Extremely Large Telescope (E-ELT), will search for biosignatures using transmission spectroscopy (e.g., Snellen et al. 2013; Rodler & López-Morales 2014) and direct imaging spectroscopy (e.g., Kawahara et al. 2012; Crossfield 2013) of terrestrial planets around late-type stars. There are also plans to use the UV spectrograph on the World Space Observatory-Ultraviolet (WSO-UV) and Life-environmentology, Astronomy, and PlanetarY Ultraviolet Telescope Assembly (LAPYUTA) to search for the atomic oxygen (O I) line (130 nm), a potential biosignature, in the upper atmosphere of terrestrial transiting exoplanets orbiting late-type stars (e.g., Tavrov et al. 2018).

The future exploration of terrestrial planet atmospheres relies crucially on identifying suitable targets prior to characterization. Among transiting planets, those in the HZ around late-type stars are best suited for two reasons. First, the HZ planets around low-luminosity, late-type stars have much shorter orbital periods than the Earth. This makes it more

plausible to find them via the transit method in the first place, and it also allows multiple monitorings of their transits. Secondly, the small radius of late-type stars deepens the transit signal compared to Sun-like stars. Various efforts have been made to detect terrestrial planets transiting late-type dwarfs, from both the ground and space. Several planets in the HZ of an ultra-cool dwarf, TRAPPIST-1, are good examples of transiting terrestrial planets that are ideal for further atmospheric characterization (Gillon et al. 2017). NASA's Spitzer telescope determined that the Earth-like planets of the TRAPPIST-1 system lie in the HZ. Unfortunately, the Spitzer mission terminated in 2020 January, removing a key instrument from the exoplanet community's toolbox. The Transiting Exoplanet Survey Satellite (TESS, Ricker et al. 2014) is an all-sky survey that discovered a similar planet around an early M dwarf, TOI-700d and e (Gilbert et al. 2020, 2023). With its 10.5 cm diameter camera apertures, TESS is mainly suited for targeting bright early-to-mid M dwarfs. In contrast, ground-based surveys, such as MEarth (Irwin et al. 2009), TRAPPIST, and SPECULOOS (Delrez et al. 2018), take advantage of their larger telescope aperture to find terrestrial planets around ultra-cool dwarfs with even later spectral types.

In summer and winter,[2] the NIR and high-cadence time-series photometry capability of JASMINE will be used to conduct an exoplanet transit survey, which aims to fill a gap in TESS and ground-based surveys. The NIR photometry capability of JASMINE is similar to that of Spitzer and offers long-term (a few weeks) follow-up transit observations of exoplanet systems discovered by TESS and ground-based surveys. This allows for the detection of outer orbiting planets that could be in the HZ. The scientific goals and strategies of the exoplanet transit survey are described in section 3, including other potential ways of finding exoplanets using microlensing and astrometry in the GCS field.

1.3 The JASMINE mission

To achieve these main science objectives of the Galactic Center archaeology survey and the exoplanet survey, JASMINE will have a scientific payload with a 36 cm aperture telescope with a single focal plane. JASMINE will provide photometric observations within a 1.0–1.6 μm passband over a field of view (FoV) of $0°.55 \times 0°.55$. JASMINE will orbit the Earth in a temperature-stable Sun-synchronous orbit. Figure 1 shows an artist's impression of the spacecraft. The telescope structure is made of Super-Super Invar alloy (Ona et al. 2020). A large Sun shield and telescope hood are installed to maintain thermal stability. The satellite is expected to be launched aboard a JAXA Epsilon S Launch Vehicle from the Uchinoura Space Center in Japan in 2028. More detailed instrumental specifications and survey strategies of the mission are provided in section 4.

The unique NIR astrometric and time-series photometric capabilities of JASMINE are applicable to other science targets and the unique data from the JASMINE GCS will be valuable for a wide range of scientific topics. In section 5, we summarize some examples of science cases to utilize the data from JASMINE. Section 6 summarizes the potential synergies with other relevant projects operating

---

[2] JASMINE can observe the Galactic Center field only in spring and fall, because the Sun is aligned in the same direction as the Galactic Center in Northern Hemisphere winter. In Northern Hemisphere summer, it is prohibitively difficult for the satellite to meet the required thermal conditions for precision astrometry.

when JASMINE launches. Finally, section 7 provides a brief summary of the paper.

2 Galactic Center survey (GCS): Galactic Center archaeology

At the heart of the Galaxy, the Galactic Center, lies an SMBH with a mass of $(4.297 \pm 0.013) \times 10^6 \, M_\odot$ (GRAVITY Collaboration 2021), the origin of which remains an area of intense study in modern astrophysics. What is known is that the masses, M_{BH}, of SMBHs correlate with the stellar mass, concentration, and velocity dispersion, $\sigma_\star$, of their host bulge (Magorrian et al. 1998; Ferrarese & Merritt 2000; Gebhardt et al. 2000; Graham et al. 2001), and there is an emerging dependence on the host galaxy morphology (Graham & Sahu 2023a, 2023b). The initial relationships were unexpected because the gravitational sphere of influence of the SMBH has a radius of the order of ∼1 pc, thousands of times smaller than the scale of the Galactic bulge (for reviews, see Kormendy & Ho 2013; Graham 2016a and references therein).

From the turn of the millennium when the initial correlations were discovered, it has arguably been the singular unifying focus of research on SMBHs and galaxies. It is slowly coming to be understood as resulting from an interplay between periods of baryonic mass accretion on to the SMBH and neighboring stellar populations, and the "feedback" from the resultant active galactic nucleus (AGN) activity (King & Pounds 2015), a process that may have started at the earliest epochs (e.g., Shen et al. 2015). Indeed, the existence of SMBHs at redshifts exceeding 7.5 (Bañados et al. 2018), when the universe was barely 500 million years old, implies that much cosmic history may be imprinted upon the environment of the Galactic Center, motivating Galactic archaeology (Freeman & Bland-Hawthorn 2002) at the Galactic Center. While it is now apparent that major "dry" mergers have established the bulge–black hole (BH) scaling relations in elliptical galaxies (Graham & Sahu 2023a; Graham 2023a), with AGN feedback relegated to a maintenance role (Benson et al. 2003), the new morphology-aware scaling relations have recently revealed how accretion and minor mergers have likely built spiral galaxies from lenticular galaxies (Graham 2023b). Indeed, it is not just the Milky Way that shows evidence of disrupted satellites (e.g., Javanmardi et al. 2016; Mao et al. 2021). Moreover, some of these satellites may be delivering massive BHs into the spiral galaxies, possibly evidenced by the X-ray point source in the disrupted Nikhuli system captured by NGC 4424 (Graham et al. 2021a).

Galactic Center archaeology has been a distinctly multi-wavelength field. The highest-energy observations have appropriately revealed the most conspicuous evidence of past AGN activity from the SMBH of the Milky Way, Sagittarius A* (Sgr A*), in the form of the Fermi bubble. The Fermi bubble is seen in γ-rays, which extend to ∼10 kpc and are considered to be due to AGN activity several Myr ago (Guo & Mathews 2012; Fox et al. 2015), although the origin of the bubble is still in debate and a star formation driven bubble (e.g., Crocker & Aharonian 2011; Sarkar et al. 2015; Nogueras-Lara et al. 2019) is also a possible origin. The X-rays likewise implicate past AGN activity, such as the presence of Fe Kα ($h\nu = 6.4$ keV) fluorescence at the interfaces of cold molecular regions in the vicinity of Sgr A* (e.g., Ponti et al. 2010, 2013, Clavel et al. 2013), or the presence of a hot-gas cavitation, symmetric about Sgr A*, extending out to several kpc (Nicastro et al. 2016; Predehl et al. 2020). These "light echos" are also seen at lower energies (Sofue & Handa 1984; Tsuboi et al. 1985; Bland-Hawthorn & Cohen 2003), with Hα emission seen in the Magellanic Stream requiring an illumination by UV ionizing photons generally only possible from AGNs (Bland-Hawthorn et al. 2013, 2019a).

From visual to NIR wavelengths, Galactic Center archaeology studies have been focused predominantly on the history and makeup of the Galaxy's stellar populations. Several key parameters, such as the stellar chemical abundances, e.g., [Fe/H] and [α/Fe]], surface gravities, effective temperatures, and kinematics, are of interest to these studies. Although there are many optical photometric and spectroscopic surveys of stars in the central region of the Galaxy, because of the extremely high extinction at optical wavelengths, the optical surveys tend to avoid the Galactic Center and focus instead on the global properties of the bulge/bar. To study the Galactic Center, NIR observations are crucial. For example, photometric data from the IRSF/Simultaneous InfraRed Imager for Unbiased Surveys (SIRIUS, Nagayama et al. 2003; Nishiyama et al. 2006), the Two Micron All Sky Survey (2MASS, Skrutskie et al. 2006), VISTA Variables in the Via Lactea (VVV, Minniti et al. 2010), and GALACTICNUCLEUS (Nogueras-Lara et al. 2018) revealed the detailed stellar structure of the Galactic Center, including the nuclear star cluster (NSC, subsection 2.1) and nuclear stellar disk (NSD: subsection 2.3). Meanwhile, the APOGEE spectroscopic survey, with its NIR (1.51–1.70 μm) high spectral resolution ($R \sim 22500$), has been critical for understanding the chemical makeup of stellar populations in the Galaxy, as well as providing line-of-sight velocities. Results from APOGEE include kinematical and structural differentiation between metal-poor and metal-rich stars in the inner Galaxy (Zasowski et al. 2016; García Pérez et al. 2018; Wylie et al. 2021), detailed chemical abundances (Zasowski et al. 2019), signatures of the central bar (Nidever et al. 2012; Queiroz et al. 2021), and measuring the rotation of both the bulge (Ness et al. 2016a) and the NSD (Schönrich et al. 2015), which may extend to kpc scales in size (Debattista et al. 2015, 2018). Recently, using the K-band Multi-Object Spectrograph (KMOS) on the Very Large Telescope (VLT), Fritz et al. (2021) surveyed the stars in the NSD, and analyzed their line-of-sight velocities and metallicities. Schultheis et al. (2021) found that the NSD is kinematically cold, and that more metal-rich stars are kinematically colder. The presence of the NSD in other galaxies has been used to infer the longevity of galaxy bars and their role in transporting gas to the innermost regions (Gadotti et al. 2015, 2019; see also subsection 2.4).

However, while there has been an explosion of archaeological studies of the Galactic Center as a result of these and other new facilities and methods to exploit line-of-sight velocities and chemical abundances to access relic stellar signatures that tell the history of the Galaxy formation, high-precision proper motions and parallaxes—critical to providing the remaining three dimensions of phase space needed for mapping the gravitational potential of the Galactic Center—have thus far been unavailable. This is because the Galactic Center can exhibit upwards of 30–60 mag extinction at visual wavelengths (e.g., Fritz et al. 2011), precluding the use of Gaia data. JASMINE will close this gap by mapping the positions, motions, and parallaxes of stars in the NIR H_w band, where the extinction is much lower, i.e., of the order of $A_{H_w} \sim 5$–6 mag
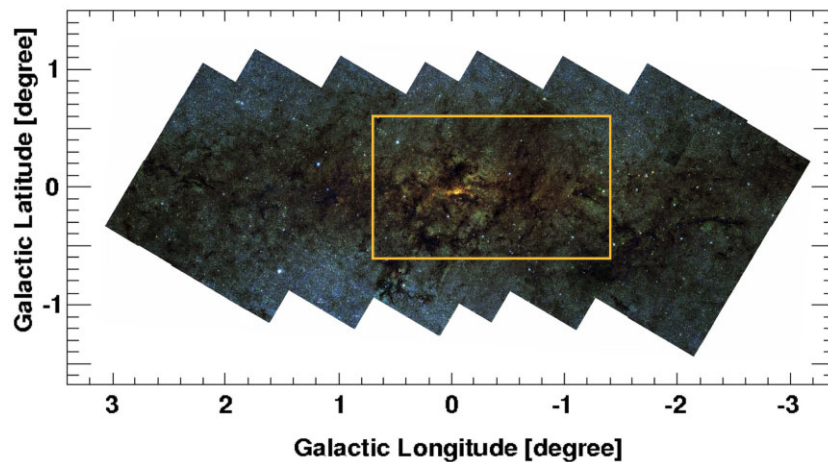
Fig. 2. Planned survey area of the JASMINE GCS program (highlighted with a yellow open square) overlaid on an the image of the SIRIUS survey (Nishiyama et al. 2006).

(e.g., Fritz et al. 2011; Gonzalez et al. 2013; Nogueras-Lara et al. 2021).

The GCS of JASMINE will provide the parallax and proper motion of stars in a Galactic Center field defined by a rectangular region of $-1°.4 < l < 0°.7$ and $-0°.6 < b < 0°.6$. Note that $0°.7$ corresponds to about 100 pc at the distance of the Galactic Center. This survey region is still subject to change, and may become $-0°.7 < l < 1°.4$ and $-0°.6 < b < 0°.6$, i.e., shifting toward the positive longitude without changing the size of the survey area, depending on the scientific values and operation and/or data analysis requirements. In this paper, unless otherwise stated, we consider the region of $-1°.4 < l < 0°.7$ and $-0°.6 < b < 0°.6$ as highlighted in figure 2. Within this main survey area, JASMINE is expected to produce accurate positions and proper motions for about 120000 stars up to $H_w < 14.5$ mag, including about 68000 Galactic Center stars.[3]

The proper motion accuracy achieved by JASMINE for bright stars with $H_w < 12.5$ mag is expected to be about 25 μas yr^{-1}, and the proper motion accuracy for the faintest stars with $H_w = 14.5$ mag is expected to be about 125 μas yr^{-1}. These accuracies respectively correspond to transverse velocity accuracies of ~ 0.98 km s^{-1} and ~ 4.9 km s^{-1} at the distance of the Galactic Center. Recently, careful analysis of long-timespan, NIR, ground-based imaging data has yielded sub-mas yr^{-1} proper motion accuracy. For example, the VVV InfraRed Astrometry Catalogue (VIRAC, Smith et al. 2018) reaches a mode in the proper motion uncertainty distribution of 0.3 mas yr^{-1} in version 2 of VIRAC (Sormani et al. 2022). However, the systematic uncertainties of the ground-based data are difficult to quantify due to atmospheric effects, the distortion of telescope optics, and detector deformation, which are not well controlled. JASMINE will provide independent and improved measurements of proper motion from space, as well as a critical NIR reference frame for the Galactic Center region, which will be a valuable asset in improving the proper motion accuracy for these legacy ground-based data. In addition, for bright stars with $H_w < 12.5$ mag JASMINE will provide precise parallax measurements with an accuracy of ~ 25 μas. This corresponds to

$\sim 20\%$ accuracy of the parallax distance for the stars in the Galactic Center, which enables us to identify the Galactic Center stars less ambiguously. These unique distance confirmations using trigonometric parallaxes will provide a critical verification of the color selection methods that are currently most predominantly used to create samples of Galactic Center stars.

This section summarizes the science objectives of the GCS. The section is organized by increasing physical scale, from parsec-scale dynamics of the nuclear star cluster in subsection 2.1 to kiloparsec-scale dynamics of the Galactic bar, bulge, and inner disk in subsection 2.6. Note that at a Galactic Center distance of 8.275 kpc (GRAVITY Collaboration 2021), the angular scale is 0.04 pc arcsec^{-1}.

2.1 Kinematics and history of the nuclear star cluster

On scales of only a few parsecs, the stellar structure closest to and therefore most affected by Sgr A* is the nuclear star cluster (NSC), which has a stellar mass of about $\sim 10^7 M_\odot$ (Launhardt et al. 2002; Feldmeier et al. 2014; Chatzopoulos et al. 2015; Feldmeier-Krause et al. 2017). The first separation of the NSC from the other components of the Galaxy (NSD/bulge/bar/disk) yielded an NSC light profile that appeared well matched by a Sérsic model with an index of ~ 3 and an effective half-light radius of 3.2 pc (Graham & Spitler 2009). A recent estimate reports an index of 2.2 ± 0.7 and $R_e = 5.1 \pm 1.0$ pc (Gallego-Cano et al. 2020). However, perhaps the core-Sérsic model (Graham et al. 2003), fitted separately to the NSC's different stellar populations, may prove more apt at quantifying it and, in turn, yielding insight into its origins and evolution. This could be relevant in the case of binary collisions preferentially removing red giant stars (Davies et al. 1991).

When present, NSCs scale with the mass of their host bulge, possibly in a manner dependent on the host galaxy morphology (Balcells et al. 2003; Graham & Guzmán 2003). Furthermore, a positive correlation between NSC mass and the central BH mass has also been observed (Graham 2016b, 2020). NSCs in late-type galaxies show extended periods of star formation (for a review, see Neumayer et al. 2020), resulting in a younger stellar population

---

[3] We estimate the number of stars in the Galactic Center by considering that all the stars with $J - H > 2$ mag are in the Galactic Center, although a redder cut is likely required at lower galactic latitudes. These numbers are obtained from the combined data of the 2MASS point source catalog and the SIRIUS catalog.

(Walcher et al. 2006). The NSC of the Milky Way also shows extended star formation (Neumayer et al. 2020). Most stars formed more than 5 Gyr ago, followed by a low level of star formation, until the burst of star formation in the last 100 Myr (e.g., Blum et al. 2003; Pfuhl et al. 2011; Nogueras-Lara et al. 2019). Wolf–Rayet and O- and B-type stars (with ages of a few Myr) are found in the central 0.5 pc of NSCs (Paumard et al. 2006; Bartko et al. 2009; Neumayer et al. 2020), which indicates the in situ formation of the NSC of the Milky Way, at least for the youngest population (Aharon & Perets 2015).

On the other hand, using NIR drift-scan spectroscopic observations, Feldmeier et al. (2014) found a kinematic misalignment between the NSC with respect to the Galactic plane and a rotating substructure that suggests past accretion of at least one other star cluster. Dynamical friction may lead to the capture and central deposition of globular clusters (Tremaine et al. 1975). This scenario has some theoretical support, as *N*-body simulations have shown that an NSC like the one in the Milky Way can be produced by the infall of a few globular clusters that are shredded by the SMBH (Antonini et al. 2012; Perets & Mastrobuono-Battisti 2014). Interestingly, high-resolution spectroscopy of the NSC (Rich et al. 2017) finds a wide abundance range spanning [M/H] = −1.25 to supersolar metallicities, [M/H] > 0.3. This is confirmed in larger low-resolution surveys, e.g., using the integral field spectrograph KMOS on VLT by Feldmeier-Krause et al. (2020). They further find that the subsolar population with [M/H] < 0 shows an asymmetric spatial distribution, which might be the signature of a recent globular cluster merger.

Hence, the nature and origin of the NSC of the Milky Way are still in debate, and could link to the in situ star formation at the Galactic Center and/or mergers of globular clusters or ancient mergers with other galaxies. These are distinct dynamical processes, where spectroscopic and numerical studies have made great headway so far. What is missing is the other two dimensions of kinematical information in the proper motion that an astrometric mission, such as JASMINE, can provide. We expect JASMINE to observe about 100 NSC stars with H_w < 14.5 mag. Although this is a small number of stars, the novel $\sim 100\ \mu$as yr^{-1} level of proper motion for the NSC stars, combined with high-precision radial velocities, will likely yield accelerations and orbits. JASMINE astrometry data will also be complementary to astrometry of the fainter infrared sources (e.g., Schödel et al. 2009) and the millimeter–submillimeter sources in the inner region of the NSC, i.e., close to Sgr A*. Recently, Tsuboi et al. (2022) demonstrated that the proper motions of millimeter–submillimeter bright young stars within 0.5 pc of Sgr A* can be obtained with the Atacama Large Millimeter/submillimeter Array (ALMA), measuring the relative astrometry with respect to Sgr A*. Combined with this information, JASMINE will enhance our understanding of the nature and origin of the NSC.

2.2 SMBH formation history

As alluded to at the beginning of this section, remnants of the earliest epochs can be imprinted on the centers of galaxies, and indeed the formation of the SMBHs themselves may leave a mark on their environment. The presence of $10^9\ M_\odot$ SMBHs that powered quasars when the universe was only a few hundred Myr old (e.g., Bañados et al. 2018; Yang et al. 2020; Wang et al. 2021) is a major conundrum for the mechanism of formation of SMBHs (e.g., Rees 1984; Volonteri 2010; Woods et al. 2019). This is especially challenging for the "light" seed scenario, where stellar-mass BHs ($\lesssim 100\ M_\odot$) formed from massive first-generation stars (Pop III stars) in mini-halos. Even if accreting at the maximum stable rate set by the balance of gravity and radiation pressure (the Eddington limit), these light BHs did not have sufficient time to grow into the monster SMBHs powering the earliest quasars. On the other hand, super-Eddington accretion from disk-fed BHs rather than an idealized spherical model may circumvent this concern (Alexander & Natarajan 2014).

Nonetheless, this had made an alternative "heavy" seed scenario more attractive (e.g., Woods et al. 2019). If a metal-free halo is massive enough to host atomic cooling, i.e., $T_{\rm vir} \sim 10^4$ K, and is exposed to strong Lyman–Werner radiation, H_2 cooling is completely suppressed, and the high temperature prevents fragmentation (Omukai 2001). This leads to the formation of a super-massive star, also known as a quasi-star (e.g., Bromm & Loeb 2003; Inayoshi et al. 2014), which directly collapses into a BH with a mass of $\sim 10^4$–$10^6\ M_\odot$ (e.g., Ferrara et al. 2014; Umeda et al. 2016; Woods et al. 2020). These massive BH seeds also form in relatively massive halos with high-density gas, which enables further gas accretion on to the BH. Hence, the heavy seeds can grow rapidly enough to explain the massive SMBHs found at $z \sim 7$.

Although the heavy seed scenario is attractive for explaining SMBHs at high redshift, they are considered to be rare, with a comoving number density of about 10^{-6}–10^{-4} Mpc^{-3} (e.g., Habouzit et al. 2016). This is a smaller number density than that for the Milky Way-sized galaxies. It is an interesting question whether or not the SMBH of the Milky Way formed from a single massive direct collapse to a BH, mainly via accretion. Alternatively, the SMBH of the Milky Way could be formed from more abundant Pop III origin BHs, via accretion and mergers, i.e., the light seed scenario. The light seeds from Pop III stars can be as massive as 1000 $M_\odot$ (Hirano et al. 2014), and using cosmological numerical simulations Taylor and Kobayashi (2014) demonstrated that such light seeds can reproduce the observed BH mass–stellar velocity dispersion relation. In this scenario, BHs are expected to be found ubiquitously in galaxies of all masses, with intermediate-mass BHs (IMBHs, Chilingarian et al. 2018; Greene et al. 2020) of $M_{\rm BH}$ < 10^5–$10^6\ M_\odot$ perhaps common in low-mass galaxies (e.g., Graham et al. 2021b).

Building off the promise of earlier discoveries of AGNs in local dwarf galaxies (e.g., Filippenko & Ho 2003), this predictive framework has fueled an intense search for IMBHs in dwarf galaxies, with some promising results (e.g., Greene & Ho 2004; Farrell et al. 2009; Satyapal et al. 2009; Secrest et al. 2012, 2015; Reines et al. 2013; Graham & Scott 2015; Baldassare et al. 2015, 2020; Graham et al. 2016; Jiang et al. 2018; Davis & Graham 2021), including a dynamically estimated BH mass of NGC 205 having $M_{\rm BH} = 6.8^{+95.6}_{-6.7} \times 10^3\ M_\odot$ (3 σ, Nguyen et al. 2019). The mergers of BHs with $\sim 10^4$–$10^7\ M_\odot$ at the Galactic Center are a prime gravitational wave target of ESA's Laser Interferometer Space Array (LISA, Amaro-Seoane et al. 2017). These multi-messenger astronomy sources will provide strong constraints on the population and merger rates of IMBHs, ultimately revealing the formation mechanism of SMBHs (e.g., Volonteri et al. 2020) and adding detail to the suspected accretion-driven origin of spiral galaxies (Graham 2023b).
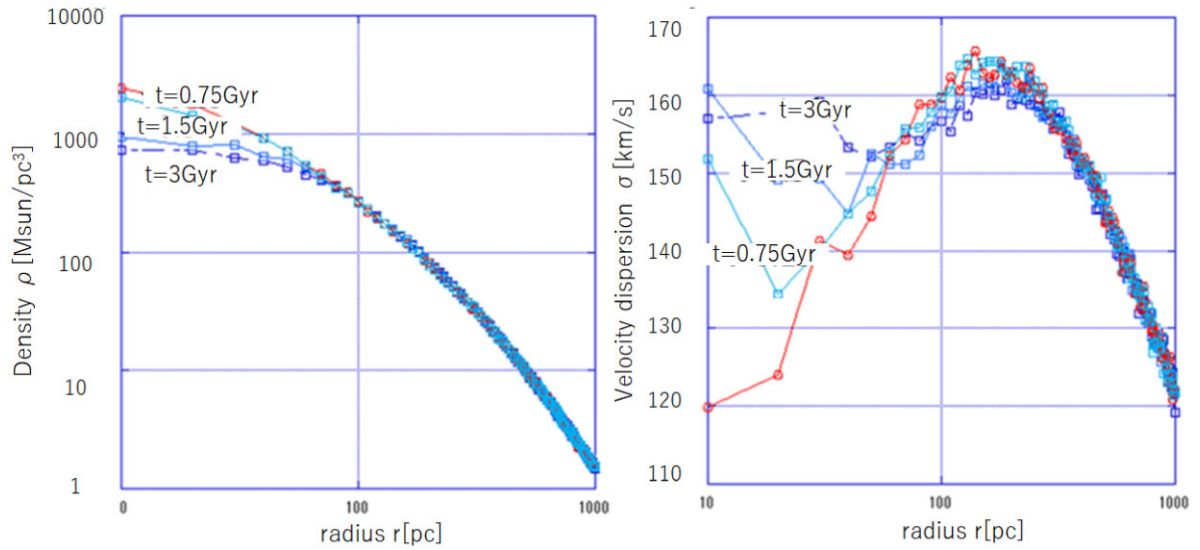
Fig. 3. Density (left) and velocity dispersion distribution (right) profiles of the stellar system. The red line shows the original density and velocity dispersion profile. The blue lines indicate the profiles at different times, as shown by the time labels, since the simulation of the mergers of the five BHs with $8 \times 10^5 \, M_\odot$ started.

JASMINE can provide an independent test of the significance of the IMBH mergers for the formation of the SMBH of the Milky Way, because if the SMBH was built up by the mergers of IMBHs, these coalescences would heat up the older stars within 100 pc of the Galactic Center, with the stellar profile becoming cored (Tanikawa & Umemura 2014). To demonstrate this, we set up an *N*-body simulation of a spherical bulge model, following Tanikawa and Umemura (2014). Although, as discussed in previous and following sections, the Galactic Center has a complex structure—and there are an NSC (subsection 2.1) and NSD (subsection 2.3)—here, for simplicity we consider a spherical isotropic bulge component only. Hence, this merely serves to show the potential capability of the JASMINE data with a simple model. More complex modeling studies are required to address how the different populations of the Galactic Center stars are affected by the mergers of IMBHs, and how gas may spare the ejection of stars.

We have first assumed a spherical stellar component following a Hernquist profile (Hernquist 1990) with a mass of $9 \times 10^9 \, M_\odot$ and a half-mass radius of 1.1 kpc.[4] We use 524288 particles to describe this stellar system. We then add five $8 \times 10^5 \, M_\odot$ BHs, which follow the same distribution function as the stellar system. Because of dynamical friction, these BHs fall into the center of the system, and merge into an SMBH on a timescale of about 1 Gyr (Tanikawa & Umemura 2014). The back reaction of dynamical friction heats up the stellar system in the central 100 pc. Figure 3 shows the density profile (left) and velocity dispersion profile (right) evolution when the BHs merge into a central SMBH. The red lines of these figures show the initial condition of the Hernquist profile with the central density profile slope of r^{-1}. Blue lines show how the density and velocity dispersion profiles change as the

BHs merge into the center of the system, and dynamical friction heats up the stellar system. After 3 Gyr, the density profile becomes significantly shallower with a slope of less than $r^{-0.5}$ within $r = 100$ pc, and the velocity dispersion could differ from the initial velocity dispersion by as much as 30 km s^{-1} at $r \sim 10$ pc. We ran the simulations with different seed BH masses of 4×10^5 and $2 \times 10^5 \, M_\odot$, and found that as long as the total mass is $4 \times 10^6 \, M_\odot$ like the SMBH of the Milky Way, the cored density distribution with a similar size and slope can be caused by the BH mergers, independent of the initial seed mass. A difference, depending on the mass of the seed BHs, is that lighter seed BHs take a longer time to merge into a single central SMBH.

JASMINE is expected to observe about 6000 (68000) stars with $H_w < 12.5 \, (14.5)$ mag and $J - H > 2$ mag in the Galactic Center, and measure their parallax and proper motion with accuracies of 25 (125) μas and 25 (125) μas yr^{-1} [about 1 (5) km s^{-1} at $d = 8.275$ kpc], respectively. The superb parallax accuracy of JASMINE for bright ($H_w < 12.5$ mag) stars will minimize the contamination of the foreground Galactic disk stars. Because the intrinsic NIR colors of giants are almost constant irrespective of their intrinsic luminosity, the color selection criterion for the Galactic Center stars obtained from the parallax–color relation of bright stars at different positions in the sky can be applied to select the Galactic Center stars for the fainter stars (e.g., Nogueras-Lara et al. 2021). Then, we can use the larger number of faint stars with similar colors, which enables us to observe the velocity dispersion profile within 100 pc to tell the difference in velocity dispersion by about 10 km s^{-1} as shown in figure 3. Hence, JASMINE can detect relics of possible BH mergers, if the SMBH of the Milky Way was built up via mergers of IMBHs. If such a heated velocity dispersion profile is not observed, it could be a sign that the SMBH started from a relatively massive BH and grew mainly via accretion, although there could be some alternative scenarios, such as an adiabatic contraction of the bulge stars due to the formation of an NSC and/or NSD.

---

[4] Our assumed bulge mass is slightly larger than the current upper limit of the bulge mass in the Milky Way from kinematics of the stars in the Galactic Center region, e.g., about 10% of the disk mass, i.e., $\sim 5 \times 10^9 \, M_\odot$, suggested by Shen et al. (2010). However, for this simple numerical experiment, we consider a higher mass for increased stability, and as it would provide more conservative results for the dynamical response.

2.3 The nuclear stellar disk: Structure

Extending out to ~200 pc, the Galactic Center hosts an NSD coincident with and of the same scale as the Central Molecular Zone (CMZ, Launhardt et al. 2002). The NSD has an exponential profile (Nishiyama et al. 2013), in accord with other galaxies (Balcells et al. 2007; Ledo et al. 2010; Morelli et al. 2010). The radial extent of the disk is around 230 pc (Bland-Hawthorn & Gerhard 2016), and the vertical scale height is measured to be around 45 pc (Nishiyama et al. 2013; Bland-Hawthorn & Gerhard 2016). The total mass of the nuclear stellar disk is estimated to be around $1.4 \times 10^9\,M_\odot$ (Bland-Hawthorn & Gerhard 2016). The presence of classical Cepheids (Matsunaga et al. 2011, 2015) reveals a thin disk of young stars continuously formed over the past ~100 Myr (Dékány et al. 2015). While line-of-sight velocity studies have been done to understand the kinematics of the NSD (e.g., Schönrich et al. 2015), a full 6D phase-space characterization awaits a high-precision astrometric mission for the Galactic Center stars, which JASMINE will provide, as demonstrated with the current existing dataset in Sormani et al. (2022).

2.3.1 Non-axisymmetry

An interesting question is whether there is a connection between the NSD and the nuclear bar as seen in simulations (e.g., Athanassoula & Misiriotis 2002; Athanassoula 2005; Cole et al. 2014) and inferred in NIR photometric campaigns (Alard 2001; Nishiyama et al. 2005; Rodriguez-Fernandez & Combes 2008; Gonzalez et al. 2011). Nuclear bars are frequently found in earlier galaxy types (Shlosman et al. 1989; Friedli & Martinet 1993; Laine et al. 2002; Erwin 2004), and appear to be a distinct kinematical structure from the main outer bar. Using the VVV survey data, Gonzalez et al. (2011) suggested that the Milky Way has a nuclear bar with a size of about 500 pc that is misaligned with the long bar. Such a nuclear bar, if it exists, can drive the inflow of the gas from the size of the CMZ, from about ~200 to 10 pc, without destroying the NSD or CMZ's disk (or ring) structure (Namekata et al. 2009). However, Gerhard and Martinez-Valpuesta (2012) suggested that the nuclear bar observed in the star counts can be explained by the projection effect of the inner boxy bar (see also Fujii et al. 2019), thus casting doubt on the nuclear bar's existence.

However, the NSD may still have a non-axisymmetric structure, and the strength of the non-axisymmetry could determine the efficiency of the gas inflow. The precise motion of the stars in the NSD provided by JASMINE can enable the assessment of the non-axisymmetry of the NSD, because the kinematics of the NSD stars should be affected by non-axisymmetry, and will provide a stronger constraint than the star count observations.

2.3.2 Young star clusters

There are two young star clusters, the Arches (Nagata et al. 1995) and the Quintuplet (Kobayashi et al. 1983; Nagata et al. 1990; Okuda et al. 1990), within about 30 pc of the Galactic Center. The stellar mass of the Arches is estimated to have an upper limit of $7 \times 10^4\,M_\odot$ (Figer et al. 2002) and the age is about 3.5 Myr (Schneider et al. 2014). The line-of-sight velocity and the proper motion of the Arches cluster are estimated to be $v_{\mathrm{LOS}} = 95 \pm 8\,\mathrm{km\,s^{-1}}$ (Figer et al. 2002) and $v_{\mathrm{pm}} = 172 \pm 15\,\mathrm{km\,s^{-1}}$ (Clarkson et al. 2012), respectively. The stellar mass and age of the Quintuplet are $10^4\,M_\odot$ (Figer et al. 1999) and

4.8 Myr (Nogueras-Lara et al. 2019), respectively. The line-of-sight velocity and proper motion of the Quintuplet cluster are estimated to be $v_{\mathrm{LOS}} = 102 \pm 2\,\mathrm{km\,s^{-1}}$ (Stolte et al. 2014) and $v_{\mathrm{pm}} = 132 \pm 15\,\mathrm{km\,s^{-1}}$ (Stolte et al. 2014).

Based on high-resolution numerical simulations of a barred Milky Way-like galaxy that resolve the star formation in the CMZ, Sormani et al. (2020) argued that the current position and estimated velocity for the Arches and Quintuplet clusters indicate that both clusters formed at the location where the gas inflow from the bar collides with the CMZ. This is consistent with what is also discussed in Stolte et al. (2014), who suggested that the young star clusters formed at the transition place between the x_1-orbits (the gas in the leading side of the bar) and x_2-orbits (CMZ).

Recently, Hosek et al. (2022) measured the absolute proper motion of these clusters using multi-epoch Hubble Space Telescope data and the Gaia EDR3 reference frame, and obtained $(\mu_l \cos b, \mu_b) = (-2.03 \pm 0.025, -0.30 \pm 0.029)\,\mathrm{mas\,yr^{-1}}$ for the Arches and $(-2.45 \pm 0.026, -0.37 \pm 0.029)\,\mathrm{mas\,yr^{-1}}$ for the Quintuplet, where $(\mu_l \cos b, \mu_b)$ are the proper motion in the galactic longitude and latitude directions. These results indicate that these clusters are moving parallel to the Galactic mid-plane.

JASMINE is expected to observe about 10 stars in the Arches and about 20 stars in the Quintuplet with $0.125\,\mathrm{mas\,yr^{-1}}$ proper motion accuracy. The accuracy of the proper motion measurements of these clusters is comparable to previous studies, but JASMINE will have a longer time baseline and an improved absolute reference frame. The combination of the JASMINE data and that from the existing literature will further improve the proper motion measurements. The enhanced proper motions will test the above-mentioned scenario and pinpoint the formation location of these clusters.

JASMINE is also capable of detecting the presence of new young star clusters (see also sub-subsection 5.3.2). Revealing the formation location of hidden young clusters in addition to the Arches and Quintuplet clusters will help us understand the star formation mechanism in the CMZ and their relation to the NSD, by comparison with observations of molecular gas in the Galactic Center region (e.g., Henshaw et al. 2016; Sormani et al. 2020; see also the next section). The recent ability to make precise measurements of the proper motion of star-forming regions by very long baseline interferometry (VLBI) observations, such as the VLBI Exploration of Radio Astrometry (VERA), would provide further information on star formation in the Galactic Center (e.g., Sakai et al. 2023). JASMINE data will be complementary to the VLBI astrometry data to further study the formation and evolution mechanism of the NSD.

2.4 Nuclear stellar disk: The formation epoch of the galactic bar

The central few kpc region of the Milky Way shows a prominent bar structure (e.g., Binney et al. 1997; Bland-Hawthorn & Gerhard 2016). The shape of the inner region of the bar/bulge has been found to display a so-called boxy/peanut morphology (McWilliam & Zoccali 2010; Wegg & Gerhard 2013; Ciambur et al. 2017). The inner stellar kinematics shows a cylindrical rotation (Howard et al. 2008; Bekki & Tsujimoto 2011; Kunder et al. 2012; Ness et al. 2016a), which indicates that the inner bulge is dominated by the bar (Shen et al. 2010; Bekki & Tsujimoto 2011). Shen et al. (2010) found

Table 1. Selection of estimations of the age of the Galactic bar based on various observations.

Age [Gyr]	Method/tracer	Literature
$\sim$3–4	N-body sim., pattern speed of the bar	Tepper-Garcia et al. (2021)
$\sim$3–6	Spatial distribution/infrared carbon stars in the outer bar	Cole and Weinberg (2002)
$\sim$6–8	Spatial distribution/red giants in the inner ring	Wylie, Clarke, and Gerhard (2022)
$\sim$8–9	Spatial distribution/O-rich Miras in the BP-shaped bulge	Grady, Belokurov, and Evans (2020)
$\gtrsim$8	Spatial distribution/red clumps in the NSD	Nogueras-Lara et al. (2019)
$\sim$10	Kinematics and spatial/red giants in the outer bar	Bovy et al. (2019)

that a classical bulge with a merger origin makes up less than 8% of the Galaxy's disk mass. The Galactic bulge is therefore primarily a disk-like structure built up with a more secular formation history (Combes et al. 1990; Kormendy & Kennicutt 2004; Athanassoula 2016).

The central bar components affect the radial and rotational velocity distribution of the Galactic disk stars. The presence of groups of stars moving with particular radial and rotational velocities in the solar neighborhood is considered to be due to the bar (Dehnen 2000). The Hercules stream, which is a group of stars rotating more slowly than the average local azimuthal velocity and moving outward in the disk, has been suggested to be caused by the outer Lindblad resonance of the bar being just inside the Sun's orbital radius, allowing us to derive the pattern speed of the bar (Dehnen 1999, 2000; Ramos et al. 2018; Fragkoudi et al. 2019). However, recent studies demonstrate that such moving groups can also be caused by transient spiral arms (De Simone et al. 2004; Quillen et al. 2011; Hunt et al. 2018; Fujii et al. 2019; Khoperskov & Gerhard 2022), as well as the other resonances of the bar, including the co-rotation resonance (e.g., Pérez-Villegas et al. 2017; Monari et al. 2019a; Chiba et al. 2021; Chiba & Schönrich 2021) and the 4:1 resonance (Hunt & Bovy 2018).

On the other hand, NIR photometric surveys, such as VVV, and spectroscopic surveys, such as the Bulge Radial Velocity Assay (BRAVA, Kunder et al. 2012), the Abundances and Radial velocity Galactic Origins Survey (ARGOS, Freeman et al. 2013; Ness et al. 2013), the Pristine Inner Galaxy Survey (PIGS, Arentsen et al. 2020), and APOGEE, have revealed the detailed stellar structure and line-of-sight velocities of the bar. These observations were directly compared with theoretical models (e.g., Shen et al. 2010; Portail et al. 2015), suggesting a slower pattern speed for the bar than that inferred by assuming that the outer Lindblad resonance lay just inside the solar radius. Recently, both the gas dynamics (Sormani et al. 2015; Li et al. 2022) and stellar dynamics from the Optical Gravitational Lensing Experiment (OGLE, Rattenbury et al. 2007), BRAVA, ARGOS, APOGEE, VVV, and/or Gaia DR2 data (Portail et al. 2017; Sanders et al. 2019; Bovy et al. 2019; Clarke & Gerhard 2022) have converged to a value for the bar pattern speed of around 35–40 km s^{-1} kpc^{-1}.

Bovy et al. (2019) further analyzed the age and stellar abundances of the stars within the bar region, and found it populated mainly by stars with older ages and higher levels of [α/Fe], akin to the properties of old thick disk stars. Bovy et al. further suggested that the Galactic bar formed when the old thick disk formed at an early epoch of the Milky Way's evolution. If the bar did form as early as 10 Gyr ago, it may have affected the chemical distribution of stars in the Galactic disk. For example, the Lindblad resonances due to the bar act as a barrier for stellar migration, and the stars formed inside and outside the outer Lindblad resonance do not mix (Halle et al.

2015; Haywood et al. 2018a). Hence, identifying the epoch of bar formation is an imperative task in understanding the evolution of the Galactic disk. Table 1 summarizes examples of observed estimations of Galactic bar age in the literature. It should be noted that the age of the stars in the Galactic bar does not tell us the formation epoch of the bar, because stars born both before and after the bar can be captured by it (Wozniak 2007; Baba et al. 2022). Hence, the creation epoch of the bar remains a challenging question even in the post-Gaia era.

It is known that bar formation induces gas inflow to the central sub-kpc region of the host galaxy, which leads to the formation of a compact and kinematically cold rotating nuclear gas disk (e.g., Athanassoula 1992; Sormani et al. 2018). Subsequently, the stars formed from the nuclear gas disk build up the NSD (e.g., Friedli & Benz 1993; Athanassoula 2005; Wozniak & Michel-Dansac 2009; Martel et al. 2013; Cole et al. 2014; Ness et al. 2014; Debattista et al. 2015; Seo et al. 2019). Using an N-body/hydrodynamics simulation of a Milky Way-sized disk galaxy, Baba and Kawata (2020) demonstrated that bar formation triggers an intense burst of star formation in the central region, which creates the NSD (figure 4). Consequently, the oldest age limit of the NSD stars displays a relatively sharp cut-off, and it tells us the age of the bar. In this way, the age distribution of the NSD in the Milky Way can tell us the formation epoch of the Galactic bar (see also Fragkoudi et al. 2020).

Baba and Kawata (2020) showed that the NSD is kinematically colder than the other stellar components, which is consistent with the recent observation mentioned above (Schultheis et al. 2021). Hence, the NSD stars can be identified kinematically. Baba and Kawata (2020) also suggested that stellar proper motions in addition to line-of-sight velocities are crucial to reducing contamination from other, kinematically hotter, stars, such as those from the bulge, bar, and Galactic disk. The superb astrometric accuracy of JASMINE will enable us to identify the NSD stars and reduce the contamination from the other stellar components.

To obtain the age of the NSD stars, we will use Mira variables, because they are known to follow an age–period relation (Feast & Whitelock 1997; Grady et al. 2019; Zhang & Sanders 2023). Mira variables are intrinsically bright, and there are expected to be enough Miras in the JASMINE GCS to enable a robust age distribution study of the NSD. From the number of observed Miras in a smaller region of the Galactic Center in Matsunaga et al. (2009), it is expected that about 2000 Miras whose color is red enough to be at the distance of the NSD and with a luminosity brighter than $H_{\rm w} = 14.5$ mag will be observed within the GCS region of JASMINE. The proper motion measurements by JASMINE as well as the line-of-sight velocity from ground-based spectroscopic follow-up data (see section 6 for potential
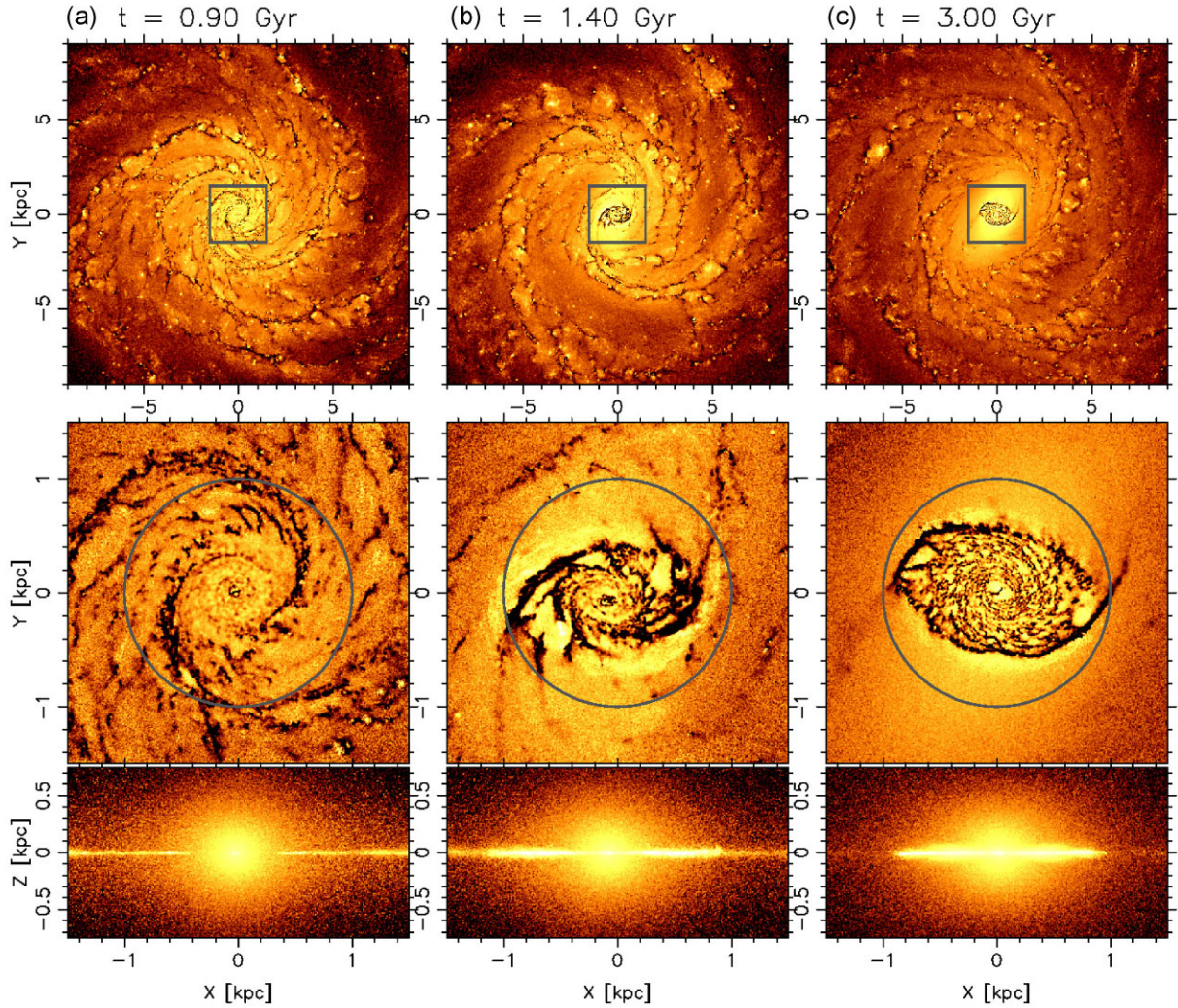
Fig. 4. Morphological evolution of a simulated Milky Way-sized galaxy (Baba & Kawata 2020) in face-on views of the whole galaxy scale (top row), the central region (middle row), and in an edge-on view of the central region (bottom) at times (a) prior to, (b) during, and (c) after bar formation. Orange colors indicate the surface density of stars on a logarithmic scale, and the dark filamentary structures in the face-on views (top and middle panels) indicate the cold dense gas. After the bar has formed, the major axis of the bar is orientated such that its major axis lies 25° from the *y*-axis.

instruments to be used) will enable us to pick out Miras in the NSD.

Before the launch of JASMINE, we need to identify Miras in the JASMINE GCS field (figure 2) with long-term time-series photometric surveys. Recently, Sanders et al. (2022) identified more Miras from the VVV survey. We will also use the upcoming data from the Prime focus Infrared Microlensing Experiment (PRIME, see sub-subsection 6.1.1), which is a joint Japan–USA–South Africa 1.8 m NIR telescope (with 1.3 deg² FoV) built in South Africa. The PRIME data will allow us to identify brighter Miras that are saturated in the VVV data and be valuable to verify the VVV Miras.

Although the age–period relation of the Miras is still not well calibrated, we expect that it will be improved with Gaia data (e.g., Zhang & Sanders 2023). Even without such a relation, the period of such Miras will be measured precisely, while identifying the shortest period of Miras in the NSD and comparing it with the period of Miras in the other Galactic components will tell us the relative formation epoch of the Galactic bar (see figure 5), e.g., with respect to those for the thick and thin disks. This was demonstrated in Grady, Belokurov,

and Evans (2020), who focused on the age of stars in the bar, but who could not reach the NSD because they studied Miras detected by Gaia (see also Catchpole et al. 2016).

2.4.1 Slowdown of the bar pattern speed

Producing a sample of NSD stars with age information will also help to further uncover the slowdown history of the pattern speed of the Galactic bar. Recently, Chiba, Friske, and Schönrich (2021) and Chiba and Schönrich (2021) suggested that the kinematics of local stars observed in Gaia DR2 can be naturally explained if the pattern speed of the Galactic bar is slowing down. The slowdown of the bar pattern speed is often seen in *N*-body simulation of barred galaxies and is considered to be due to the transfer of the angular momentum of the bar to the dark halo (e.g., Weinberg 1985). The size of the NSD is likely affected by the location of the inner Lindblad resonance of the bar or the existence of x_2-orbits (e.g., Regan & Teuben 2003; Li et al. 2015), which is likely affected by the pattern speed of the bar. Hence, it is expected that the age distribution of the NSD disk as a function of radius and/or angular momentum could be sensitive to the slowdown history of the
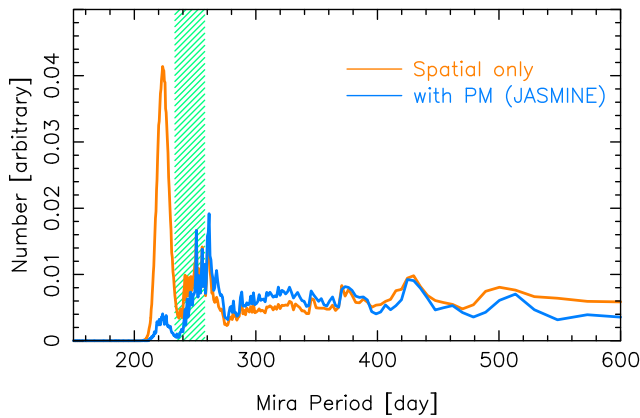
Fig. 5. Expected period distribution of the Mira variables in the NSD of the simulation shown in figure 4. The periods of Miras are derived from the age of star particles in the simulation snapshot at $t = 5$ Gyr, using the empirical age–period relation in Grady, Belokurov, and Evans (2019). The orange line indicates the period distribution of Miras, when the star particles are chosen by spatial information only, i.e., by the location corresponding to the galactic longitude and latitude range of the NSD. The blue line shows the period distribution when the stars are selected by the galactic longitude and latitude region of the NSD and the line-of-sight velocity and proper motion region corresponding to the NSD kinematics. In this simulation snapshot, the bar age is 3.5 Gyr (green shaded region). Here, we have assumed that there is a kinematically hot component, i.e., a classical bulge, which is 1 Gyr older than the formation age of the bar. The orange line shows significant contamination from such a component, while the blue line with the additional kinematical selection of the NSD shows a sudden decrease of the population with shorter periods than about 250 d, which corresponds to the formation age of the bar.

Galactic bar. Interestingly, a radial dependence of the age of the NSD stars was recently indicated by Nogueras-Lara et al. (2023), motivating further studies. JASMINE will be able to provide the age and kinematics of stars in the NSD, which will open up this new window to unravel the history of the Galactic bar pattern speed. How the NSD stellar age and kinematics are affected by the change in bar pattern speed is not well understood. Also, the bar pattern speed may not monotonically spin down, but may spin up, for example, due to gas infall. This could cause a more complicated mix of the age–kinematics relation of NSD stars. More theoretical studies on this topic are also encouraged.

2.4.2 Impacts on radial migration and the Sun's birth radius

Identifying the bar formation epoch and the evolution of the pattern speed is crucial to answering how radial migration shaped the current chemodynamical structure of the Galactic disk. Bar formation induces significant radial migration in stars of the Galactic disk (e.g., Di Matteo et al. 2013; Khoperskov et al. 2020), and the coupling between bar resonances and spiral arm resonances further induces strong radial migration of disk stars (Minchev & Famaey 2010). The slowing down of the bar pattern speed means that the resonances of the bar sweep a large radial range of the Galactic disk, and affect the kinematics of the disk stars at these radii and enhance radial migration (Halle et al. 2015, 2018; Khoperskov et al. 2020; Chiba et al. 2021).

The Sun is considered to have been formed in the inner disk ($R \sim 5$–7 kpc), and to have radially migrated outward to reach its current radius (e.g., Wielen et al. 1996; Sellwood & Binney 2002; Minchev et al. 2018; Feltzing et al. 2020; Tsujimoto & Baba 2020). It is a fascinating question as to whether the

Galactic bar formed before or after the formation of the Sun. If the Galactic bar is younger than the age of the Sun, the orbital history of the Sun is likely impacted by the Galactic bar formation, in addition to radial migration due to resonances, making this a key question in understanding the Sun's dynamical history.

Recently, the accurately measured chemical abundance pattern of a large number of disk stars by APOGEE combined with the kinematics provided by Gaia has enabled modeling of the history of the inside-out disk formation of the Galactic disk and the impact of the radial migration of stars (Hayden et al. 2015; Frankel et al. 2018, 2020; Imig et al. 2023). However, radial migration due to bar formation and evolution has not yet been taken into account, because of the complexity of such a model with additional parameters needed to fit the data and thus requiring additional priors. One such key prior is the formation epoch of the bar. As discussed in this section, JASMINE will provide this important piece of information from the age distribution of the NSD.

2.4.3 Comparison with the cosmic bar fraction and the past merger history of the Milky Way

It would be also interesting to compare the bar formation epoch of the Milky Way with the cosmic bar fraction (e.g., Sheth et al. 2008), to study how common the formation epoch of the Milky Way is. Identifying the bar formation epoch in the Milky Way allows us to study the physical process of the Galactic bar formation by comparing it with the expected formation epochs of the bar with different mechanisms from cosmological simulations (e.g., Cavanagh et al. 2022; Izquierdo-Villalba et al. 2022). Another intriguing question is if the formation epoch of the bar of the Milky Way is similar to the time of the merger events of the Gaia–Sausage–Enceladus and the Sagittarius dwarf, whose impact could have induced the bar formation of the Milky Way.

2.5 Nuclear stellar disk: A link to high-redshift progenitors

The size of the Galactic nuclear disk is similar to the size of star-forming galaxies at redshift, $z > 6$ (Shibuya et al. 2015; Kikuchihara et al. 2020), as also recently seen by JWST (Ono et al. 2023). The compact disks observed at high redshift display a surface brightness profile following an exponential law, like a rotating disk (Shibuya et al. 2019). The theoretical study of Bekki (2000) suggested that the gas accretion to a massive BH can create an NSD-like compact disk at high redshift. It would be a fascinating question whether the Milky Way started its formation from a compact disk similar to those observed at high redshift, and, if so, whether part or the majority of the NSD could be a relic of such a compact disk epoch.

The age and metallicity distribution of the NSD disk stars identified from the proper motions measured by JASMINE will answer this question regarding the early structure of the Milky Way. If JASMINE finds an old and metal-poor population in the NSD, in addition to the populations formed after bar formation, they could be a relic of the high-redshift disk. A comparison of the kinematics and metallicity properties between the Milky Way's old disk and the high-redshift disks in Milky Way progenitors will be a new window to connect Galactic archaeology to the observations of high-redshift galaxies (see also Clarkson et al. 2008; Renzini et al. 2018), which will be further advanced by the advent of JWST and

future 30 m class ground-based telescopes, such as E-ELT, GMT, and TMT.

2.6 Inner disk: Spiral arms and galactoseismology

The foreground stars of the JASMINE GCS field will give access to Galactic disk kinematics from the solar radius to the Galactic Center. The Gaia data revealed the striking ridge-like features in the stellar rotation velocity distribution as a function of radius, i.e., the R_{GC}–V_ϕ diagram (Antoja et al. 2018; Kawata et al. 2018; Ramos et al. 2018). These features also correlate with the radial velocity of the stars (Fragkoudi et al. 2019), and are considered to be due to bar resonances and effects of the spiral arms (e.g., Hunt et al. 2018, 2019; Friske & Schönrich 2019; Asano et al. 2020). Because of the heavy dust extinction in the inner disk, the Gaia data can reach only up to about 3 kpc, i.e., $R_{GC} \gtrsim 5$ kpc, in the mid-plane toward the Galactic Center. The NIR astrometry of JASMINE can extend this analysis all the way to the Galactic Center.

The nature of spiral arms, especially whether they are classical density wave-like features (Lin & Shu 1964) or transient features (e.g., Sellwood 2011), is currently hotly debated (see Dobbs & Baba 2014; Sellwood & Masters 2022 for reviews). Spiral arms could be related to the bar (e.g., Athanassoula 2012) and induced by satellite galaxy interactions (e.g., Purcell et al. 2011; Pettitt et al. 2016). Also, the effects of spiral arms on radial migration depend on the nature of the spiral arms. Radial migration is much more significant if the spiral arms are transient features (e.g., Sellwood & Binney 2002; Grand et al. 2012). JASMINE will provide detailed kinematics of the stars towards the Galactic Center, which covers the Sagittarius arm and the Scutum–Centaurus arm. The locations of the spiral arms of the Galaxy are still not measured confidently from the stellar kinematics, although they can be traced with the gas, star-forming regions, and young stars (e.g., Nakanishi & Sofue 2006; Reid et al. 2019; Skowron et al. 2019; Colombo et al. 2022). It is also debated whether the Sagittarius arm is the major arm, i.e., a stellar arm, or purely a gas arm (e.g., Benjamin et al. 2005; Pettitt et al. 2014), although the recent Gaia EDR3 data indicate an excess of young stars in the Sagittarius arm (Poggio et al. 2021). A crucial piece of information regarding the nature of spiral arms and the strength of stellar spiral arms is the stellar kinematics both inside and outside of the arm (Baba et al. 2013, 2018; Kawata et al. 2014). In addition to the GCS, we plan to run a Galactic mid-plane survey (see subsection 5.1 for more details). A combination of these data can provide the kinematics of both sides of the Sagittarius arm and the Scutum–Centaurus arm at different radii. Comparison between these data and *N*-body modeling of disk galaxies will be necessary to ultimately answer the long-standing question in Galactic astronomy of the nature of spiral arms.

The Gaia data also revealed a vertical corrugation in the vertical velocity, v_z, of the disk stars as a function of Galactocentric radius (Schönrich & Dehnen 2018; Gaia Collaboration 2018b; Kawata et al. 2018), which is related to the phase spiral most clearly seen in the z–v_z diagram when colored by the radial velocity, v_{rad} (Antoja et al. 2018; Bland-Hawthorn et al. 2019b; Hunt et al. 2022). Hence, they are likely closely linked with in-plane kinematical features, such as moving groups, the R_{GC}–V_ϕ ridge-like features, and spiral arm features (e.g., Laporte et al. 2019; Khanna et al. 2019; Bland-Hawthorn & Tepper-García 2021; Hunt et al.

2021; Antoja et al. 2022). These vertical kinematical features are considered to be due to the recent ($<$Gyr) perturbation from the Sagittarius dwarf galaxy (Bland-Hawthorn et al. 2019b; Laporte et al. 2019) and/or the wake of the dark matter halo induced by an earlier phase of the infall of the Sagittarius dwarf a few Gyr ago (Grand et al. 2023). However, it is also possible for them to have been induced by bar buckling, which may have happened recently and created the X-shaped/boxy inner Milky Way bar (Khoperskov et al. 2019). Tracing the vertical corrugation seen around the solar radius towards the Galactic Center will be key to answering whether this dynamical phenomenon is ubiquitous in the inner disk. A comparison of the observed corrugation features as a function of radius with different models of the Sagittarius dwarf perturbation and the bar buckling model will allow us to reveal the origin of the corrugation. Both the impact of the dwarf perturbation and the bar buckling can also significantly affect radial migration. The Galactoseismic information on both in-plane and vertical kinematics as measured in the inner disk by JASMINE will provide crucial information regarding the recent dynamical evolution of the Galactic disk.

The foreground disk stars of the JASMINE GCS field up to $d \sim 6$ kpc from the Sun are dominated by red giants. The time-series photometry of JASMINE with about 46 instances of $\sim$12.5 s exposures every $\sim$530 min for 3 yr of the nominal lifetime of the telescope will be highly valuable for asteroseismology. It will allow for the measurement of precise stellar masses, which will provide relative ages of stars, crucial information for Galactic archaeology studies (e.g., Chaplin & Miglio 2013; Miglio et al. 2021a).

It is also likely that a few open clusters will be discovered in this field. There is at least one star cluster (UBC335) in the new Gaia DR2 star cluster catalogue (Castro-Ginard et al. 2020) in the JASMINE GCS field. These cluster data would be useful for the calibration of asteroseismic ages, as proposed in an ESA M7 mission candidate, HAYDN (Miglio et al. 2021b). JASMINE can provide a proof of concept study for HAYDN in terms of asteroseismology in dense stellar fields.

The ages of giant stars can also be obtained from follow-up spectroscopic data, mainly from [C/N] (Masseron & Gilmore 2015; Martig et al. 2016), which can be calibrated by their asteroseismic ages. Machine learning techniques are often used to train a model to map the chemical abundance patterns to ages, where having a high-quality training set is crucial (e.g., Ness et al. 2016b; Das & Sanders 2019; Mackereth et al. 2019; Ciucă et al. 2021). Asteroseismology from JASMINE combined with spectroscopic follow-up data will provide the unique calibration information for the inner disk red giants needed for future machine learning applications.

3 Exoplanet survey (EPS)

3.1 Transiting planet survey around late-type stars

As described in the introduction (subsection 1.2) and shown in figure 6, terrestrial planets in the HZ around mid-to-late M dwarfs remain difficult to explore with both TESS and ground-based surveys. Searching for terrestrial planets around ultra-cool dwarfs like TRAPPIST-1 is challenging for TESS owing to its modest 10.5 cm aperture. In ground-based surveys, HZ terrestrial planets around earlier-type stars, like TOI-700, exhibit transits that are too shallow and have too long
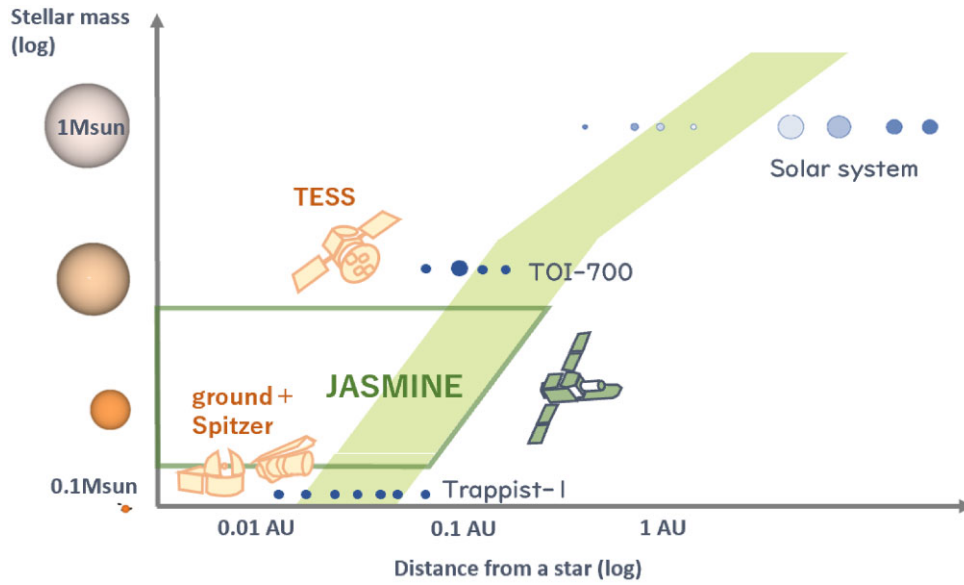
Fig. 6. Survey area for the JASMINE transit survey on the plane of star–planet distance versus stellar mass, contained within the green box. The HZ is shaded light green.
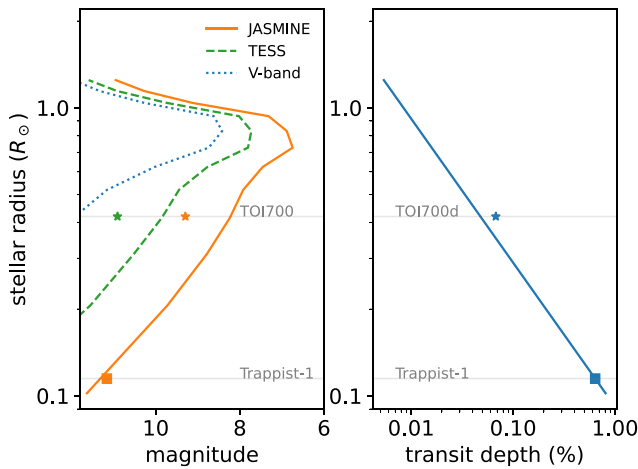

Fig. 7. Left: The lines show the apparent magnitudes of the 250th brightest star in the sky in each radius bin of width of $\Delta R = 0.1 \, R_\odot$, where the stars are from TESS candidate target list version 8 obtained via the Mikulski Archive for Space Telescope database. Solid, dashed, and dotted lines indicate the magnitudes in the JASMINE H_w, TESS, and *V* bands, respectively. The positions of TOI-700 and TRAPPIST-1 are indicated by stars and squares, respectively, and their color indicates the magnitude of JASMINE (orange) and TESS (green) magnitudes. Right: Transit depth due to an Earth-sized exoplanet as a function of stellar radius.

orbital periods. In contrast, JASMINE has a 36 cm aperture and an NIR passband, and can also perform long continuous monitoring from space and suppress intrinsic variability due to stellar activity (see sub-subsection 3.6.3 for details). This makes JASMINE a unique probe of terrestrial planets in the HZ around mid-to-late M dwarfs that have orbital periods of several weeks, or semi-major axes of 0.03–0.3 au. Figure 7 shows this trade-off relation between stellar brightness and transit depth. The left panel shows the apparent magnitudes of the 250th brightest star in a radius bin of width of $0.1 \, R_\odot$, where $R_\odot$ is the solar radius. For M-type stars with radii smaller than $0.5 \, R_\odot$, smaller stars are apparently

fainter both in the visible and NIR bands. In contrast, the transit signals are larger for those smaller stars, as shown in the right panel. The sweet spot for precise NIR photometry with JASMINE therefore lies around 0.2–0.3 $R_\odot$.

Figure 8 assesses this statement more realistically. Here, we estimate the H_w magnitudes of the brightest M dwarfs in the entire sky that host transiting Earth-sized planets in the HZ whose transits are deep enough to be detected with JASMINE. The result is based on a Monte Carlo simulation consisting of the following three steps: (i) Assign Earth-sized planets at the inner edge of the classical HZ to certain fractions (here 100% and 10%) of nearby M dwarfs in the TESS candidate target list (Stassun et al. 2019). (ii) Check which planets show transits, assuming that the orbits are isotropically oriented. (iii) Check whether a single transit signal has a signal-to-noise ratio (S/N) greater than 7, where the signal is computed from the stellar radius, and the noise is evaluated for the timescale of expected transit duration using the noise model in subsection 3.6. The dashed and dotted lines show the magnitudes of the brightest stars estimated from 10000 random realizations in each stellar-mass bin, assuming that HZ Earths occur around 100% and 10% of the sample stars, respectively. These estimates are compared with known transiting planets and planet candidates from ground- and space-based surveys (see legends), including the two Earth-sized planets ($<1.5 \, R_\oplus$) in the HZ, TOI-700 and TRAPPIST-1, shown with filled symbols. The occurrence rate of HZ Earths around mid M dwarfs is yet to be quantified; the Kepler sample suggests an occurrence rate of $\sim$30% around earlier M dwarfs (e.g., Dressing & Charbonneau 2013, 2015; Hsu et al. 2020), and here the values of 100% and 10% are chosen to bracket this estimate. While it is unclear whether the estimate for earlier M dwarfs can be simply extrapolated to mid M dwarfs, the fact that the two known planets lie close to the dotted line (i.e., the brightest planet hosts assuming the 10% occurrence have already been found) appears to be consistent with the occurrence rate of $\gtrsim$10% around later M dwarfs. Our simulation results demonstrate the ability of JASMINE to identify
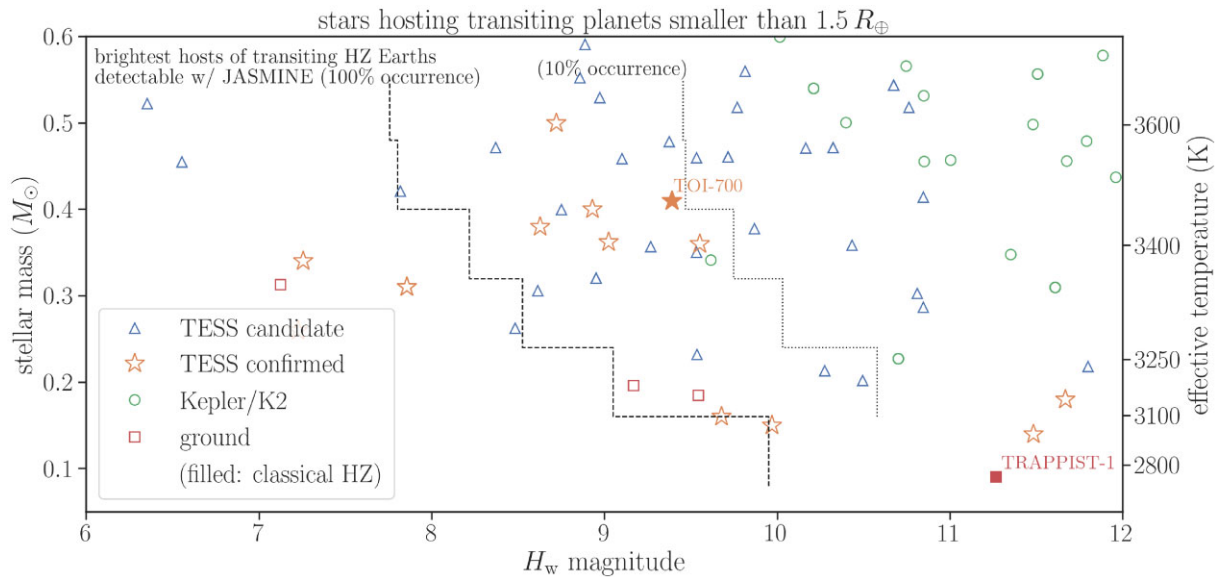
Fig. 8. JASMINE's photometric precision is sufficient to find transiting Earth-sized planets in the HZ of the brightest mid M dwarfs. The black dashed and dotted lines show the estimates of the H_w magnitudes of the brightest stars in the sky for which transit signals due to HZ Earths are large enough to be detected by JASMINE photometry (see text for details); here 100% and 10% of M dwarfs in the TESS candidate target lists harbor such planets, respectively. The open and filled symbols denote the masses and H_w magnitudes of stars with known transiting planets smaller than 1.5 $R_\oplus$. Most of these planets are outside the classical HZ except for TOI-700 and TRAPPIST-1, shown as a filled star and a square, respectively.

Earth-sized transiting planets in the HZ of mid M ($\sim$0.2 $M_\odot$) dwarfs with $H_w \lesssim 10$ mag, if their occurrence rate is $\gtrsim \mathcal{O}(10\%)$ and if those stars are monitored over a sufficiently long time.

The habitability of exoplanets is often evaluated based on the concept of the habitable zone. For tidally locked exo-terrestrial planets, the inner edge of the habitable zone should be considered in relation to atmospheric dynamics, which is primarily affected by the planet's orbital period. Recent studies using 3D general circulation models (GCMs) suggest that a tidally locked terrestrial planet near the inner edge of the habitable zone of a star, with an effective temperature exceeding 3300 K, is likely to exhibit atmospheric circulation characterized by strong convective motions beneath the substellar point and a thermally direct circulation between the day and night hemispheres (e.g., Showman et al. 2013; Haqq-Misra et al. 2018). This strong convection facilitates the formation of thick clouds, which envelop the planet's dayside hemisphere, thereby increasing its albedo (Yang et al. 2013). As a result, this cloud feedback mechanism can render a tidally locked terrestrial planet habitable even if a planet exists closer to the star than the inner boundary of the classical habitable zone, corresponding to the inner edge of 1.3 solar insolation compared with 0.95 solar insolation of the classical one for 3300 K. Conversely, the inner edge of the habitable zone for a star with an effective temperature below $\sim$3000 K gets closer to the classical definition. This is attributed to the dimmer nature of such stars, where clouds on the dayside are advected eastward off the substellar point due to rapid rotation (Kopparapu et al. 2017). Hence, focusing on JASMINE targets around stars with effective temperatures near 3000 K is critical for understanding the boundary conditions affecting the habitability of tidally locked exo-terrestrial planets, as well as for elucidating their climate formation and verifying our theories regarding habitable planets.

3.2 Follow-up characterization from space

Photometry from space is important not only for finding new transiting planets, but also for characterizing them. For example, modeling of transit timing variations (TTVs) (i.e., variations in the orbital periods due to gravitational interactions between multiple planets) measured by Spitzer played a significant role in precisely weighing the planets of the TRAPPIST-1 system (e.g., Grimm et al. 2018; Agol et al. 2021). Such precise masses for Earth-mass planets are still difficult to obtain, even with state-of-the-art infrared spectrographs, but are crucial for understanding the composition of these planets and for interpreting their transmission spectra. Even if TTVs alone are not sufficient for obtaining precise masses, they still constrain mass ratios, and joint analyses with RV data improve mass measurements. Thus, follow-up observations of known multi-transit systems with JASMINE are valuable, even if no new transiting planet is found. These data contribute to the derivation of the best-constrained masses for terrestrial planets transiting late-type stars.

Long-term photometry from space is important even for single-transit planets without any known signature of dynamical interactions. Extending the baseline of transit measurements helps to pinpoint the ephemeris of transiting planets found from relatively short baseline observations. If follow-up spectroscopy is performed much later than the discovery, a small error in the ephemeris calculated from the discovery data could result in a transit prediction that is far from the actual value (stale ephemeris problem). Extending the transit baseline is essential to avoid wasting precious observation time, for example, with JWST. Checking for the presence or absence of TTVs is also important in this context.

The ability to perform high-cadence, high-precision NIR photometry from space makes JASMINE a unique follow-up facility, similar to Spitzer, even for systems with shorter observing baselines. The detailed shapes of the transit light curves revealed from such measurements are important for

ensuring that the system is not an eclipsing binary system (which tends to produce V-shaped dips). The chromaticity of the transit also helps to identify stellar eclipses if the candidates are obtained from optical observations. Better constraints on the transit shapes, in particular the durations of the transit ingress and egress, also improve the measurements of transit impact parameters, and hence the planetary radii (Petigura 2020), as the two parameters are correlated through stellar limb darkening. This is important for learning about their compositions, given that the precision of stellar parameter measurements has now become comparable (or even better, depending on the instrument) to the precision of the radius ratio measurements from the transit light curve. NIR observations are particularly well suited for this task because the limb-darkening and stellar variabilities (i.e., the source of correlated noise) are both weaker than those in the optical regime.

Spitzer was an important facility to perform such space-based follow-up observations until 2020. A similar role is now being fulfilled by the CHaracterising ExOPlanet Satellite (CHEOPS). JASMINE could serve as a successor to these missions in the late 2020s and address various other scientific questions as were covered by Spitzer (cf. Deming & Knutson 2020). See table 2 for comparisons of those space missions.

3.3 Searching for young planets

Other potential targets for the pointing–individual–target (PIT)-type transit survey by JASMINE are stars in star clusters, young moving groups, and younger star-forming regions. Recently, transit surveys from space have unveiled a population of young close-in planets (for example, Mann et al. 2017, 2018; Plavchan et al. 2020). These planets are often reported to have inflated radii for their insolation flux level received from host stars (Mann et al. 2016), in comparison with their older counterparts. Some super-Neptune-sized young planets were discovered as multi-planet systems, and those could be progenitors of "compact-multi" super-Earths (David et al. 2019), most commonly found around main-sequence solar-type stars. Hypotheses can be tested in relation to the formations of the super-Earth "radius gaps" (Fulton et al. 2017) and the desert of the close-in Neptunian planets (Lundkvist et al. 2016). Measurements of eccentricities and inclinations (spin–orbit angles) of young planets would also allow the corroboration or refutation of planet migration theories for close-in large planets (for example, Hirano et al. 2020a, 2020b). Overall, young exoplanet systems provide an ideal setting for testing hypotheses on planet formation and evolution.

Younger systems allow two possible directions for JASMINE observations. One is a blind transit survey for stellar clusters, stars in star-forming regions, etc. Although the FoV of JASMINE is much smaller than that of ordinary tran-
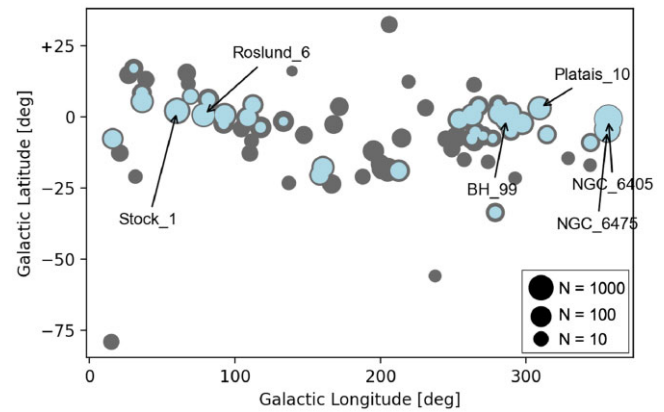

Fig. 9. Distribution of clusters that are closer than 500 pc from the Earth. The original list is cited from Cantat-Gaudin et al. (2018). The sizes of the data points represent the number of detectable cool targets within the FoV of $0°\!.55 \times 0°\!.55$, when transiting planets exist. The blue and gray colors correspond to assumed planetary radii of Earth size and Neptunian size, respectively. Details are described in subsection 3.3.

sit surveys (i.e., often larger than $10° \times 10°$), many stars in the clusters (of the order of 10–100 for, e.g., the Beehive open cluster) are simultaneously observed, even with JASMINE's FoV ($\approx 0°\!.55 \times 0°\!.55$). This simultaneous photometry for multiple stars would significantly enhance the probability of transit detection compared with targeting field stars. For reference, the distribution of the clusters within 500 pc from the Earth, i.e., close enough to detect planet transits, is shown in figure 9. The size of data points represents the number of cool stars that may show a larger transit signal than 4σ when transiting a planetary candidate's orbit. The blue and gray colors correspond to cases when the transiting planetary radii are Earth- and Neptune-sized, respectively. Here, we computed stellar radii using relations between the Gaia $BP - RP$ colors and effective temperatures in Mann et al. (2015). The transit depth was derived as $(R_{\rm p}/R_\star)^2$ and the photometric noise follows figure 10. There are a good number of clusters that contain ~100 effective targets for the blind survey of transiting planets along the galactic longitude. The other direction is the follow-up photometry of planet hosts or planet-candidate-hosting young stars for an additional planet search, as in the case of the M dwarf campaigns described in the previous sections. These follow-up observations target young stars hosting transiting close-in planets, similar to K2-25b and AU Mic b. It should be stressed that, for these targets, space photometry by Spitzer has played a significant role in confirming the planetary nature and refining transit ephemerides (Thao et al. 2020; Plavchan et al. 2020). Reduced flux modulations resulting

Table 2. Capability of performing photometry from space.

Mission	Telescope	Passband	Pixel size	FOV for late-type stars	Relative modulation amplitude by stellar activity[*]	Status
JASMINE	36 cm	1.0–1.6 μm	$0''\!.4$	$0°\!.55 \times 0°\!.55$	~0.4	2028 (planned)
TESS	10.5 cm	0.6–1.1 μm	$21''$	$24° \times 24° \times 4$	~0.8	2018–
CHEOPS	32 cm	0.4–1.1 μm	$1''$	$0°\!.32 \times 0°\!.32$	~0.9	2019–
Kepler	95 cm	0.4–0.9 μm	$4''$	$12° \times 12°$	1	Retired
Spitzer	85 cm	3.6–8 μm	$1''$–$8''$	$5' \times 5'$		Retired

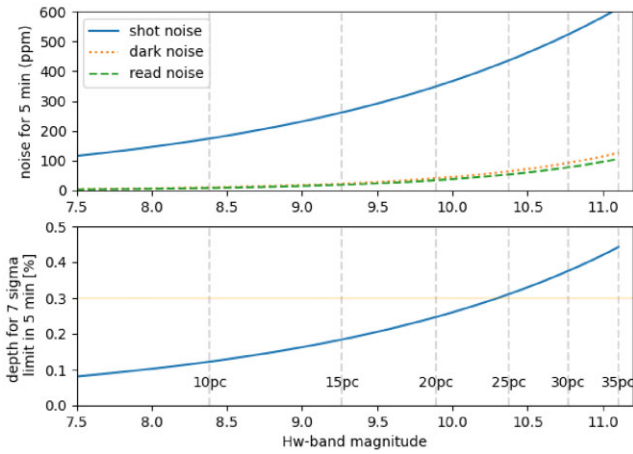[*]See sub-subsection 3.6.3 for further details.

Fig. 10. Statistical noise as a function of H_w magnitude. Top panel: 1 σ level of shot, dark, and readout noises. Bottom: Transit depth corresponding to 7σ detection during a 5 min exposure (in terms of being able to measure the transit shape, the S/N at 5 min is shown). A telescope diameter of 36 cm was assumed (secondary telescope is 12.6 cm). The dark and readout noise are assumed to be 25 e$^-$ s^{-1} and 15 e$^-$ read^{-1}. The limiting distances are computed for a 0.2 $R_\odot$ star with a 3000 K blackbody spectrum. The horizontal yellow line indicates the typical depth of Earth-sized planets around a mid M-type star.

Fig. 11. Passbands of JASMINE (green solid), TESS (blue dotted), and CHEOPS (orange dashed), each normalized by its maximum throughput. The red solid line indicates the normalized photon flux of an M-type star (3000 K, log $g = 5$) by PHOENIX.

from stellar activity in the NIR region (Miyakawa et al. 2021) make JASMINE optimal for these types of transit surveys from space (see sub-subsection 3.6.3). The HZ around young stars (even M stars) tends to be further out in orbit ($P > 50$ d) because of their inflated radii, but the HZ shrinks in the orbital distance as the system ages and the central star becomes smaller. Finding "future-habitable" planets would be an intriguing topic.

3.4 Stellar spin-down relations from young cluster observations

Photometric observations of stars in young clusters described in subsection 3.3 would usher in new knowledge on stellar rotation evolution, especially in young mid-to-late M dwarfs. It has been known that stars spin down over time via magnetic braking (angular momentum loss) since Skumanich (1972). This has led to the development of the gyrochronology relation, which uses stellar rotation periods ($P_{\rm rot}$) as an indicator of stellar ages (e.g., Barnes 2003). This gyrochronology relation is important for considering the effects of stellar magnetic activities (e.g., X-ray/EUV emissions) on the planetary atmosphere over various ages (e.g., Tu et al. 2015; Johnstone et al. 2021).

Recent K2 mission data have provided us with the measurements of $P_{\rm rot}$ in benchmark open clusters over various ages from pre-main-sequence age ($\sim$3 Myr) to intermediate age ($\sim$2.7 Gyr) (Curtis et al. 2020; Rebull et al. 2020; Johnstone et al. 2021). They showed that the formula describing the process of stellar spin-down cannot be as simple as first assumed. Curtis et al. (2020) showed that low-mass stars show temporal stalling of spin-down in medium ages. Rebull et al. (2020) reported on the rotation of stars in younger clusters (from 1 to 790 Myr), and the properties of rotation evolution differ greatly depending on spectral types. This would also be closely related to star–disk interactions in the pre-main-sequence phase of stellar evolution (e.g., Bouvier et al. 2014). These recent studies showed the possibility that the rotation
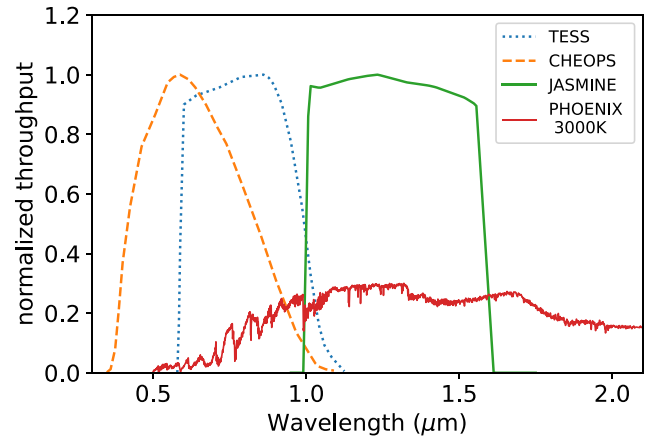
evolution of M dwarfs could be somewhat different (e.g., large scatter of M dwarfs at $\sim$790 Myr in figure 9 of Rebull et al. 2020) from that of G dwarfs, and this difference is yet to be completely understood. Moreover, in the previous studies using K2 and TESS data, there are very few measurements of mid-to-late M dwarfs. For example, in the K2 optical observations, most mid-to-late M dwarfs were not selected as targets. Then NIR photometric observations using JASMINE would help to fill in this "blank region" by measuring the rotation period of more mid-to-late M dwarfs in young stellar clusters, as byproducts of young cluster observations described in subsection 3.3.

As discussed in the above sections, mid-to-late M dwarfs are bright in NIR wavelengths (figure 11), and the precision of JASMINE photometric observations for mid-to-late M dwarfs can be better than K2 and TESS. In addition, the pixel size of JASMINE, which is more than an order of magnitude better than those of Kepler and TESS (table 2), can be beneficial for such studies due to the capability to remove visual binary stars.

3.5 Photometric variability of brown dwarfs

Brown dwarfs are intermediate objects between stars and planets with temperatures below $\sim$2400 K. This temperature range resembles that of the primary targets for current observations of exoplanet atmospheres. Since brown dwarfs share many physical and chemical processes with gas-giant exoplanets, understanding their atmospheres is also essential for studying these exoplanet atmospheres.

Many brown dwarfs reportedly show large photometric variations of typically up to a few percent (see Biller 2017; Artigau 2018 for reviews) with timescales similar to their rotation periods (ranging from a few hours to a day). Observed significant photometric variations in brown dwarfs are mainly attributed to the inhomogeneities of cloud opacity over their surface. Using the general circulation model (GCM), Tan and Showman (2021) recently demonstrated that cloud radiative feedback drives vigorous atmospheric circulation, producing inhomogeneities of cloud distributions over the surface. Their simulations predict more prominent variability when viewed equator-on rather than pole-on, consistent with the tentative
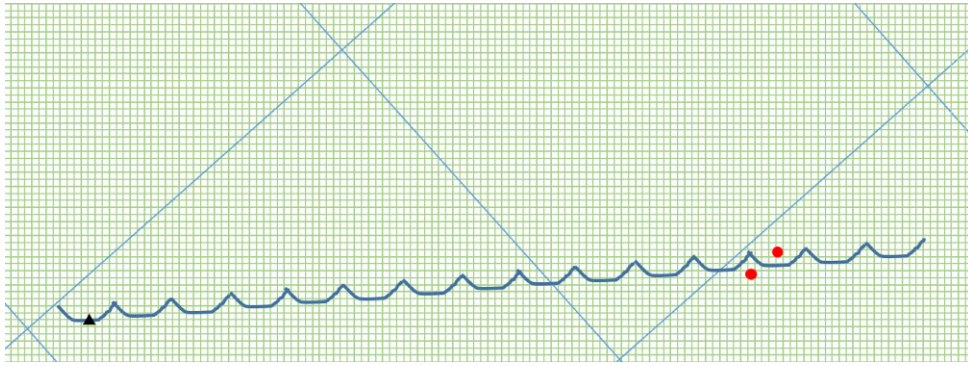
Fig. 12. Luhman 16 orbit on the TESS (cyan, 21″ pitch) and JASMINE (green, 0.″4 pitch) detector pixel grids. The red dots correspond to a projected separation of the semi-major axis of Luhman 16 AB. The triangle indicates the position, as observed by TESS in 2019 (Apai et al. 2021).

trend of current observations (Vos et al. 2020), pending further confirmation. The dependence of the variability on other parameters such as the spectral type and gravity remains highly uncertain because of the lack of samples with precise photometric monitoring. This constitutes an obstacle to obtaining detailed insights into the cause of the variability, and further understanding physical and chemical processes in the brown dwarf atmospheres. For example, if silicate clouds alone are responsible for the observed variability of brown dwarfs, one would expect the greatest variability at the L-type/T-type spectral transition. This is because those clouds start to form below the photosphere in the cold atmospheres of T-type dwarfs. On the other hand, if some other types of clouds, such as Na_2S and KCl, instead form in such cooler atmospheres (Morley et al. 2012), the trend of variability over the spectral type should be more complex (the variability amplitude should be maximized at the spectral type whose photospheres have temperatures close to the condensation temperatures of each forming cloud).

In this context, the high photometric precision of JASMINE makes it suitable for systematically performing variability observations for several brown dwarfs with different fundamental parameters (spectral type, inclination angle, gravity, and age) to reveal the trend of variability against those parameters. A recently developed dynamic mapping technique (Kawahara & Masuda 2020) makes it possible to explore the origin of the variability, namely time-varying cloud distributions, and further understand atmospheric circulation and cloud formation mechanisms in brown dwarf atmospheres. Here, we note that, owing to the rapid rotation of brown dwarfs with rotation periods of the order of hours (Biller 2017; Artigau 2018), the observation time required to monitor the global surface of a brown dwarf is relatively short. Whereas the variability observation campaign for 44 brown dwarfs was conducted using Channels 1 and 2 (3.6 and 4.5 μm) of the Spitzer Space Telescope (Metchev et al. 2015), JASMINE can perform these observations at different wavelengths (1.0–1.6 μm). Note that some of those brown dwarfs have been observed with the Wide Field Camera 3 (WFC3; 1.1–1.7 μm) of the Hubble Space Telescope (e.g., Buenzli et al. 2014), including the investigation of the spectral variability for a few targets (e.g., Apai et al. 2013; Yang et al. 2015). Because different wavelengths can probe different depths in the atmosphere, combining the observations by Spitzer and JASMINE will provide comprehensive insight into the vertical structure of the atmosphere, including clouds.

In particular, JASMINE has an excellent capability for observing brown dwarf binaries. Recently, Apai, Nardiello, and Bedin (2021) observed the precise light curves of a nearby bright brown dwarf binary, Luhman 16 AB, using TESS. Thanks to their long-term observation covering about 100 estimated rotation periods of Luhman 16 B, they succeeded in extracting several minor modulation periods of 2.5, 6.94, and 90.8 hr in the observed light curve in addition to the dominant period of 5.28 hr. They concluded that the 2.5 and 5.28 hr periods emerge from Luhman 16 B possibly due to the atmospheric waves with half and one rotation periods while the 6.94 hr peak is likely the rotation period of Luhman 16 A. As for the 90.8 hr period, they could not determine which component it originated from, but they tentatively attributed that modulation to the vortex in the polar regions. JASMINE can resolve the semi-major axis of this system corresponding to 1.″8, while TESS was unable to separate them (figure 12). Thus, JASMINE can confirm whether the 6.94 hr light-curve modulation indeed corresponds to the rotation period of Luhman 16 A. In addition, if a long-term observation is possible, the component causing the 90.8 hr modulation will be identified, which will provide detailed insights into the atmospheric dynamics of brown dwarfs.

Moreover, simultaneous observations with ground-based high-resolution spectrographs such as the Infrared Doppler (IRD, Kotani et al. 2018) mounted on the 8.2 m Subaru telescope for several best-suited targets will allow us to obtain more detailed surface maps of the temperatures and clouds for the observed brown dwarfs using the Doppler imaging technique, as done for Luhman 16 B (Crossfield 2014).

3.6 NIR photometry by JASMINE

Subsections 3.1–3.5 described the science cases that use precision NIR photometry by JASMINE. Here, we show how the required precision is attained. First, the photometric precision required to detect Earth-sized planets around M dwarf stars (subsection 3.1) is ∼0.1%, which is less stringent than that achieved by Kepler and TESS. Detecting variability in young planets and brown dwarfs requires a similar photometric precision of 0.1% (or milder). We first describe the statistical noise, including the shot noise, dark current, and readout noise of JASMINE. Next, we discuss the systematic noise caused by inter- and intrapixel fluctuations of the detector sensitivity. Finally, we consider the extent to which astrophysical noise due to stellar activity can be suppressed using an NIR passband.

3.6.1 Statistical noise

The top panel in figure 10 shows three statistical noise components, shot noise, dark current, and readout noise, as functions of the H_w magnitude. The stellar shot noise is most significant for exoplanet photometry targets. The bottom panel shows the transit depth corresponding to a detection level of 7σ in 5 min as a function of H_w. In reality, a typical transit that we search for lasts about 30 min instead of 5 min, and so the limiting depth will be a few times smaller. Consequently, one can search for a ~0.2% signal from a terrestrial planet around a $R_\star = 0.2\,R_\odot$ star that is brighter than $H_w = 11.5$ mag.

3.6.2 Impact of inter- and intrapixel sensitivity fluctuations on photometric precision

One main source of error in space-based precise photometry is an inhomogeneous detector sensitivity. Kepler and TESS avoid this systematic error by providing accurate attitude control for satellites. After its reaction wheel broke, Kepler lost precision in the attitude control to pin the stellar position in a single detector pixel. This resulted in ~1% systematic error of the aperture photometry according to the satellite drift. These systematic errors can be corrected using several techniques, e.g., pixel-level decorrelation (Luger et al. 2016). To investigate the systematic errors in the detector sensitivity, we developed a detector simulator dedicated to JASMINE, called the JASMINE-Image Simulator (JIS) (T. Kamizuka et al. in preparation). JIS simulates pixel images by incorporating both intra- and interpixel sensitivity models with attitude fluctuations. In the case of JASMINE, the point spread function (PSF) size was approximately a few times greater than the pixel size. This reduces the effect of the intrapixel fluctuation of the sensitivity, whereas the interpixel sensitivity is expected to be ~1% and it remains as a systematic error. We found that the systematic errors can be suppressed using a sufficiently sensitive detector to detect an Earth-sized planet around an M-type star after the flat correction of the interpixel sensitivity, as shown in subsection 4.3. In addition to precise measurements of the detector sensitivity prior to launch, we plan to have a single-mode fiber-type light source for the flat correction on board (T. Kotani et al. in preparation).

3.6.3 Suppression of flux modulations by stellar activity

Enhanced stellar activity poses a challenge in the search for transiting planets around young stars. Most young stars are magnetically active, often creating dark spots and plages on their surface, which are revealed as strong periodic flux modulations in the light curves. For instance, the flux variation amplitude of the young M dwarf planet host K2-33 is as large as $\approx 2\%$ (Mann et al. 2016) in the Kepler band. (In contrast, the transit depth of K2-33b is only $\approx 0.25\%$.) In the presence of such large flux modulations, together with the inflated radii of young stars, detecting "small" transiting planets (producing small transit depths) is not straightforward for young systems.

In addition, such variability can be an additional noise source, even for transit-signal detection in mature late-type stars. For the TESS passband (0.6–1.1 μm), there are approximate stellar variabilities of 400, 1000, and 4000 ppm on average for early to late M stars, corresponding to 0.35 $R_\odot$, 0.2 $R_\odot$, and 0.1 $R_\odot$ (Brady & Bean 2022), respectively. Considering the typical signal levels of terrestrial planets of 1200, 2500, and 10000 ppm for early to late M stars, flux modu-

lation due to stellar activity can be a major source of noise when searching for the transit signal of terrestrial planets in the TESS band.

Photometric monitoring in the NIR region has an advantage over optical observations in terms of the reduced flux contrast of active surface regions (spots etc). Recent radial velocity measurements (for example, Crockett et al. 2012; Beichman et al. 2019), as well as photometric observations (Miyakawa et al. 2021), revealed that the contrast of typical surface spots on young active stars is mitigated by a factor of 2–3 in the NIR region. For reference, the expected relative modulation amplitudes by stellar activity are listed in table 2, where the Kepler passband case is used as a reference and set at 1. The contrast was calculated by combining the PHOENIX atmospheric model and the response function for each passband in the same manner as in Miyakawa et al. (2021) when the stellar surface temperature and relative starspot temperature are 3500 K and 0.95, respectively. Miyakawa et al. (2022) implemented detailed simulations of the detection of close-in transiting planets around young cool stars (primarily M dwarfs). Their injection–recovery tests showed that the injected planets were recovered with enhanced rates in the NIR in all cases, and the recovery rate was significantly improved for more rapidly rotating stars ($P_{rot} < $ a few days) with larger activity-induced modulations. This highlights the remarkable benefit of performing transit surveys by NIR photometry to identify small transiting planets around particularly young active stars, such as those in the Pleiades cluster (~100 Myr) and star-forming regions ($\lesssim$10 Myr).

3.7 Exoplanet microlensing

Gas-giant planets, such as Jupiter and Saturn, are thought to have formed just outside the snow line, where icy materials are abundant. In this circumstance, a protoplanetary core grows quickly and starts accumulating the surrounding gas within the lifetime of the protoplanetary disk (for example, Ida & Lin 2004). However, the detailed process of gas-giant planet formation remains unclear. Unveiling the mass distribution of exoplanets outside the snowline is of particular importance in understanding this process. However, existing exoplanet detection techniques (except for microlensing) are insufficiently sensitive for detecting planets in this orbital region.

Microlensing detects planetary signals by observing the characteristic light curve produced by a background source star and altered by the gravitational lensing effect of the foreground planetary system. By monitoring hundreds of millions of stars in the Galactic bulge region, more than a hundred exoplanets have been detected using this technique. However, the ultra-high stellar density of the field and the large distance to the planetary systems has made it difficult to further characterize each planetary system. Although the Nancy Grace Roman Space Telescope (see sub-subsection 6.2.2) aims to improve the demographics of exoplanets substantially in the late 2020s by monitoring the Galactic bulge region (Penny et al. 2019), the difficulty of performing follow-up observations of each system remains.

This difficulty can be resolved if planetary systems are detected at close distances by microlensing. Although the event rate of such nearby planetary microlensing events is expected to be relatively small, the first such event was serendipitously discovered in 2017 (Nucita et al. 2018; Fukui et al. 2019). High-cadence, large-sky-area surveys such as the All Sky

Automated Survey for SuperNovae (ASAS-SN), Zwicky Transient Facility (ZTF), Tomo-e Gozen, and Vera C. Rubin Observatory's Legacy Survey of Space and Time (LSST) have the potential to find more such events.

JASMINE can play an invaluable role in following up such nearby planetary microlensing event observations from the ground. First, the high astrometric capability of JASMINE allows the centroid shift of the source star to be measured, thanks to the lensing effect (the signal is typically ∼1 mas). This will help to solve the degeneracy between the mass and distance of the lens system. Secondly, by simultaneously observing the same event from JASMINE and from the ground, one can measure the parallax effect in the microlensing light curve, which will also help solve for degeneracy. Thirdly, the NIR light curve from JASMINE allows the luminosity of the lens (host) star to be measured, thereby providing additional information about the host star in addition to its mass and distance (e.g., temperature). We note that although the GCS data will automatically provide all the required data, if events happen in the JASMINE GCS field, a full utilization of the advantages of JASMINE requires a target-of-opportunity (ToO) mode that can respond to a trigger within a few days.

3.8 Astrometric planet survey

The astrometric detection of exoplanets has two key advantages over other exoplanet detection methods. First, the astrometric signal increases for planets more distant from their host stars, making this method complementary to the radial velocity and transit methods, which are sensitive only to short-period planets. Secondly, the two-dimensional motion of a star measured by astrometry, combined with Kepler's laws and an estimated stellar mass, allows a solution of both the absolute mass and the complete planetary orbit. This is generally not possible for exoplanets discovered based on radial velocities or microlensing.

The astrometric signal (maximum shift of the stellar position by a planet) is given by

$$a_s \sim 30 (M_p/M_{Jup})(M_s/M_\odot)^{-1}(a/3 \text{ au})(d/100 \text{ pc})^{-1} \mu\text{as},\quad(1)$$

where M_p denotes the planetary mass, M_s the stellar mass, a the semi-major axis, and d the distance to the planetary system. Although few exoplanets have been detected to date by this technique alone, Gaia is expected to detect tens of thousands of Jovian planets at a few au around solar-type stars using this technique (Perryman et al. 2014) because of its ultra-high astrometric precision at optical wavelengths (∼25 μas for stars with $G < 15$ mag). However, it remains difficult for Gaia to detect planets around ultra-cool dwarfs and/or long-period planets because of their lack of sensitivity. JASMINE can complement Gaia exoplanet exploration with its NIR capability and the long time baseline between Gaia and JASMINE. In the following subsections, we describe several scientific cases that JASMINE can pursue.

3.8.1 Planets around ultra-cool dwarfs

Core-accretion theories predict that massive planets are less abundant around lower-mass stars because of the lack of materials in the surrounding protoplanetary disks (for example, Ida & Lin 2005). However, some Jovian planets have been discovered around mid-to-early M dwarfs, challenging current planet formation theories (for example, Morales et al. 2019).
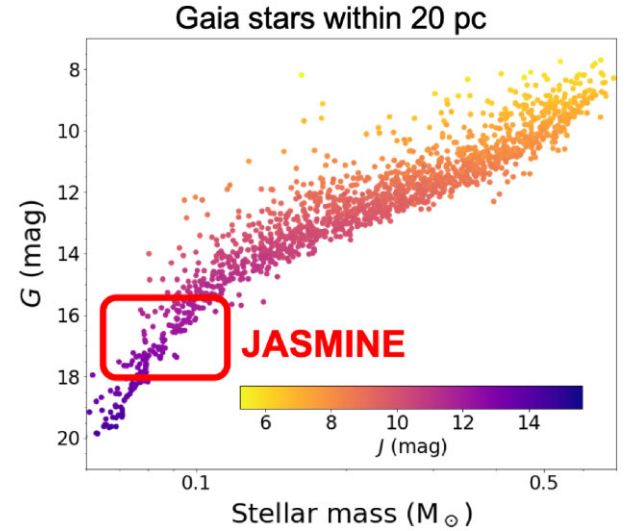

Fig. 13. Gaia G-band (y-axis) and 2MASS J-band (colors) magnitudes of the stars within 20 pc as a function of the stellar mass (x-axis). The UCD region to which JASMINE is sensitive to planets comparable to or higher than Gaia is indicated by the red box.

To further address this problem, it is important to unveil the planet population around further lower-mass stars or ultra-cool dwarfs (UCDs; $T_{eff} \lesssim 3000$ K). So far, only a limited number of planets have been discovered around UCDs owing to their faintness at optical wavelengths.

The astrometry technique is very sensitive to distant planets around nearby UCDs because the astrometric signal increases inversely with the stellar mass. For example, the astrometric signal on a 0.1 $M_\odot$ star at a distance of 20 pc caused by a planet with a mass of 0.1 M_{Jup} and an orbital period of 20 yr reaches ∼500 μas. Because Gaia alone is likely to find it difficult to firmly detect such planets owing to the faintness of nearby UCDs in the optical ($G > 16$ mag) and the limited time baseline (∼10 yr), JASMINE could play an essential role in confirming the candidates of such planets that will be detected by Gaia due to the NIR brightness of nearby UCDs ($J \sim 12$–14 mag; see figure 13), and the time baseline between Gaia and JASMINE (up to ∼18 yr).

3.8.2 Planet search in the Galactic Center survey

The data obtained by intensive observation with JASMINE toward the Galactic Center (section 2) will also be useful when searching for exoplanets using the astrometric technique. Despite the limited number of nearby stars within the JASMINE GCS area that are suitable for this planetary search, the expected astrometric precision toward this region (25 μas) will provide a good sensitivity to low-mass planets (down to ∼Neptune mass) around M dwarfs. Potentially, about a thousand M and K dwarfs that are bright enough for JASMINE are located within the GCS region (most within 1 kpc), providing good targets for an astrometric planetary search.

3.8.3 Synergy with radial velocity and direct imaging

Astrometry has good synergy with radial velocity and direct imaging techniques. Although the radial velocity technique is sensitive to long-period (tens of years) planets, this method alone cannot measure the orbital inclination. Thus, it cannot measure the true value but only the lower limit of the
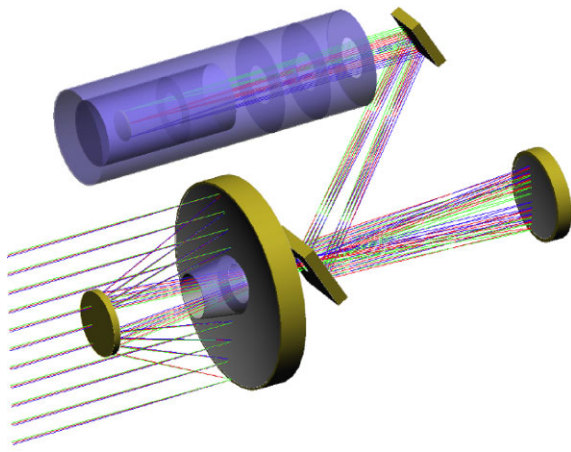
Fig. 14. Preliminary optical design of JASMINE.

Fig. 15. Example of a schematic view of the payload layout.

planetary mass. By measuring the astrometric signal of the host star of such a planet, one can determine the complete orbit and mass of the planet (for example, Feng et al. 2019). JASMINE can play an important role in measuring the true mass of long-period planets (planetary candidates) around nearby M dwarfs discovered by radial velocity surveys, such as the one that is ongoing with Subaru/IRD. Astrometry can also play a crucial role in determining the formation scenario of young self-luminous planets discovered by direct imaging. Although direct imaging can measure the complete orbit and luminosity of a planet, it alone cannot measure the dynamic mass of the planet, which is key to distinguishing different formation scenarios, i.e., hot and cold start models. Recently, the accelerations of host stars of several direct imaging planets were measured by combining the Hipparcos and Gaia proper motions, constraining their formation scenarios (for example, Dupuy et al. 2019, 2022). JASMINE will be able to contribute to such studies in combination with Gaia.

4 Mission and instrument concept

In this section we summarize the current concept study of the JASMINE mission and the survey plan to achieve the above-mentioned main science objectives of the Galactic Center archaeology and the HZ exoplanet search. The mission and instrument concepts are still under development. Hence, the specifications summarized in this section are subject to change during the further development phases of the mission.

4.1 Satellite and payload design

The satellite system of JASMINE consists of a bus module and a mission module. The mission module includes a telescope and electronics box. A large Sun shield and telescope hood are installed to protect the telescope from stray light and temperature change. The JASMINE satellite will be launched by the JAXA Epsilon S Launch Vehicle from the Uchinoura Space Center in Japan. JASMINE will be in a Sun-synchronous low-Earth orbit at an altitude of about 600 km with a mission lifetime of 3 yr. The weight of JASMINE is about 600 kg.

JASMINE has a circular primary mirror with a diameter size of 36 cm. The current preliminary optical design adopts a modified Korsch system with three mirrors and two folding mirrors to fit the focal length (4.37 m) into
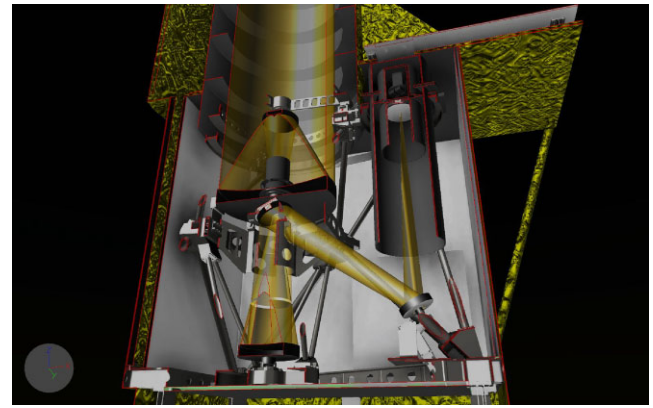
Table 3. Summary of the specifications of JASMINE.

Launch vehicle	JAXA Epsilon S
Mass	~600 kg
Volume	1 m^3
Power	600 W
Orbit	600 km Sun-synchronous orbit
Downlink	Omnidirectional X band
Mission lifetime	3 yr
Telescope	Modified Korsch system
Aperture	36 cm diameter
Focal length	4.37 m
Field of view	$0°\!\!.55 \times 0°\!\!.55$
Detector	Hamamatsu Photonics InGaAs
Number of detector	4
Number of pixels	1952×1952
Wavelength range	$H_{\rm w}$ band (1.0–1.6 μm)
Pixel size	472 mas

the size of the payload (figure 14). JASMINE is planned to use CLEARCERAM®-Z EX for the mirror and Super-Super Invar alloy (Ona et al. 2020) for the telescope structure. CLEARCERAM®-Z EX and Super-Super Invar have extremely low ($0 \pm 1 \times 10^{-8}$ K^{-1} for CLEARCERAM®-Z EX and $0 \pm 5 \times 10^{-8}$ K^{-1} for Super-Super Invar) coefficients of thermal expansion (CTE) at about 278 K, which is the operation temperature of the telescope. JASMINE uses four Hamamatsu Photonics InGaAs NIR detectors (the performance of a prototype model with a smaller format can be found in Nakaya et al. 2016). The FoV is $0°\!\!.55 \times 0°\!\!.55$. JASMINE uses an $H_{\rm w}$ filter that covers 1.0–1.6 μm. Figure 11 shows the $H_{\rm w}$ passband.

The whole telescope is encased within the "telescope panel box" that insulates the telescope from outside (figure 15). This enables precise control of the temperature variation of the telescope within $0°\!\!.1$ for 50 min, by keeping the temperature change inside the telescope panel box within 1 degree. The operation temperature for the detector is required to be less than 173 K and the temperature variation is required to be kept within the 1 degree level for 50 min. The structural thermal stability will keep the position of stars on the focal plane within 10 nm for 50 min. This is achieved by the above-mentioned thermal control and the extremely low CTE of the CLEARCERAM®-Z EX mirror and Super-Super Invar telescope structure. A summary of the specifications of the satellite and telescope is shown in table 3.
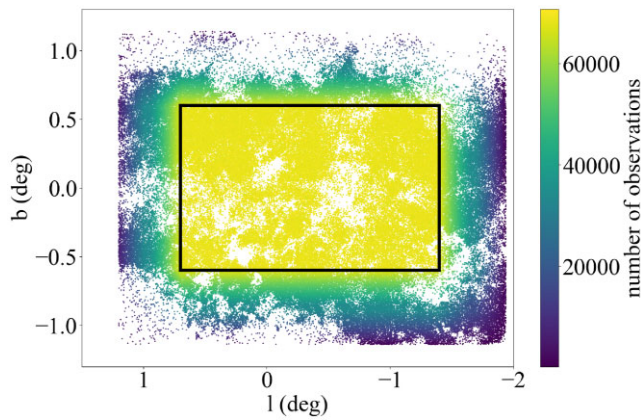
Fig. 16. Number of observations for each star observed towards the Galactic Center. The black rectangle highlights the JASMINE GCS field.

4.2 Galactic Center survey strategy

The GCS is designed to achieve the science goals in section 2. To achieve precise astrometric accuracy, JASMINE will observe the same field repeatedly (about 60000 times). The GCS field covers a rectangular region of $-0°.6 < b < 0°.6$ and $-1°.4 < l < 0°.7$ (or $-0°.7 < l < 1°.4$) as described in section 2. With a finite mission lifetime, the survey area on the sky is limited to ensure good astrometry, i.e., a sufficient number of repeat observations for each object. The JASMINE GCS is designed to cover the NSD (subsection 2.3). The GCS covers both sides of the longitudes and latitudes of the central part of the NSD ($-0°.6 < b < 0°.6$ and $-0°.7 < l < 0°.7$). On the other hand, a compromise must be made for the outer part of the NSD, i.e., observing only one side of the disk, considering the apparent symmetry of the NSD.

The whole GCS region will be mapped with a strategy to observe all the stars in this region a similar number of times during the three years of the nominal operation period of JASMINE and detect each star at different positions within the detector, to randomize the noise and reduce systematic biases. The expected number of observations for the stars in and around the GCS region is shown in figure 16. As can be seen from the figure, a number of stars surrounding the GCS region will be observed throughout the mission operation, though with a lower samping rate. Although the accuracy of the astrometry will be worse in this surrounding region, we will downlink the data for stars in this region and analyze their time-series astrometry and photometry.

At each pointing of a single field of view of $0°.55 \times 0°.55$, JASMINE takes a 12.5 s exposure (plus 1 s of readout time) 46 times; these are combined to one frame that is hereafter defined as a "small frame." The exposure of 12.5 s corresponds to the saturation limit of $H_w = 9.7$ mag. Although the pixel resolution of each image is $0''.472$, we will determine the centroid position of the stars with an accuracy of about a 4 mas level for stars brighter than $H_w = 12.5$ mag, using the effective point spread function (ePSF, Anderson & King 2000).

The parallax accuracy of 25 μas for stars brighter than 12.5 mag is obtained by the repeated observation of about 60000 times in 3 yr. In each orbit of about 97 min, JASMINE will observe four different small frames within 48% of each orbit.[5] Two of these fields overlap by about half the size of

---

[5] The number of different fields observed per orbit is to be determined when the various trade-off studies are finalized.
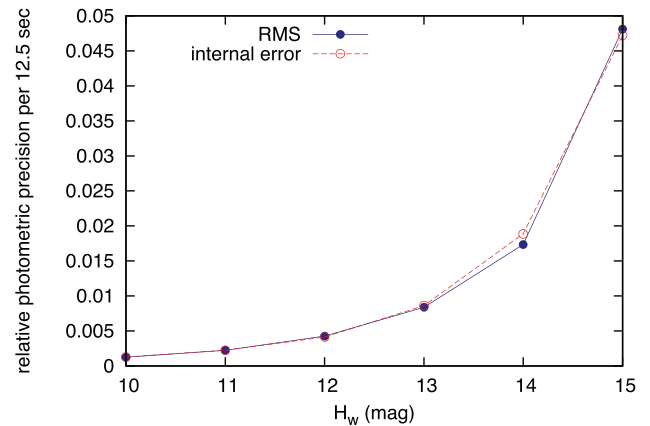

Fig. 17. Estimation of the uncertainties per single exposure of 12.5 s as a function of the magnitude of the stars. Red circles connected with the dashed line labeled as "internal error" present the photometric errors computed from the Poisson noise and the readout noise. The solid blue circle connected with the blue line labeled with "RMS" shows the photometric errors computed from the RMS error of the photometric measurement of 100 simulated images for each brightness of a star created with JIS (sub-subsection 3.6.2).

the field of view (either shifted vertically or horizontally, so that there will be two directions of overlap) to correct the distortion of the images due to optical distortion and detector distortion. The observed fields in each orbit are chosen to map the main survey field homogeneously, but as randomly as possible. The distortions of the images are modeled with two-dimensional fifth-order polynomial functions by assuming that the primary stars do not move in the short observational time in a single orbit. Here, the primary stars are defined as stars that do not have an intrinsic shift due to binaries or microlensing. As mentioned above, the telescope is stable enough to keep the position of stars on the focal plane to within 10 nm for 50 min, which allows us to ignore the time variation of the coefficients of the terms higher than the first order of the polynomial functions for the distortion correction, and maintain 10 μas stability of astrometric measurement. The time variation of the first order of the distortion, expansion and contraction, will be modeled with the stars whose parallax and proper motion is accurately measured with Gaia.

The time-series photometry can be obtained from the GCS data. Figure 17 shows the expected photometric uncertainties for a single exposure. The figure shows that the photometric accuracy is about 1 mmag for bright stars with $H_w = 10$ mag, but reaches 40 mmag for faint stars ($H_w = 14.5$ mag) in a small frame. Here, we assume that the inter- and intrapixel sensitivity fluctuations are completely calibrated. The internal error in figure 17 indicates the photometric errors computed from the Poisson noise and the readout noise. "RMS" shows the photometric errors computed from the RMS error of the photometric measurement of 100 simulated images created with JIS (sub-subsection 3.6.2), which is almost consistent with the internal error. Each star is expected to be observed every ~530 min.

Because of the limited downlink capacity, only the data of 9×9 pixels around the target stars are planned to be downlinked to the ground station. For these selected window regions, the data of every exposure, i.e., 46 images per small frame, will be downlinked, and will be used for astrometry and
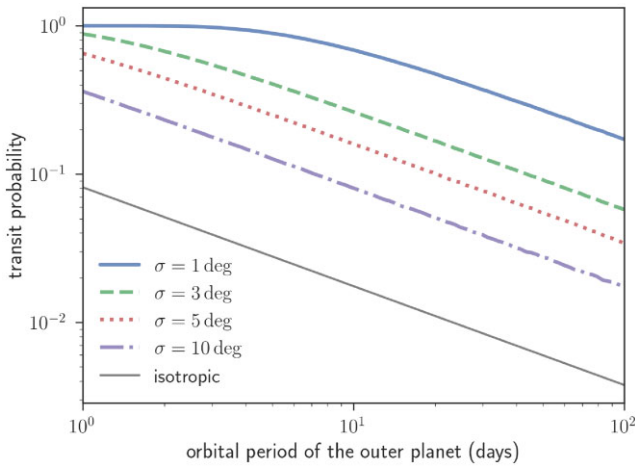
Fig. 18. Geometric transit probability of an outer planet, given the presence of an inner transiting planet, as a function of the different distributions of the mutual inclination of multiple planets. We assumed $M_\star = 0.2 M_\odot$, $R_\star = 0.2 R_\odot$, for Rayleigh distributions (with σ as the mutual inclination distribution) and for an isotropic distribution.

time-series photometry analysis. However, we plan to downlink at least one full-frame image per small frame, and make these data immediately available for the community. Such full-image data would be valuable for serendipitous discovery of any transient event. In addition, we can downlink all exposure data in a few additional pre-selected small regions. For example, Sgr A* occasionally flares up in the near-infrared, and an extremely bright flare was observed in 2019. Converting from the reported magnitudes in the H and K' bands in Do et al. (2019), the observed peak magnitude of the 2019 flare corresponds to about $H_w = 18$ mag. This is out of reach for a single exposure of the JASMINE GCS. However, 46 stacked images per single pointing can detect such a flare. Depending on the scientific merit and the downlink capacity, we can downlink all exposure data of a small region around Sgr A* and monitor the stacked flux.

4.3 Exoplanet survey strategy

The field of view of JASMINE ($0°.55 \times 0°.55$) makes it better suited to pointing–individual–target (PIT) observations than to a blind transit survey. Because the probability that an HZ planet transits a randomly chosen mid M star is only $\mathcal{O}(1\%)$, and because the orbital period of the HZ planet is $\mathcal{O}(\text{week})$, hundreds or more of such stars need to be monitored for at least a month to detect those planets in a blind transit survey. This is impractical with JASMINE.

Instead, JASMINE plans to focus on fewer [$\mathcal{O}(10)$] target stars that have a high prior probability of having transiting planets in the HZ. Specifically, we focus on stars with known transiting planets with orbital periods shorter than those in the HZ (i.e., $\lesssim 10$ d), which have been detected by ground- and/or space-based surveys prior to JASMINE. If these planets also have an outer planet in the HZ whose orbit is likely aligned with the inner transiting planet(s), the HZ planet is much more likely to transit than around a randomly chosen star: for mutual orbital inclinations of a few degrees, as inferred for multiplanetary systems from Kepler (Fabrycky et al. 2014), the transit probability for the HZ planet conditioned on the presence of inner transiting planets is a few tens of percent (figure 18). Such undetected HZ planets may be de-

tected with long-term follow-up monitoring using JASMINE. This strategy makes it plausible to find HZ transiting planets by monitoring $\mathcal{O}(10)$ targets. Indeed, the effectiveness of such a strategy has been demonstrated by Spitzer observations of TRAPPIST-1. They revealed five more terrestrial planets, d–g (Gillon et al. 2017) on wider orbits covering the HZ than planets b and c, which were originally reported from a ground-based survey (Gillon et al. 2016).

To identify transiting planets in the HZ, JASMINE needs to monitor each star for at least a few weeks in total, and the survey is planned to be performed during the periods when the Galactic Center is not observable. Because JASMINE can observe the region within $45°$ around the Sun, such observations are feasible for most stars in the sky (figure 19). Here the white dots show the locations of potential target M dwarfs, the color corresponds to the total number of visible days per year, and the gray area corresponds to the region around the Galactic and anti-Galactic Centers. Even excluding those latter regions, many mid or late M dwarfs can be observed with a sufficiently long baseline time. In principle, the anti-Galactic Center direction could also be observed for the exoplanet survey during the astrometric survey of the Galactic Center. However, this may affect the thermal stability of the astrometric survey. A more detailed thermal stability analysis is needed to determine the visibility in the anti-Galactic direction.

Figure 20 shows a simulated light curve of a mid-to-late M-type star that includes a transit signal by a terrestrial planet. This simulation includes photon noise, dark current, readout noise, and systematic error from intra- and interpixel sensitivity fluctuations, incorporating attitude control error of the satellite and a PSF of the optics with wavefront aberrations expressed by Zernike polynomials. An Earth-sized planet around a star with $R_\star = 0.2 R_\odot$ yields a transit signal of $\sim 0.2\%$–0.3%, which can be detected in the simulated light curve of JASMINE after the flat correction of the interpixel sensitivity (see sub-subsection 3.6.2 for details).

5 Other potential science cases

5.1 Galactic mid-plane survey

While the Gaia mission is creating groundbreaking advances in the exploration of the structure and kinematics of the Galaxy as mentioned above, Gaia's contributions to understanding the large-scale dynamics of the youngest populations of the disk ("Extreme Population I") will necessarily be limited, as even $1°$ of latitude is the scale height of these populations at a distance of about 5 kpc. Yet it is within this $\lesssim 100$ pc from the Galactic mid-plane that the main acting fields of the primary agents of disk dynamical evolution are, e.g., giant molecular clouds, the spiral arms, and the densest parts of the Galactic bar. To gather a complete understanding of processes such as secular orbital heating and radial migration that are driven by these perturbations requires contiguous kinematic information spanning the very youngest stars born in the Galactic mid-plane to their older siblings (well studied by other surveys) that have long since been scattered to dynamically hotter and/or radially migrated orbits.

Moreover, without accurate proper motions, even surveys like APOGEE, which is providing the first global view of the detailed chemistry and radial velocities of disk and bulge stars, are limited in their ability to place this information within a

Color: visible period [d]. Points: Target stars, 9.5<H<10.5 2700<T<3300, R<0.4Rsol
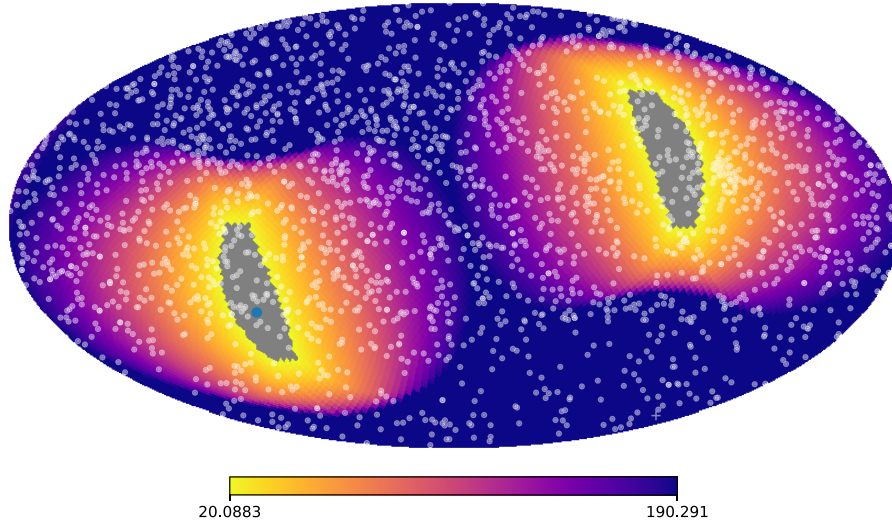

Fig. 19. Visibility of JASMINE on the equatorial coordinate system. The color indicates the total number of visible days per year. The small dots indicate the target M-type stars. The two gray areas correspond to the Galactic Center and the anti-Galactic Center, where JASMINE will conduct an astrometric survey of the Galactic Center. The blue dot indicates the Galactic Center.
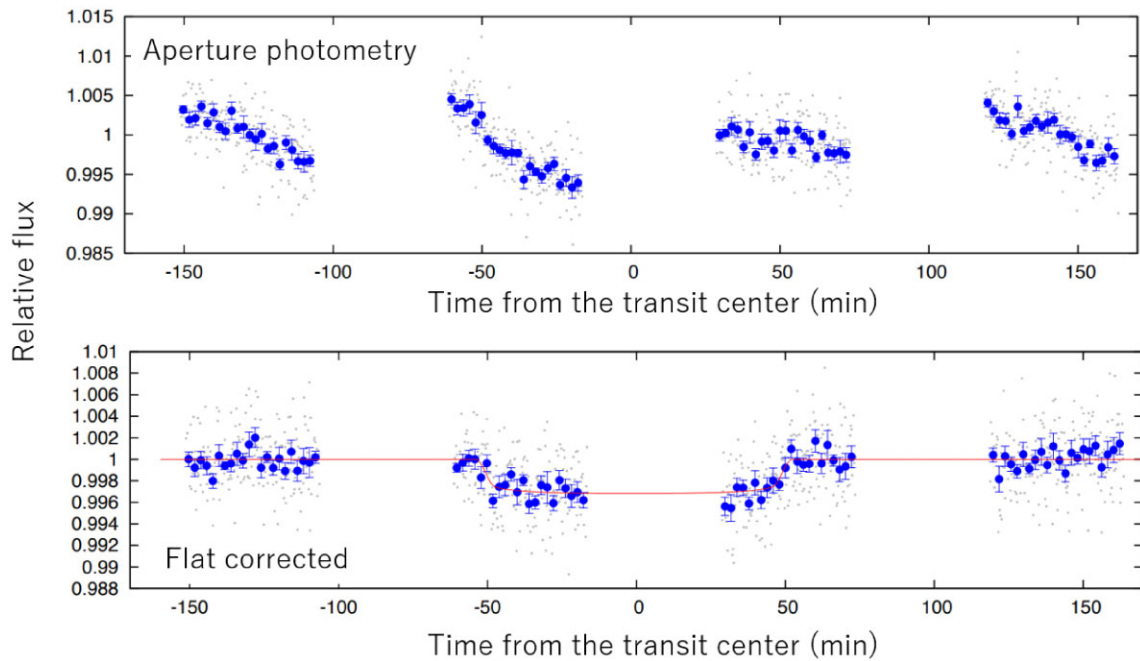

Fig. 20. Simulated transit signal assuming $R_\star = 0.2\,R_\odot$ and $R_p = 1.2\,R_\oplus$, $H_w = 10.5$ mag. The upper panel shows the light curve computed by simple aperture photometry of the simulated detector images. The detector images were computed using the JASMINE Image Simulator, which considers readout noise, dark current, inter- and intrapixel sensitivity fluctuations, attitude control error, and pointing drift. The bottom panel shows a flat-corrected version of the top panel. Flat correction is applied by using an internal flat calibration ramp and/or self-calibrated flat using bright star cluster observations in orbit.

firm dynamical context; many thousands of mid-plane stars in the APOGEE database lack Gaia astrometry, so that 3D orbits cannot be inferred. Only an NIR astrometry facility can remedy this problem by supplying a similar global view of mid-plane stellar disk dynamics. The importance of accessing this "optically hidden Milky Way" has motivated discussions at ESA to follow Gaia up with an NIR counterpart mission, GaiaNIR (e.g., Hobbs et al. 2021), but this is not likely to be realized for a few decades.

JASMINE is well suited to be a pathfinder for a proposed large flagship all-sky astrometric survey mission in the NIR, like the GaiaNIR concept, and is capable of having an immediate impact in the field of Galactic archaeology. In addition to the GCS in section 2, to address the science objectives of the inner disk dynamics summarized in subsection 2.6, tracing the dynamics and chemistry of the stars in the Galactic disk mid-plane at the various azimuthal angles of the disk is required. One potential targeting strategy is a small campaign

of mosaicked JASMINE pointings, which are centered on the location of APOGEE $b = 0°$ fields, which are located about every 5° in longitude around the entire sky. Such a strategy will instantly pay dividends through the value-added information on tens of thousands of stars with spectroscopy from the APOGEE and APOGEE-2 surveys, and their SDSS-V extension, Milky Way Mapper (see subsection 6.1.3), that will lack Gaia's accurate astrometric data, because of the extreme foreground obscuration. These data will provide a systematic probe of the dynamics of the low-latitude disk.

The required astrometric accuracy should not be as strict as the GCS. Although APOGEE spectroscopy yields ~ 0.1 km s^{-1} accuracy radial velocities for stars, we do not require such accuracy in the transverse velocities. This is because we are primarily interested in measuring the velocity dispersions for young Population I stars, which are of the order of 10–30 km s^{-1} per dimension. For example, 200 μas yr^{-1} proper motion provided by JASMINE translates to a transverse velocity error of <5 km s^{-1} for a star at 5 kpc (this is a bit higher than the approximate median distance of the APOGEE midplane stars, which are primarily red giants), and <10 km s^{-1} for stars at 10 kpc. This relaxed requirement allows us to survey a large range of the galactic longitude, when JASMINE is not observing primary science targets.

5.1.1 Star-forming region

A rigid adherence to the pointing strategy of the Galactic midplane survey is not necessary, and other interesting science problems, e.g., astrometric and photometric exploration of young stellar clusters and star-forming regions (which naturally lie at low latitude), can also benefit from judicious placement of the JASMINE Galactic mid-plane survey "pickets." For example, the APOGEE project has dedicated itself to intense spectroscopic probes of several star-forming regions (e.g., the Orion Complex, the Perseus Molecular Cloud, and the Cygnus region), which may also be matched with JASMINE targeting.

Stars are mainly formed in giant molecular clouds (GMCs). Moreover, star-forming regions strongly concentrate into very compact sections within GMCs. Using the Two Micron All Sky Survey (2MASS) point source catalog, Carpenter (2000) estimated the fraction of young stellar populations contained within clusters to be 50%–100% for nearby cluster-forming GMCs, such as Perseus, Orion A, Orion B, and MonR2. NIR surveys of young stellar populations using the Spitzer Space Telescope have confirmed that clustered star formation is the dominant mode of star formation in the Galaxy (e.g., Poulton et al. 2008; Román-Zúñiga et al. 2008).

This traditional picture is now challenged by the recent Gaia data releases, which are revealing a more complex reality. Anders et al. (2021) claimed that only about 16% of the stars in the solar neighborhood formed in bound clusters, comparing the star formation rate in the solar neighborhood and the populations of the young star clusters. From the more small-scale kinematics of the OB associations, Ward, Kruijssen, and Rix (2020) showed that the velocity fields of the OB association are highly substructured (see also Wright & Mamajek 2018), which is not consistent with a monolithic scenario, where stars formed in the core of bound clouds and expanded subsequently due to the outflow of the gas caused by feedback. They discussed that these are consistent with a hierarchical star formation model, where stars formed in large-scale gravitationally unbound structures in molecular clouds.

Although the Gaia data is revolutionizing our understanding of star formation, these optical observations are unavoidably missing information from deep in the core of star-forming regions where the dust extinction is too severe. The NIR astrometric observations with JASMINE and APOGEE spectroscopic data can unveil the whole picture of the star-forming region hidden in the dust, which will complement what the Gaia data have revealed and provide a more complete picture of these star-forming regions.

5.1.2 Milky Way neighborhood dwarf galaxies

The dwarf galaxy population around the Milky Way is diverse and new dwarfs are continuously being discovered (e.g., Willman et al. 2005; Belokurov et al. 2006; Zucker et al. 2006). The once-troublesome "missing satellites problem" that plagued the ΛCDM cosmology theoretical framework is now steadily being refined and coming in line with observations of the dwarf galaxy populations around more massive galaxies such as the Milky Way (Simon & Geha 2007; Kim et al. 2018; Mao et al. 2021). The ESA F-class mission ARRAKIHS (a planned 2030 lanuch) will further this inventory with unprecedented surface brightness levels in the Euclid VIS- (0.550–0.900 μm), Y- (0.920–1.230 μm), and J- (1.169–1.590 μm) band images of nearby galaxies. One remarkable discovery that came from the recent Gaia DR2 is that of the giant dwarf galaxy Antlia 2 (Torrealba et al. 2019). The primary reason that this giant dwarf galaxy lurking in the dark matter halo of the Milky Way went undetected until now is that it lies only 11 degrees off the Galactic plane. Where Gaia has run into the limit of visual-wavelength extinction, JASMINE can go deeper into the Galactic mid-plane, as part of the Galactic mid-plane survey, allowing for serendipitous dwarf galaxy and globular/stellar cluster discoveries that cannot be made via any other method. With the anticipated astrometric precision and stellar content, we will be able to detect over-densities of stars that contain common proper motions indicative of low-latitude dwarf galaxies and/or clusters that are in the optical Zone of Avoidance, within a distance of about 10 kpc, as demonstrated for Gaia data in Antoja et al. (2015) and Ciucă et al. (2018). So far, there is no dwarf galaxy found within 20 kpc, and Draco 2 at about 22 kpc is the closest (e.g., McConnachie & Venn 2020). Although the total field of view of the Galactic mid-plane survey is very limited, finding any galaxy within 20 kpc will be a significant discovery, and will be integral to studies of the survivability of dwarf galaxies within the inner Galaxy, their contribution to the bulge, and their impact on the Galactic disk (e.g., D'Onghia et al. 2010).

5.2 X-ray binaries

Another interesting target for which the precise astrometry with short-cadence observations of JASMINE can provide unique and impactful data is X-ray binaries, including gamma-ray binaries (Aharonian et al. 2005). These are ideal laboratories for the study of high-energy astrophysics and prime future targets for multi-messenger astronomy, including continuous gravitational wave observations (e.g., Middleton et al. 2020). Astrometric measurements of their companion stars enables us to measure the physical scale of the orbital parameters, and to unveil the mass of the compact object, whether it be a white dwarf, neutron star, or BH (Yamaguchi et al. 2018b; see also sub-subsection 5.3.1). We list below examples of X-ray binaries, which are particularly

interesting targets for JASMINE, when JASMINE cannot observe the GCS field. This merely presents examples of potential targets, and is not an exhaustive list.

γ Cassiopeia (γ Cas): γ Cas is considered to be the first star identified as a Be star (a B type star with emission lines) (Secchi 1866). However, now γ Cas is known to be a rare kind of Be star, which is characterized by a hard X-ray spectrum with a thermal X-ray emission, a high temperature (>10 keV), and a lack of strong variability (e.g., Motch et al. 2015; Nazé & Motch 2018; Tsujimoto et al. 2018). Despite the proximity of the object ($d \sim 168$ pc) (van Leeuwen 2007) and several decades of observational and theoretical studies, the X-ray emission mechanism and the nature of the lower-mass secondary star are still debated (e.g., Smith 2019; Langer et al. 2020). While the $\sim$204 d binary period with an orbit that is close to circular (Miroshnichenko et al. 2002; Nemravová et al. 2012) is known, the mass of the smaller-mass secondary star is not well measured and it is still debated whether the secondary star is a white dwarf or a neutron star (Langer et al. 2020). With a visual magnitude of $\sim$2, γ Cas is too bright for Gaia. JASMINE can adjust the exposure time to observe such a bright object with a short cadence. Such time-series astrometric information will provide the precise orbital parameters and mass of the secondary star from astrometric observations (Yamaguchi et al. 2018b), which will be a crucial to understanding the long-debated properties of γ Cas and other similar systems (γ Cas analogs).

LSI +61 303/HESS J0632+057: These are both gamma-ray binaries, in which the source of gamma rays may be the impact of a relativistic pulsar wind on outflowing protons in the disk of a Be star, UV photons from a massive main-sequence star, or by the interaction of UV photons from such a star on the accretion disk of an X-ray binary counterpart (Mirabel 2012). Determining the masses of these companions can be achieved with high astrometric precision observations.

X Per/V725 Tau: Like γ Cas, these are X-ray binaries with rapidly rotating B stars, and likely host neutron star companions. Neutron stars are **characterized** by their equation of state, which requires knowing their masses (e.g., Demorest et al. 2010). This can be done with precise determination of orbital parameters (Miller 2013).

5.3 Complementary sciences with the Galactic Center survey data

The JASMINE GCS data will provide accurate astrometry and time-series photometry for all the stars with 9.5 mag < H_w < 14.5 mag in the JASMINE GCS field. The GCS data should be valuable for a wide range of scientific studies, not just for the core science of JASMINE as shown in section 2. In this section, we highlight some of these science cases. Note that the aim of this section is not to provide a comprehensive list, but merely to list the potential science cases. We hope that many science cases that are not as premeditated will be developed by the wider science community.

5.3.1 Hunting inner disk BHs

Massive stars are expected to become BHs upon their demise (e.g., Maeder 1992). Therefore, it is expected that there are many stellar-mass BHs floating around in the Milky Way (e.g., Brown & Bethe 1994). Stellar-mass BHs are found in the Galaxy as X-ray binaries (e.g., Özel et al. 2010), whose

masses are around 5–20 $M_\odot$. Several gravitational wave detections of stellar-mass BH binaries since the first detection of GW150914 by the LIGO/VIRGO collaborations (Abbott et al. 2016) revealed that there are indeed stellar-mass BHs, up to $M_{\rm BH} \sim 150\ M_\odot$ (Abbott et al. 2020). Two remaining questions are what is the mass function of this BH population, and how they are spatially distributed in the Galaxy? These questions are also related to the origin of SMBHs, as discussed in subsection 2.2.

One promising method to detect a large population of these stellar-mass BHs is finding a binary system of a BH and a companion star bright enough to allow for its kinematics to be measured with astrometry and/or spectroscopic observations. These systems do not require the companion star to be interacting with the BH and emitting X-rays, i.e., a non-interacting BH (Thompson et al. 2019). Such non-interacting BHs are expected to be observed by the precise astrometry available with Gaia (e.g., Penoyre et al. 2022). Recently Shikauchi, Tanikawa, and Kawanaka (2022) estimated that Gaia will detect $\sim$1.1–46 non-interacting BH binaries (see also Kawanaka et al. 2017; Yamaguchi et al. 2018a). In fact, so far from Gaia DR3 and follow-up observations, two non-interacting BH binaries, Gaia BH1 with a Sun-like star (Chakrabarti et al. 2023; El-Badry et al. 2023a) and Gaia BH2 with a red giant star (Tanikawa et al. 2023; El-Badry et al. 2023b), have been found. JASMINE will offer similarly precise astrometry for stars in the inner disk from the Sun to the Galactic Center, where Gaia cannot observe due to the high extinction. Therefore, JASMINE is expected to uncover the population of BHs in the inner Galaxy. According to a similar model of Shikauchi, Tanikawa, and Kawanaka (2022), in the JASMINE GCS region 100–1000 BH–star binaries are expected to exist. Further study of how many such binaries can be detected by JASMINE is ongoing.

Another way of hunting for BHs with JASMINE is microlensing. JASMINE will offer time-series photometry of the Galactic Center region where the stellar density is very high. We expect that JASMINE will find about three microlensing events during the nominal operation of 3 yr, which is an optimistic estimate based on the VVV microlensing survey results (Navarro et al. 2020). As suggested by Abrams and Takada (2020), long-timescale (>100 d) microlensing events are expected to be dominated by a high-mass ($\gtrsim$30 $M_\odot$) BH lens. Photometric microlensing itself does not give us the lens' mass. However, JASMINE can also detect astrometric microlensing from the centroid shift of the source (e.g., Dominik & Sahu 2000; Belokurov & Evans 2002). Astrometric microlensing enables us to measure the source mass if the mass and distance to the lens are optimum for the measurement. Recently, the first astrometric microlensing measurement has been reported for a microlensing event found by ground-based observation and followed up by the Hubble Space Telescope for astrometry (Lam et al. 2022; Sahu et al. 2022). However, the lens masses for the same event, OGLE-2011-BLG-0462/MOA-2011-BLG-191, reported by the two teams are so far quite different. Sahu et al. (2022) reported a lens mass of 7.1 ± 1.3 $M_\odot$, clearly indicating a BH, at distance of 1.58 ± 0.18 kpc, while Lam et al. (2022) reported a lens mass of 1.6–4.2 $M_\odot$, which could be a neutron star or BH, at a distance of 0.69–1.37 kpc. This tension could be due to systematic uncertainty from the two independent measurements of photometry and astrometry. The astrometric displacement of this event was larger than 1 mas and large enough to be clearly detected

by JASMINE. JASMINE can provide both photometric and astrometric information, which may help to reduce the systematic uncertainty of such microlensing events. The chance of having such an event in the JASMINE GCS field in the lifetime of JASMINE could be slim, but one event of precise measurement of the high-mass BH would still be an exciting outcome, because only a few such events are expected even in the Gaia data (Rybicki et al. 2018).

5.3.2 Hunting IMBHs in the Galactic Center

A pressing mystery is the low number of confidently confirmed IMBHs $M_{BH} = 100–10^5 \, M_\odot$ (Chilingarian et al. 2018). Many candidates are, however, known (e.g., Graham et al. 2021b), and they may form the low-mass ($M_{bh} < 10^5 \, M_\odot$) extension to the quadratic BH/bulge mass scaling relation for disk galaxies (Graham & Scott 2015). The Galactic Center is an attractive area to explore for these long-sought IMBHs (see Greene et al. 2020 for a review), especially if brought in through the capture of dwarf-mass galaxies. Furthermore, Portegies Zwart et al. (2006) demonstrated that some massive star clusters formed in the central 100 pc undergo core collapse before the massive stars die, i.e., ∼3 Myr, which induces a runaway stellar merger and creates an IMBH. They estimated that within 10 pc from the Galactic Center about 50 IMBHs may exist. Some of them could be still within surviving star clusters (e.g., Fujii et al. 2008), like the star clusters near the Galactic Center, the Arches (Figer et al. 2002) and the Quintuplet (Figer et al. 1999). Detecting a star cluster in a high stellar density region like the Galactic Center with only photometric data is difficult. However, the proper motion data from JASMINE will enable the detection of star clusters in the Galactic Center (see also subsection 2.3), which can inform follow-up studies of their cluster centers with X-ray and/or radio surveys (e.g., Oka et al. 2017; Tsuboi et al. 2017).

Interestingly, so far five IMBH candidates have been discovered as high-velocity (velocity width >50 km s^{-1}) compact (<5 pc) clouds in the Galactic Center (Takekawa et al. 2020). The advent of ALMA enables measurement of the detailed velocity structure of compact clouds less than 0.1 pc from the center, which is consistent with Keplerian rotation around a massive object whose inferred mass is between 10^4 and $10^5 \, M_\odot$ (e.g., Tsuboi et al. 2019; Takekawa et al. 2020). Although further studies are required to prove that they are true IMBHs, these observations may indicate that several IMBHs exist in the Galactic Center.

With JASMINE, IMBHs can be detected as a binary motion of bright stars around an IMBH or astrometric microlensing, as discussed in the previous section, if such systems exist or such an event occurs. For example, if a 1 $M_\odot$ asymptotic giant branch star is rotating around a 1000 $M_\odot$ BH with an orbital period of 3 yr with zero eccentricity at a distance of 8 kpc, the semi-major axis of the orbit corresponds to 2.6 mas, which can be detected by JASMINE.

There will be an astrometric microlensing event if an IMBH crosses in front of a distant star. Following Toki and Takada (2021), we can consider an event for a source star at 8 kpc, and a lens object of an IMBH with 1000 $M_\odot$ crossing at 7.5 kpc. The Einstein timescale of this event is 713 d, and the maximum displacement due to the astrometric microlensing is 2.9 mas (Toki & Takada 2021). This can be detected by JASMINE, though such an event would be extremely rare.

5.3.3 Gravitational waves

Gravitational waves (GWs) have been successfully detected by the Laser Interferometer Gravitational-Wave Observatory (LIGO), Virgo, and the Kamioka Gravitational Wave Detector (KAGRA) collaborations. The sources for these events are merging compact objects such as BHs and neutron stars. It is of importance to detect gravitational waves from SMBH binaries to study the growth mechanism of SMBHs. These waves have much longer wavelengths than detectable by ground-based detectors. Astrometry could be a valuable resource to detect or constrain such low-frequency gravitational waves (e.g., Klioner 2018).

Here, we estimate the strain sensitivity of the JASMINE GCS. It is well known that the maximal magnitude of the astrometric effect of a gravitational wave is $h/2$ with h being the strain. The astrometric accuracy of single observations of JASMINE is $\Delta\theta = 4$ mas for stars with magnitude $H_w < 12.5$ mag and the uncertainty grows exponentially for fainter sources. Given that each star will be observed around $N_{obs} = 68000$ times, considering a realistically expected distribution of stars in H_w magnitudes of the GCS and using the theoretical formulation developed for Gaia-like astrometry (Klioner 2018), one can conclude that the full sensitivity of JASMINE to the effects of a gravitational wave will be $h = 3 \times 10^{-13}$. Here we assume that the instrument is ideally calibrated, so that the full accuracy scales as $N_{obs}^{-1/2}$ for each source and the sensitivity is also accordingly computed from the combination of the contributions from individual sources.

However, the astrometric effect of a gravitational wave is proportional to the sine of the angular separation χ between the direction of observation and that towards the gravitational wave source (Book & Flanagan 2011; Klioner 2018). Although JASMINE produces relative astrometry only, the variation of the astrometric effect within the observed field on the sky can be detected. Therefore, the sensitivity quoted above should be scaled by $|\sin(\chi + f/2) - \sin(\chi - f/2)| = 2\sin(f/2)|\cos\chi|$, where f is the extension of the observed field, being $f \approx 2°$ for the JASMINE GCS. Therefore, the theoretical sensitivity of JASMINE can be estimated as $h = 8.6 \times 10^{-12}|\cos\chi|$. Interestingly, the maximal sensitivity is reached for gravitational sources approximately in the direction of observation or the opposite direction where $|\cos\chi| \approx 1$. This theoretical sensitivity is valid for the gravitational wave periods between the typical cadence of observations and the duration of observations by JASMINE.

5.3.4 Ultra-light dark matter

The precise measurement of the kinematics of stars revealed by JASMINE would enable us to reconstruct the mass distribution in the Galactic Center (e.g., Genzel et al. 1996; Chatzopoulos et al. 2015; see also subsections 2.1 and 2.3). It is believed that in the central 100 pc of the Galaxy baryons dominate the mass profile, and the total mass measured from the dynamical model is consistent with what is expected from the stellar density profile (e.g., Launhardt et al. 2002; Fritz et al. 2016). However, the Galactic Center is attracting interest in testing for the existence of a particular dark matter candidate, namely ultra-light dark matter (ULDM), including axion-like ULDM particles (see, e.g., Ferreira 2021 for a review). Although ULDM behaves like conventional cold dark matter on large scales, ULDM is expected to produce a

soliton core in the Galactic Center on the de Broglie wavelength scale due to Bose–Einstein condensation. Schive, Chiueh, and Broadhurst (2014) suggested that ULDM particle masses of $\sim 8 \times 10^{-23}$ eV can explain the dynamical mass profile of the Fornax dwarf galaxy (but see also Safarzadeh & Spergel 2020). Bar et al. (2018) suggested that the soliton core created from a dark matter particle mass less than 10^{-19} eV can influence the gravitational potential in the Galactic Center significantly. De Martino et al. (2020) showed that stellar velocity dispersion observed in the Galactic Center implies a soliton core as massive as $\sim 10^9 \, M_\odot$, expected from ULDM particles with $\sim 10^{-22}$ eV. Maleki, Baghram, and Rahvar (2020) also demonstrated that a soliton core corresponding to a particle mass of $\sim 2.5 \times 10^{-21}$ eV explains the rotation curve of the Milky Way in the central region. Li, Shen, and Schive (2020) showed that such a massive soliton core as suggested above can influence the kinematic properties of the nuclear gas disk on a scale of ~ 200 pc.

Recently, Toguz et al. (2022) demonstrated that the kinematics of stars in the NSC can provide constraints on the particle mass range of ULDM. Toguz et al. (2022) applied a simple isotropic dynamical model to the kinematics data of the NSC stars in Fritz et al. (2016), and rejected the mass range of ULDM between $10^{-20.4}$ and $10^{-18.5}$ eV. JASMINE will provide the precise kinematics of the stars in the NSD (subsection 2.3), which is the dominant stellar component from a few pc to ~ 200 pc. This size corresponds to a soliton core size of $\sim 10^{-19}$–10^{-22} eV ULDM. Using the dynamical modeling of these stellar structures, the precise astrometric information on JASMINE may uncover indirect evidence of ULDM or provide stringent constraints on the existence of ULDM with a particle mass between 10^{-22} and 10^{-19} eV.

5.3.5 Identifying disrupted globular cluster population

Recent observational studies of the Galactic bulge by APOGEE have discovered that a significant fraction of the bulge stars have unusually high [N/Fe] (e.g., Schiavon et al. 2017). These N-rich stars are not found in the Galactic disk, but they are ubiquitous in globular clusters. Accordingly, one of the possible scenarios for the formation of the N-rich stars in the Galactic bulge is that the stars originate from globular clusters that had been completely destroyed by the strong tidal field of the Galactic bulge. Interestingly, these N-rich stars have been discovered in elliptical galaxies (e.g., Schiavon 2007; van Dokkum et al. 2017), which suggests that N-rich populations are common in galactic bulges and elliptical galaxies, i.e., not just in the Galactic bulge, in line with the indistinguishable properties of classical bulges and elliptical galaxies (e.g., Renzini 1999; Kormendy et al. 2009; Fisher & Drory 2010).

Globular clusters can spiral into the central region of the Galactic bulge due to dynamical friction (e.g., Tremaine et al. 1975), and they can be more severely influenced by the tidal field of the bulge in the inner region. Accordingly, if such a globular cluster destruction scenario for the N-rich stars is correct, then stars from destroyed globular clusters could be a major population in the central region of the Galactic halo. In fact, using APOGEE DR16, Horta et al. (2021b) estimated that N-rich stars represent about 17% of the total halo stars at 1.5 kpc from the Galactic Center (see also Fernández-Trincado et al. 2022). JASMINE will enable us to investigate the 3D spatial distributions and kinematics of N-rich (globular cluster origin) and N-normal halo stars in the cen-

tral region through the superb accuracy of its proper motion measurement. Because the globular cluster origin stars could inherit unique kinematics different from other halo stars, such 3D dynamics of N-rich stars will contribute to our understanding of the formation of the inner bulge. In APOGEE DR17 (Abdurro'uf et al. 2022), there are 436 good-quality stars with measured [N/Fe] and [Fe/H] in the JASMINE GCS field, i.e., STARFLAG = 0, ASPCAPFLAG = 0, SNR > 70, $3250 < T_{\rm eff} < 4500$ K, and $\log g < 3$ (Kisku et al. 2021), and six of them are N-rich stars ([N/Fe] > 0.5, $-1.5 <$ [Fe/H] < 0.0). All these stars are bright enough for JASMINE to observe. Therefore, it is promising that JASMINE will provide the proper motion of a good number of N-rich stars in the Galactic Center field in combination with future high-resolution high-quality spectroscopic surveys of the Galactic Center field, which will help to discover more N-rich stars.

5.3.6 Relics of ancient mergers

An ancient galaxy merger of Gaia–Sausage–Enceladus discovered in the Gaia data (section 1) leaves questions like "where is the core of the remnant now?" and "has the core of the progenitor galaxy reached the Galactic Center?" To assess the possibility of identifying such merger remnants in the JASMINE GCS, we again use APOGEE DR17, but apply a slightly different-quality cut, i.e., STARFLAG = 0, APPCAPFLAG = 0, SNR > 70, $3500 < T_{\rm eff} < 5500$ K, and $\log g < 3.6$, following Horta et al. (2023), who used APOGEE DR17 to chemically characterize halo substructures of the likely accreted populations. We find that there are 284 APOGEE high-quality star data within the JASMINE GCS field. The Gaia–Sausage–Enceladus remnants occupy a distinct stellar abundance distribution in the [α/Fe]–[Fe/H] plane (e.g., Haywood et al. 2018b; Helmi et al. 2018; Das et al. 2020). Out of this sample, we find four stars within the abundances expected for the Gaia–Sausage–Enceladus remnants, i.e., stars with [Fe/H] < -1.1 and [Mg/Fe] < -0.28. All these stars are brighter than $H_{\rm w} = 14.5$ mag.

Note, however, that the APOGEE DR17 sample is not a complete sample up to $H_{\rm w} = 14.5$ mag, but has a sample selection due to colors and/or specific scientific targets. The JASMINE GCS will obtain the precise proper motion for about 1000 times more stars than present in the APOGEE data. Obtaining accurate proper motions and orbits of these potential remnant stars of the Gaia–Sausage–Enceladus interaction in the inner Galactic disk will allow studies to test the association with the already-measured Gaia–Sausage–Enceladus remnants, which have so far been found exclusively in the solar neighborhood.

Horta et al. (2021a) found the inner galactic structure (IGS), which has similar chemical properties to the accreted components of the Galactic halo. They suggest that this could be a relic of an ancient accretion of another galaxy in the Milky Way earlier than the Gaia–Sausage–Enceladus merger and could be a more massive progenitor than Gaia–Sausage–Enceladus. Further studies with Gaia DR3 and ground-based spectroscopic data (e.g., Belokurov & Kravtsov 2022; Rix et al. 2022) argue that such centrally concentrated metal-poor stars are relics of the ancient Milky Way proto-Galaxy, which could be mix of merger and in situ populations from the early epoch of Milky Way formation. JASMINE can provide the proper motion of the stars in the Galactic Center where Gaia cannot observe, and will help to identify the inner extension of the ancient populations.

5.3.7 Origin of hyper-velocity stars

Hills ([1988](#)) theoretically predicted that the SMBH at the Galactic Center (Sgr A*) ejects stars with extremely large velocities as a result of close encounters and disruption of stellar binaries near the SMBH. Yu and Tremaine ([2003](#)) expanded upon the possible ejection mechanisms. The discoveries of young hyper-velocity stars (HVSs) in the halo (Brown et al. [2005](#); Zheng et al. [2014](#); Brown [2015](#); Huang et al. [2017](#); Massey et al. [2018](#); Koposov et al. [2020](#)) confirmed this prediction. Among these discoveries, the most intriguing one is the A-type HVS dubbed S5-HVS1 (Koposov et al. [2020](#)). Based on the astrometric data from Gaia and a follow-up spectroscopic observation, it turns out that this star was ejected from the Galactic Center 4.8 Myr ago with an ejection velocity of $\sim$1800 km s^{-1}. Some numerical simulations suggest that the ejection rate of HVSs is around 10^{-5}–10^{-4} yr^{-1} (Brown [2015](#)). This ejection rate suggests that there are 1–10 HVSs within a sphere of radius 0.1 kpc centered at the Galactic Center, given their typical velocity $\sim$1000 km s^{-1}. Of course, what we can expect to observe with JASMINE is a tiny fraction of them, because they need to be bright enough to be detected by JASMINE. Given that the GCS area of JASMINE includes a square region of $\pm0°\!.6$ around the Galactic Center ($0°\!.6$ corresponds to about 0.09 kpc at the projected distance of 8.275 kpc), it is an enticing prospect to look for HVS candidates with JASMINE. If JASMINE discovers an HVS within $r < 0.1$ kpc from the Galactic Center, this will be very useful to understand the detailed mechanism of HVS ejection. For example, an HVS with a velocity of 1000 km s^{-1} at $r = 0.1$ kpc can be traced back to the Galactic Center by integrating the orbit backward in time for just 0.1 Myr. This means that we can probe the environment near the SMBH in the immediate past (just 0.1 Myr ago), such as the binary fraction near the SMBH or the orbital distribution near the SMBH. If JASMINE finds an HVS whose orbit is not consistent with the SMBH origin, it may indicate the existence of an IMBH, which can produce an HVS, in the Galactic Center.

5.3.8 X-ray sources and the origin of the Galactic ridge X-ray emission

The apparently extended hard ($\geq$2 keV) X-ray emission along the Galactic plane has been known as the Galactic ridge X-ray emission (GRXE) since the early 1980s (e.g., Worrall et al. [1982](#)). This emission extends tens of degrees in galactic longitude and a few degrees in galactic latitude in $|l| < 45°$ and $|b| < 1°\!.5$. The GRXE has an integrated X-ray luminosity of $\sim$1 $\times 10^{38}$ erg s^{-1} in the 2–10 keV range (Koyama et al. [1986](#); Valinia & Marshall [1998](#)) at the distance of the Galactic Center. The X-ray spectrum is described by a two-temperature thermal plasma ($\sim$1 and 5–10 keV) with K-shell emission lines (e.g., Koyama et al. [1996](#); Yamauchi et al. [2009](#)): from neutral or low-ionized Fe at 6.4 keV (Fe I) as well as from highly ionized Fe at 6.7 keV (Fe XXV) and 7.0 keV (Fe XXVI).

It has been a subject of intense debate whether the GRXE is a truly diffuse emission of a low surface brightness along the Galactic plane or a composition of discrete faint unresolved X-ray sources such as cataclysmic variables (CVs) and X-ray active stars (e.g., Revnivtsev et al. [2006](#); Yuasa et al. [2012](#); Hong [2012](#)). Many X-ray observations have been carried out on this topic. In a Galactic bulge region ($l = 0°\!.08, b = -1°\!.42$), $\sim$80% of the diffuse X-ray emission was resolved into faint X-ray point sources using the deepest X-ray observation with the Chandra X-ray Observatory with an excellent spatial resolution of $0''\!.5$. This indicates that the apparently diffuse emission in the Galactic bulge is primarily made of faint discrete X-ray sources (Revnivtsev et al. [2009](#)). There are several candidates for such a population of faint X-ray sources, including magnetic CVs (e.g., Yuasa et al. [2012](#); Hong [2012](#)), nonmagnetic CVs (Nobukawa et al. [2016](#)), and X-ray active stars (e.g., Revnivtsev et al. [2006](#)).

However, it is difficult to constrain the nature of these faint X-ray point sources from X-ray observations alone, because most of these sources are detected only with a limited number of X-ray photons (fewer than 10 photons) even with the deepest observations. Thus, follow-up observations at longer wavelengths are needed. Because of the large interstellar absorption toward the Galactic plane, NIR observations are more suited than optical observations. NIR identifications of X-ray point sources were performed along the Galactic plane (e.g., Laycock et al. [2005](#); Morihana et al. [2016](#)), which provided clues to the nature of faint X-ray point source populations that make up the GRXE. The distance of these sources is unknown. Thus, classification of the sources is based on the X-ray to NIR flux ratio; high values suggest sources containing a compact object such as CVs and low values suggest sources otherwise such as stars. If the distance is obtained for many of these sources with JASMINE, we can discuss their nature based on the absolute luminosity both in X-ray and NIR bands and discriminate foreground contamination in the line of sight. A more robust classification of X-ray sources and their 3D distribution allow us to constrain the Galactic X-ray point source population for the different locations and components of our Galaxy, providing a hint to understanding the formation history of our Galaxy.

A large fraction of the observing fields of the GCS using JASMINE ($-0°\!.6 < b < 0°\!.6$ and $-1°\!.4 < l < 0°\!.7$ or $-0°\!.7 < l < 1°\!.4$ in section [2](#)) was observed with Chandra (the Chandra Multiwavelength Plane Survey; $-0°\!.4 < b < 0°\!.4$ and $-1.0° < l < 1.0°$, Grindlay et al. [2005](#)). A total of 9017 X-ray point sources were detected with a total exposure of 2.5 Ms (Muno et al. [2009](#)). NIR identifications for these X-ray point sources were also made (Mauerhan et al. [2009](#)). Based on this, we estimate that $\sim$600 X-ray sources will be identified in NIR brighter than 12.5 mag in the $H_{\rm w}$ band in the JASMINE GCS region. This is a significant improvement compared to the Gaia DR3 optical identification and astrometric distances for $\sim$100 sources (Gaia Collaboration [2023](#)), which are mostly foreground sources located within 2 kpc. This will be complemented with JASMINE.

5.3.9 Observations of small solar system bodies

As solar system bodies are moving objects, they are good targets for astrometry and time-series photometry. Precise astrometry improves the orbital elements of small solar system bodies such as comets and asteroids. It provides a solid foundation in several fields. Risks of minor bodies that threaten the Earth (potentially hazardous asteroids) can be precisely assessed. Non-gravitational effects such as the Yarkovsky effect can be quantitatively measured. An asteroid family, asteroids derived from the same parent body, can be identified. Astrometry of interstellar objects such as 1I/'Oumuamua and 2I/Borisov is essential to understand their origins. The rotation periods and shapes of minor bodies are derived from time-series photometry, leading to their internal structure estimates (bulk density). A binary system can be identified if it shows an
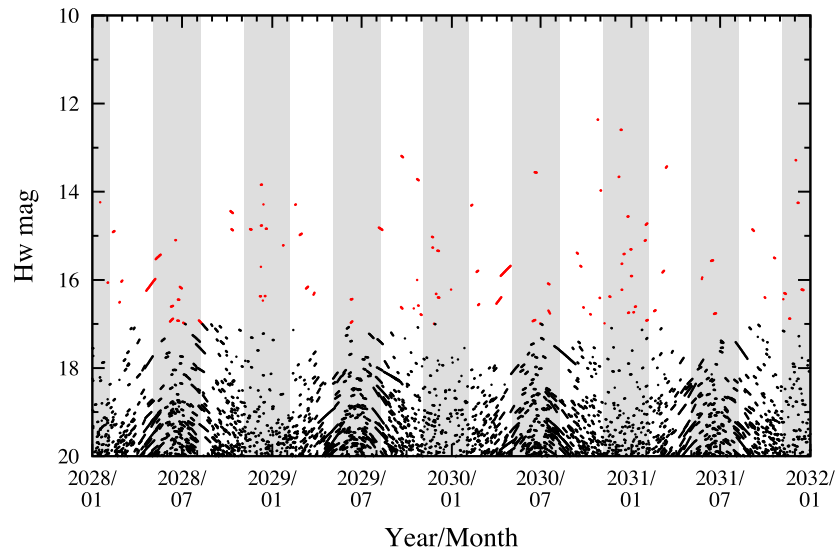
Fig. 21. Brightnesses of asteroids crossing the JASMINE GCS observation field, which is approximated with a 0.7 deg radius circle region from $(l, b) = (359°9, 0°0)$. Asteroids brighter than 17.0 mag are shown in red. The gray-shaded regions show the seasons when the Galactic Center is not accessible by JASMINE.

eclipse or mutual event. Time-series photometry is also useful for tracking the brightness changes of active asteroids. Since JASMINE is in a Sun-synchronous polar orbit, JASMINE's photometry will be complementary to ground-based observations. Finally, non-targeted, serendipitous surveys provide opportunities to discover new minor bodies.

The expected number of small solar system bodies via JASMINE is estimated as follows. Here, we focus on asteroids, the most abundant objects among minor bodies detectable by JASMINE. The spectral energy density of an asteroid is generally dominated by two components: reflected sunlight at optical wavelengths and thermal emission at infrared wavelengths. JASMINE's H_w band is located at transitional wavelengths between the two components. Hence, unfortunately, the minor bodies are fainter in the H_w band, and it is more challenging to detect them with JASMINE. To evaluate the observability of asteroids, we propagate the positions of known asteroids and check if they cross the JASMINE GCS observing region. The orbital elements of asteroids were retrieved from Lowell Minor Planet Services operated by Lowell Observatory on 2022 August 26. Objects with large uncertainties were removed. The total number of objects was 1192756, which includes 1148593 main-belt asteroids, 28829 near-Earth asteroids, 11458 Jupiter trojans, and 3876 trans-Neptunian objects. The topocentric (geocentric) coordinates were calculated from 2028 January 1 to 2031 December 31. For the sake of simplicity, JASMINE's observing region was defined as a circle with a radius of 0.7 degrees centered at $(l, b) = (359°9, 0°0)$ in galactic coordinates. The defined region differs from the current baseline of JASMINE GCS, but the number of observable objects is not significantly affected. With the distances, absolute magnitudes, and slope parameters, the apparent magnitudes of the bodies in the V band can be calculated (Bowell et al. [1989]). We then assume that the $V - H_w$ color for the objects is the same as the Sun, i.e., $(V - H_w)_\odot \sim 1.21$, and convert the V-band to H_w-band magnitude, assuming that all the asteroids have flat reflection spectra.

Figure 21 shows the brightnesses of asteroids crossing the JASMINE GCS region at different epochs. Each segment
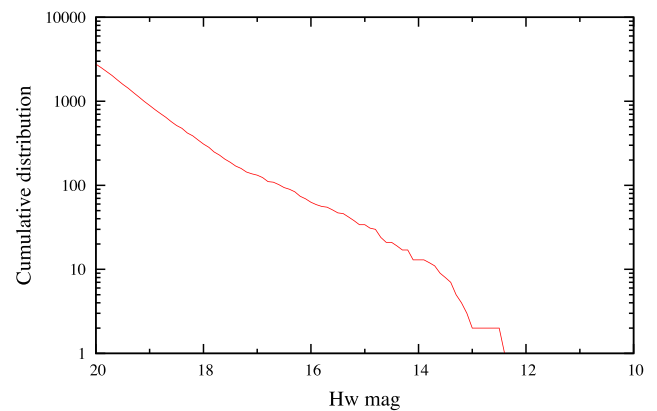
Fig. 22. Cumulative distribution of the H_w magnitude for asteroids observable throughout the JASMINE operation period.

shows an individual asteroid. Due to the operation constraint of the satellite, JASMINE does not observe the Galactic Center in the gray-shaded seasons. The length of the segment represents the observable duration, which depends on the relative motion to JASMINE. A handful of asteroids can be observed at apparent magnitudes brighter than $H_w = 14.5$ mag (sufficient for astrometry) and $H_w = 17.0$ mag (for photometry). Figure 22 illustrates a cumulative histogram of the H_w magnitude for observable asteroids. The numbers of objects brighter than $H_w = 14.5$ and 17.0 mag are about 10 and 100, respectively, throughout the operation period. The expected number of potential targets for astrometry in the JASMINE GCS is rather small. Thus, it is unlikely that there are serendipitous astrometric measurements with JASMINE, while targeted observations for known objects to provide additional astrometric information are preferred.

Taking advantage of accurate photometry, JASMINE may observe occultation events by minor bodies. Occultation provides valuable information for shape modeling and binary search. Since the brightness of a minor body does not matter in an occultation observation, the number of potential

targets significantly increases. Detecting an occultation event is feasible with accurate orbital elements and dedicated observation planning. Serendipitous observations of occultation events may detect new objects that are unreachable even by large telescopes with apertures of ∼10 m. Schlichting et al. (2009) claimed an occultation event by a trans-Neptunian object with a radius of 500 m at 45 au in archival data by the Hubble Space Telescope's Fine Guidance Sensors. Arimatsu et al. (2019) detected an occultation event by a trans-Neptunian object with a radius of 1.3 km using a coordinated observation system of multiple low-cost commercial off-the-shelf 0.28 m aperture telescopes, the Organized Autotelescopes for Serendipitous Event Survey (OASES, Arimatsu et al. 2017). Occultation events sometimes reveal additional features of satellites and rings. Rings around (2060) Chiron and (10199) Chariklo were identified by ground-based occultation observations (e.g., Braga-Ribas et al. 2014; Ortiz et al. 2015). Recently, a ring beyond the Roche limit was discovered around (50000) Quaoar (Morgado et al. 2023). High-precision photometry with JASMINE has the potential to detect minor features in light curves (Morgado et al. 2022). As for the serendipitous survey, careful assessment of false detection is required. OASES adopted simultaneous observations with multiple telescopes, to minimize the false detection rate. JASMINE may be able to detect occultation events after all anomalous signals are suppressed by careful calibration.

6 Synergies with other projects

In this section, we summarize the Galactic stellar survey projects complementary to JASMINE and planned to be operating in the late 2020s. Although there are many projects relevant to the JASMINE science cases, here, we only list the projects and/or new instruments more relevant to JASMINE's main survey targets of the GCS and the exoplanet survey, targeting M dwarfs.

6.1 Ground-based surveys

6.1.1 PRIME

The Prime Focus Infrared Microlensing Experiment (PRIME) is a wide field ($1.56\ \mathrm{deg}^2$) 1.8 m telescope at the South African Astronomical Observatory, which is operating since 2022. PRIME is jointly managed by Japan, the USA, and South Africa. PRIME has z-, Y-, J-, and H-band filters and several narrow-band filters. PRIME will observe the Galactic Center region around $-3° < l < 3°$ and $-2° < b < 2°$, which covers the whole area of the JASMINE GCS field. The prime target of PRIME is a microlensing exoplanet search. Joint observations with JASMINE can help to constrain the parameters of the exoplanet detection further with the additional accurate astrometry information of the source stars that JASMINE can provide. The time-series photometry of PRIME will also find many variable stars. As mentioned above, the PRIME data will be used to provide the catalog of Miras observable with JASMINE.

6.1.2 Vera C. Rubin Observatory/Legacy Survey of Space and Time (LSST)

The Vera C. Rubin Observatory is located on the Cerro Panchón ridge in Chile, and will run the 10 yr Legacy Survey of Space and Time (LSST) with the 8.4 m (6.5 m effective) Simonyi Survey Telescope (Ivezić et al. 2019). The Rubin Ob-

servatory LSST camera will have a 3.5 degree field of view with about 32 gigapixels with $0''\!.2$ sampling pixel size. There will be six filters (u, g, r, i, z, and y) covering 320–1050 nm. The survey is planed to begin in 2024, and the main survey will observe a 18000 deg^2 region of the sky about 800 times in the planed duration of 10 yr. The co-added map will reach $r \sim$ 27.5 mag, and it is anticipated to detect about 20 billion stars and a similar number of galaxies. The main science drivers of LSST are probing the properties of dark energy and dark matter, cataloging an inventory of the solar system, exploring the transient optical sky, and mapping the Milky Way. The survey field covers the Galactic bulge and the Galactic Center. The LSST is capable of providing astrometric measurements for fainter stars than is possible with Gaia. With the 10 yr baseline, the expected uncertainties of parallax and proper motions are respectively $\sigma_\pi = 0.6$ mas and $\sigma_\mu = 0.2$ mas yr^{-1} for stars brighter than $r = 21$ mag, and $\sigma_\pi = 2.9$ mas and $\sigma_\mu = 1.0$ mas yr^{-1} for stars brighter than $r = 24$ mag. In addition, the time-series photometry of the LSST will help to find many variable stars and microlensing events. The majority of them will be too faint for JASMINE to follow up. However, if they are bright enough and in the same field, JASMINE can provide more accurate astrometric information.

6.1.3 SDSS-V

The Sloan Digital Sky Survey (SDSS)-V (Kollmeier et al. 2017) is an ambitious project to run an all-sky multi-epoch spectroscopic survey, utilizing telescopes in both Northern and Southern hemispheres. The survey will provide optical and IR spectra covering a 2500 deg^2 ultra-wide field for more than 6 million objects in five years (2020–2025). SDSS-V uses the telescopes at Apache Point Observatory (APO) in USA and and Las Campanas Observatory (LCO) in Chile. At APO, the 2.5 m Sloan telescope will be continuously used for SDSS-V full-time. At LCO, more than 300 nights per year of telescope time of the 2.5 m du Pont telescope will be dedicated to this survey. The survey will also use the smaller (1 m to 16 cm) telescopes at APO and LCO. The NIR APOGEE spectrograph (300 fibers, $R = 22000$, $\lambda = 1.5$–1.7 μm), the eBOSS optical spectrograph (500 fibers, $R \sim 2000$, $\lambda = 0.36$–1.0 μm), and the MaNGA multi-object IFU ($R \sim 4000$, $\lambda = 0.36$–1.0 μm) will be used at both APO and LCO. SDSS-V will run three surveys, the Milky Way Mapper, the Black Hole Mapper, and the Local Volume Mapper. The most relevant survey to JASMINE is the Milky Way Mapper, which plans to observe 4–5 million stars in the Milky Way, with the NIR APOGEE spectrograph and/or the optical BOSS spectrograph. The Milky Way Mapper aims to understand the evolution of the Milky Way and the physics of the stars and the interstellar medium, as well as multiple stars and exoplanetary systems. The Galactic Genesis Survey, as part of the Milky Way Mapper, targets the stars with $H < 11$ mag and $G - H > 3.5$ mag, which are likely to overlap with the bright target stars of the JASMINE GCS fields, and will provide accurate radial velocity and abundance patterns.

6.1.4 Subaru/PFS

Subaru Prime Focus Spectrograph (PFS, Takada et al. 2014) is the next-generation instrument of the 8.2 m Subaru telescope at the summit of Maunakea, Hawai'i in the USA, operated by the National Astronomical Observatory of Japan. PFS is a joint instrument of the institutes in Japan, Taiwan, the USA, France, Brazil, Germany, and China. PFS has a

~ 1.38 deg^2 field of view, and about 2400 science fibers. PFS consists of blue ($\lambda = 0.38$–0.65 μm, $R \sim 2300$), red (low-resolution mode: $\lambda = 0.63$–0.97 μm, $R \sim 3000$; medium-resolution mode: $\lambda = 0.71$–0.885 μm, $R \sim 5000$), and NIR ($\lambda = 0.94$–1.26 μm, $R \sim 4300$) spectrographs. It is scheduled to start operating in 2024. About 300 nights over five years of Subaru time will be dedicated to the PFS survey for cosmology, galaxy evolution, and Galactic archaeology through the Subaru Strategic Survey Program (SSSP). The GCS field is not included in the PFS SSSP. However, the NIR spectrograph of PFS is especially well suited to spectroscopic follow-up for the JASMINE GCS field stars to obtain radial velocity and chemical abundances. We plan to apply for a Subaru Intensive Program (five nights per semester) to follow up the JASMINE target stars.

6.1.5 ULTIMATE-Subaru

ULTIMATE-Subaru (Minowa et al. 2020) is another next-generation NIR instrument of Subaru, which is planned to be installed around 2028. ULTIMATE-Subaru is a wide-field ($14' \times 14'$) NIR imager and multi-object spectrograph with ground-layer adaptive optics (GLAO), which enables a spatial resolution of FWHM $\sim 0.''2$ in the K band. There is a planned Galactic Center survey of a ~ 6 deg^2 region of the Galactic Center, which covers the whole JASMINE Galactic Center field, J, H, K, and the narrow-band K_{NB} filters with a high cadence of four days (one month) for the high (low) cadence field. JASMINE can provide the astrometric reference stars in NIR, which would improve the astrometric accuracy of ULTIMATE-Subaru Galactic Center survey data. The ULTIMATE-Subaru Galactic Center survey can observe numerous stars fainter than the JASMINE magnitude limit. The combined data of JASMINE and ULTIMATE-Subaru will provide accurate astrometric information on these faint stars. They would help to identify the star clusters in the Galactic Center region from the proper motion of stars, and increase the event rate of astrometric microlensing, which will enable the measurement of the masses of lensed objects with high precision, and help to identify BHs and exoplanets.

6.1.6 VLT/MOONS

The Multi-Object Optical and Near-infrared Spectrograph (MOONS, Cirasuolo et al. 2011) is a next-generation instrument of the Very Large Telescope (VLT) UT1 at the European Southern Observatory (ESO) on Cerro Paranal in the Atacama Desert of Chile, and the planned first light is in 2024. MOONS is a multi-object (about 1000 fibers) NIR spectrograph with a field of view of $25'$ diameter. There are three channels of spectrograph, covering the RI, YJ, and H bands, with both low- and high-resolution modes. The low-resolution mode covers a wavelength range of 0.65–1.8 μm with $R_{RI} > 4100$, $R_{YJ} > 4300$, and $R_H > 6600$. The high-resolution modes cover three disconnected wavelength ranges $\lambda_{RI} = 0.76$–0.89 μm, $\lambda_{YJ} = 0.93$–1.35 μm, and $\lambda_H = 1.52$–1.64 μm with the spectral resolution of $R_{RI} > 9200$, $R_{YJ} > 4300$ (fixed with the low-resolution mode), and $R_H > 18300$, respectively. MOONS science targets cover Galactic archaeology, the growth of galaxies, and the first galaxies. Galactic archaeology studies by MOONS plan to take spectra for the several million stars observed by Gaia and the VISTA telescope, providing crucial complementary information on the accurate radial velocity and detailed chemical abundances. The NIR coverage of MOONS is capable of recording the spectra of stars in the heavily obscured Galactic Center region. Even with the high-resolution mode in the NIR H band, a signal-to-noise ratio of more than 60 can be obtained with one hour of exposure for objects brighter than $H = 15$ mag. MOONS is likely to be the most powerful instrument in the 2020s, capable of taking high-resolution spectra for all the target stars in the JASMINE GCS field.

6.1.7 VISTA/4MOST

ESO's 4-meter Multi-Object Spectroscopic Telescope (4MOST, de Jong et al. 2019) will be installed on the VISTA telescope in Chile in 2024. 4MOST has 2436 fibers and a field of view of about 4.2 deg^2. There are two low-resolution and one high-resolution spectrographs. The low-resolution spectrographs cover the wavelength range of $\lambda = 0.37$–0.95 μm with $R \sim 6500$, while the high-resolution spectrograph covers three wavelength passbands of $\lambda = 0.3926$–0.4355, 0.5160–0.5730, and 0.6100–0.6760 μm. The 4MOST consortium will run 10 surveys using 70% of the available time in five years, and planned to start in 2024, taking more than 20 million low-resolution spectra and more than 3 million high-resolution spectra. The 4MOST Milky Way Disc And BuLgE Low (4MIDABLE-LR, Chiappini et al. 2019) and High-Resolution (4MIDABLE-HR, Bensby et al. 2019) surveys will take the spectra of about 15 million and 2 million stars in the Milky Way, respectively. Their targets include the inner disk and bar/bulge region. Their survey focuses on the stars for which Gaia provides precise astrometry, but are too faint for Gaia's radial velocity spectrograph to provide a radial velocity. Their optical survey will not cover many stars in the JASMINE GCS region. However, the combination of 4MIDABLE data and Gaia data will be a powerful resource to unveil the global nature of the bar and spiral arms, and is therefore highly complementary to the JASMINE GCS.

6.1.8 Subaru/IRD

The InfraRed Doppler (IRD) spectrograph ($R \approx 70000$, $\lambda = 0.950$–1.73 μm) on the Subaru telescope (Kotani et al. 2018) is one of the most powerful instruments in the world to follow up exoplanets around M dwarfs and young stars. Besides the "validation" of transiting planet candidates around mid M dwarfs identified by JASMINE, high-dispersion spectroscopy by IRD can play a key role in further characterization of those planets; precision radial velocity measurements by IRD would enable us to constrain precise planet masses as well as orbital eccentricities. Moreover, NIR transit spectroscopy by IRD would also allow us to constrain the stellar obliquity (spin–orbit angle) and atmospheric composition (e.g., He I and molecular species), which are supposed to reflect the dynamical and chemical evolution of exoplanetary systems (e.g., Hirano et al. 2020a). Since activity-induced radial velocity variations of host stars are suppressed in the NIR, IRD is also an ideal tool to confirm and characterize planets around young active stars.

6.2 Space missions

6.2.1 Gaia

ESA's Gaia (Gaia Collaboration 2016) was launched in 2013 December. The nominal mission lifetime was five years but the mission has been extended to the second quarter of 2025. The Gaia mission is an all-sky survey to provide precise astrometry for more than one billion stars brighter than

$G \sim 21$ mag. Gaia uses a broad passband, the G band, which covers a wavelength range of $\lambda \sim 0.33$–1.05 μm (Evans et al. 2018). In the final data release after the end of the mission, the astrometric accuracy for bright stars with $G \lesssim 13$ mag is expected to reach about 7 μas. An astrometric accuracy of about 149 μas is expected to be achieved for stars brighter than $G = 19$ mag.[6] Gaia has three instruments, an astrometric instrument (ASTRO), a spectrophotometer (BP/RP), and a radial velocity spectrograph (RVS). ASTRO provides the five astrometric parameters, stellar position, proper motion, and parallax. The spectrophotometer consists of BP and RP spectrophotometers. BP and RP respectively provide low-resolution ($R \sim 5$–25) spectra of the wavelength ranges of $\lambda \sim 0.33$–0.68 and ~ 0.64–1.05 μm, which are used for chromaticity calibration for astrometric measurement, and estimates of the stellar parameters and dust extinction. RVS is an integral-field spectrograph with $R \sim 11500$, covering $\lambda = 0.845$–0.872 μm (Cropper et al. 2018). The main aim of the RVS is to provide the radial velocity for about 150 million stars brighter than $G_{RVS} = 16$ mag, depending on the spectral type of stars, where G_{RVS} is the magnitude in the RVS passband. Gaia's fourth data release is expected to be in 2025, and the full catalog and all of the data will be released, including all epoch data for all sources based on 66 months of data of the nominal mission. The final fifth data release based on about 11 yr of the extended mission is expected to be in 2030. Hence, the late 2020s and early 2030s will be a truly golden age of Galactic archaeology. JASMINE is expected to be launched in this golden age, and will provide complementary data to the Gaia data, especially for the Galactic Center stars, which the optical astrometry mission, Gaia, cannot observe.

6.2.2 Nancy Grace Roman Space Telescope
The Nancy Grace Roman Space Telescope (Roman Space Telescope) is a NASA observatory to study dark energy, exoplanets, and infrared astrophysics (Spergel et al. 2015). The telescope has a primary mirror of 2.4 m diameter. The nominal mission lifetime is six years. The Roman Space Telescope has a wide field instrument (WFI) and a coronagraph instrument (CGI). WFI is a large area, 300 megapixel, NIR camera for imaging and slitless spectroscopy with a grism ($R = 435$–865) and prism ($R = 70$–170). The imaging mode utilizes several filters covering a wavelength range of $\lambda = 0.48$–2.0 μm. The most relevant survey of the Roman Space Telescope to JASMINE's GCS is their microlensing survey, which will repeatedly observe about 2.81 deg^2 (with 10 fields) around $-0°.5 < l < 1°.8$ and $-2°.2 < b < -1°$. There will be six 72 d campaigns over six years with a cadence of every 15 min with a wide filter and 12 h with a blue filter. The Roman Space Telescope will detect billions of bulge stars and the study to obtain the precise astrometry is ongoing (WFIRST Astrometry Working Group 2019). The current planned survey region of the microlensing survey of the Roman Space Telescope does not cover the Galactic Center that JASMINE's GCS targets, because the microlensing survey requires it to maximize the event rate of microlensing and therefore target the region of lower dust extinction to obtain a higher number density of background stars. However, the Roman Space Telescope is currently gathering community input for survey strategies to maximize the science output. With strong community inputs, there could be a possibility for the Roman Space Tele-

scope to observe the JASMINE GCS field. Then, the JASMINE astrometry results would be valuable to calibrate their astrometry for fainter stars observed by the Roman Space Telescope.

6.2.3 James Webb Space Telescope
The James Webb Space Telescope (JWST) is NASA's flagship space observatory (6.5 m aperture), launched at the end of 2021 (Gardner et al. 2006). JWST has two spectrographs in the NIR band, the NIR spectrograph (NIRSpec) and the NIR imager and slitless spectrograph (NIRISS). NIRSpec is a medium-resolution spectrograph ($R = 100$–2700) with a wavelength coverage of 0.6–5 μm. The saturation limit is $H \sim 10$ mag. NIRISS is a slitless spectrograph whose spectral resolution is about $R = 700$. The saturation limit is $J \sim 8.5$ mag. The mission lifetime of JWST is five years as designed, but 10 years as an optimistic goal. If the lifetime of JWST overlaps the observation period of JASMINE, these instruments will be the most powerful instruments to follow up exoplanets found by JASMINE's exoplanet survey, to characterize exoplanet atmospheres with detailed and precise transmission spectroscopy.

JWST could also have a superb capability to study the structure, populations, and dynamics of the stars in the Galactic Center. There is a large community proposal to observe a Galactic Center field of about $1°.25 \times 0°.25$ area around Sgr A* with multiple bands of NIRCam at multiple epochs (Schödel et al. 2023). This could provide proper motions for about 10 million faint stars in the Galactic Center with an expected accuracy of ~ 0.3 mas yr^{-1}, if the 5 yr time baseline is achieved. The JASMINE GCS covers a larger area than the JWST proposal field. JASMINE will provide complementary astrometry data for the brighter stars that are saturated in the JWST observation.

6.2.4 CHEOPS
The CHaratarising ExOPlanet Satellite (CHEOPS), launched in 2019 December, is an ESA space mission dedicated to precision photometry to determine the radius of transiting exoplanets (Broeg et al. 2014). The mission lifetime is assumed to be 3.5 yr (nominal). CHEOPS is a PIT type of transiting exoplanet exploration, similar to JASMINE. The telescope diameter (32 cm) is similar to that of JASMINE. The passband of CHEOPS is visible (see figure 11) while that of JASMINE is NIR. In this sense, JASMINE is complementary to CHEOPS. However, considering the difference in the launch dates, JASMINE should be regarded as a successor of CHEOPS in terms of a space facility for photometric follow-up of transiting planets found by ground-based surveys.

6.2.5 TESS
The Transiting Exoplanet Survey Satellite (TESS) is an MIT/NASA-led all-sky survey mission to find planets transiting bright nearby stars (Ricker et al. 2014). TESS has four cameras, each with 10.5 cm diameter and 24×24 deg^2 field of view (~ 2000 deg^2 in total), and each camera has four 2k $\times$ 2k CCDs with a pixel scale of 21″. The detectors are sensitive from 0.6–1.0 μm. During the 2 yr prime mission since the launch in 2018, TESS has monitored almost the entire sky in 26 overlapping segments, and has observed each segment for 27.4 d with a 2 min cadence for 15000 pre-selected stars and with a 30 min cadence for the full image. Extension of the mission has been approved and TESS will keep tiling the

---

whole sky until at least 2024. TESS has the capability of finding Earth-sized transiting planets near the habitable zone of early-to-mid M dwarfs, and such an example has indeed been reported (TOI-700 d and e, Gilbert et al. 2020, 2023). The larger telescope aperture and redder passband of JASMINE will make it sensitive to similar planets around later-type M dwarfs. Follow-up observations by JASMINE for planets detected by TESS may lead to finding longer-period/smaller planets that were missed by TESS, as well as to characterizing them even better through a finer sampling of the transit light curve.

6.2.6 PLATO

PLAnetary Transits and Oscillations of stars (PLATO) is the third M-class (M3) mission under development by ESA for a planned launch in 2026 (Rauer et al. 2014). The primary science goal is the detection and characterization of planets transiting bright solar-type stars, in particular terrestrial planets in the HZ. This will be achieved by high-precision, continuous photometric monitoring of a large number of bright stars using a collection of small and wide-field optical telescopes. According to the PLATO definition study report,[7] the payload is planned to consist of >20 cameras each with 12 cm diameter and covering a wavelength range of 0.5–1.0 μm, which result in a total field of view of $\sim$2000 deg^2. Although the specific observing strategy is yet to be determined, PLATO is likely to cover a significant fraction of the entire sky, as well as to monitor certain regions for a duration long enough ($\sim$2 yr; Nascimbeni et al. 2022) to find planets in the HZs of Sun-like stars. The duration of the nominal science operations is four years, which may well overlap with the operation period of JASMINE. The main targets of PLATO are bright ($V \lesssim$ 13 mag) Sun-like stars, while JASMINE targets late-type stars fainter in the optical passband, taking advantage of the NIR photometry. Therefore, the two missions are complementary to each other. Like TESS, PLATO observations might also provide transiting planet target candidates around M dwarfs that can be further characterized with NIR observations by JASMINE. PLATO also aims to characterize the properties, including precise age estimates at the 10% precision level, of the host stars from time-series photometry using asteroseismology. The age information for the large number of stars that PLATO will observe will be a precious resource for studies of Galactic archaeology (Miglio et al. 2017). Hence, it will also provide complementary data to the JASMINE GCS and mid-plane survey.

6.2.7 ARIEL

The Atmospheric Remote-sensing Infrared Exoplanet Large-survey (ARIEL, Tinetti et al. 2018) is the first space telescope dedicated to the study of exoplanet atmospheres, adopted as an ESA M4 mission, whose planned launch is in 2029. The effective size of the primary mirror of ARIEL will be $\sim$1 m, which is much smaller than JWST (6.5 m). However, ARIEL will be able to collect fluxes in the wavelength range of 0.5–7.8 μm at one time, using five dichroic mirrors, three NIR spectrometers, and three optical photometric detectors. This allows one to obtain an atmospheric spectrum with a very wide wavelength coverage from a single planetary transit or eclipse observation.

ARIEL will observe a thousand exoplanets with a wide range of mass and temperature, from hot Jupiters to warm/temperate Earths, in order to understand the statistical properties of exoplanetary atmospheres and planetary formation histories. While the current target list for ARIEL already includes a large number of Jovian planets, it still lacks Neptune- and smaller-sized planets that are suitable for atmospheric study, i.e., hosted by nearby M dwarfs (Edwards et al. 2019). Although TESS has been increasing the number of such targets, it may not be enough due to its limited telescope aperture size (10 cm) and wavelength sensitivity (because of covering only the optical). Small transiting planets around nearby M dwarfs that will be discovered by JASMINE could thus be good targets for atmospheric characterization by ARIEL. Given that JASMINE is planned to be launched ahead of ARIEL, JASMINE can provide prime targets for ARIEL in a timely manner.

7 Summary and conclusions

We summarize that the unique capability of the JASMINE mission will fill the gap left by other planned and ongoing projects of Galactic stellar surveys for Galactic archaeology and habitable exoplanet searches in the late 2020s. JASMINE will be the first mission to provide 10 μas-level astrometry in the NIR band with time-series photometry. JASMINE will offer precise astrometric information where the dust extinction is too strong for the optical astrometry mission, Gaia, to detect any stars, such as the Galactic Center field and the Galactic mid-plane. The astrometric data of stars hidden behind the dust in the Galactic Center and Galactic mid-plane will shed light on the formation epoch of the Galactic bar, the nature of the spiral arms, and the mechanism underlying radial migration in the inner Galactic disk, which are likely to be remaining questions after Gaia. The combination of time-series photometry and precise astrometry will provide a vast opportunity for serendipitous discovery, including the possibilities of detecting IMBHs, astrometric microlensing of inner disk BHs, and studying the nature of star-forming regions and X-ray sources. JASMINE will also be the only space observatory in the late 2020s that can follow up exoplanet transits detected by ground-based telescopes to find planets in outer and habitable orbits around late-type stars, just as the Spitzer space observatory contributed to revolutionizing the field.

Finally, we note that JASMINE will be a crucial science demonstration mission for what a future NIR astrometry mission can offer. JASMINE will be a key mission to bridge the successful Gaia mission and its proposed successor mission, GaiaNIR (e.g., Hobbs et al. 2021), to be launched in the 2040s. GaiaNIR will provide all-sky global astrometry in the NIR band, including the Galactic disk, bar, and bulge regions. Unprecedentedly high proper motion for the stars also observed with Gaia will be obtained, taking advantage of around 20 years of baseline between the Gaia and GaiaNIR missions. Also, GaiaNIR will help to maintain and improve the absolute astrometric quality of the celestial reference frame, which otherwise degrades with time. JASMINE will be a pioneering mission to open up the future μas-level NIR astrometry, and will become an important milestone to demonstrate the power of NIR astrometry. About 20 years of time difference between JASMINE and GaiaNIR will provide superb proper motion measurements for the stars observed by JASMINE, including

---

[7] ⟨https://sci.esa.int/web/plato/-/59252-plato-definition-study-report-red-book⟩.

the NSD stars. With careful correction of systematic errors, the combination of JASMINE, GaiaNIR, and other complementary data will endeavor to measure the acceleration of the stars and map the gravitational field in the Galactic Center (e.g., Chakrabarti et al. 2020, 2022).

References

Abbott, B. P., et al. 2016, Phys. Rev. Lett., 116, 061102
Abbott, R., et al. 2020, ApJ, 900, L13
Abdurro'uf et al. 2022, ApJS, 259, 35
Abrams, N. S., & Takada, M. 2020, ApJ, 905, 121
Agol, E., et al. 2021, Planet. Sci. J., 2, 1
Aharon, D., & Perets, H. B. 2015, ApJ, 799, 185
Aharonian, F., et al. 2005, A&A, 442, 1
Alard, C. 2001, A&A, 379, L44
Alexander, T., & Natarajan, P. 2014, Science, 345, 1330
Amaro-Seoane, P., et al. 2017, arXiv:1702.00786
Anders, F., Cantat-Gaudin, T., Quadrino-Lodoso, I., Gieles, M., Jordi, C., Castro-Ginard, A., & Balaguer-Núñez, L. 2021, A&A, 645, L2
Anderson, J., & King, I. R. 2000, PASP, 112, 1360
Antoja, T., et al. 2015, MNRAS, 453, 541
Antoja, T., et al. 2018, Nature, 561, 360
Antoja, T., Ramos, P., López-Guitart, F., Anders, F., Bernet, M., & Laporte, C. F. P. 2022, A&A, 668, A61
Antonini, F., Capuzzo-Dolcetta, R., Mastrobuono-Battisti, A., & Merritt, D. 2012, ApJ, 750, 111
Apai, D., Nardiello, D., & Bedin, L. R. 2021, ApJ, 906, 64
Apai, D., Radigan, J., Buenzli, E., Burrows, A., Reid, I. N., & Jayawardhana, R. 2013, ApJ, 768, 121
Arentsen, A., et al. 2020, MNRAS, 491, L11
Arimatsu, K., et al. 2017, PASJ, 69, 68
Arimatsu, K., et al. 2019, Nat. Astron., 3, 301
Artigau, É. 2018, in Handbook of Exoplanets, ed. H. J. Deeg & J. A. Belmonte (Cham: Springer), 94
Asano, T., Fujii, M. S., Baba, J., Bédorf, J., Sellentin, E., & Portegies Zwart, S. 2020, MNRAS, 499, 2416
Athanassoula, E. 1992, MNRAS, 259, 345
Athanassoula, E. 2005, MNRAS, 358, 1477
Athanassoula, E. 2012, MNRAS, 426, L46
Athanassoula, E. 2016, in Galactic Bulges, ed. E. Laurikainen et al. (Cham: Springer), 391
Athanassoula, E., & Misiriotis, A. 2002, MNRAS, 330, 35
Baba, J., & Kawata, D. 2020, MNRAS, 492, 4500
Baba, J., Kawata, D., Matsunaga, N., Grand, R. J. J., & Hunt, J. A. S. 2018, ApJ, 853, L23
Baba, J., Kawata, D., & Schönrich, R. 2022, MNRAS, 513, 2850
Baba, J., Saitoh, T. R., & Wada, K. 2013, ApJ, 763, 46
Balcells, M., Graham, A. W., Domínguez-Palmero, L., & Peletier, R. F. 2003, ApJ, 582, L79
Balcells, M., Graham, A. W., & Peletier, R. F. 2007, ApJ, 665, 1084
Baldassare, V. F., Dickey, C., Geha, M., & Reines, A. E. 2020, ApJ, 898, L3
Baldassare, V. F., Reines, A. E., Gallo, E., & Greene, J. E. 2015, ApJ, 809, L14
Bañados, E., et al. 2018, Nature, 553, 473
Bar, N., Blas, D., Blum, K., & Sibiryakov, S. 2018, Phys. Rev. D, 98, 083027
Barnes, S. A. 2003, ApJ, 586, 464
Bartko, H., et al. 2009, ApJ, 697, 1741
Beichman, C., et al. 2019, Res. Notes AAS, 3, 89

Bekki, K. 2000, ApJ, 545, 753

Bekki, K., & Tsujimoto, T. 2011, MNRAS, 416, L60

Belokurov, V., et al. 2006, ApJ, 642, L137

Belokurov, V., Erkal, D., Evans, N. W., Koposov, S. E., & Deason, A. J. 2018, MNRAS, 478, 611

Belokurov, V., & Kravtsov, A. 2022, MNRAS, 514, 689

Belokurov, V., Sanders, J. L., Fattahi, A., Smith, M. C., Deason, A. J., Evans, N. W., & Grand, R. J. J. 2020, MNRAS, 494, 3880

Belokurov, V. A., & Evans, N. W. 2002, MNRAS, 331, 649

Benjamin, R. A., et al. 2005, ApJ, 630, L149

Bensby, T., et al. 2019, Messenger, 175, 35

Benson, A. J., Bower, R. G., Frenk, C. S., Lacey, C. G., Baugh, C. M., & Cole, S. 2003, ApJ, 599, 38

Biller, B. 2017, Astron. Rev., 13, 1

Binney, J., Gerhard, O., & Spergel, D. 1997, MNRAS, 288, 365

Binney, J., & Schönrich, R. 2018, MNRAS, 481, 1501

Bland-Hawthorn, J., et al. 2019a, ApJ, 886, 45

Bland-Hawthorn, J., et al. 2019b, MNRAS, 486, 1167

Bland-Hawthorn, J., & Cohen, M. 2003, ApJ, 582, 246

Bland-Hawthorn, J., & Gerhard, O. 2016, ARA&A, 54, 529

Bland-Hawthorn, J., Maloney, P. R., Sutherland, R. S., & Madsen, G. J. 2013, ApJ, 778, 58

Bland-Hawthorn, J., & Tepper-García, T. 2021, MNRAS, 504, 3168

Blum, R. D., Ramírez, S. V., Sellgren, K., & Olsen, K. 2003, ApJ, 597, 323

Book, L. G., & Flanagan, É. É. 2011, Phys. Rev. D, 83, 024024

Bouvier, J., Matt, S. P., Mohanty, S., Scholz, A., Stassun, K. G., & Zanni, C. 2014, in Protostars and Planets VI, ed. H. Beuther et al. (Tucson: University of Arizona Press), 433

Bovy, J., Leung, H. W., Hunt, J. A. S., Mackereth, J. T., García-Hernández, D. A., & Roman-Lopes, A. 2019, MNRAS, 490, 4740

Bowell, E., Hapke, B., Domingue, D., Lumme, K., Peltoniemi, J., & Harris, A. W. 1989, in Asteroids II, ed. R. P. Binzel et al. (Tucson: University of Arizona Press), 524

Brady, M. T., & Bean, J. L. 2022, AJ, 163, 255

Braga-Ribas, F., et al. 2014, Nature, 508, 72

Broeg, C., Benz, W., & Thomas, N. Cheops Team 2014, Contr. Astron. Obser. Skalnate Pleso, 43, 498

Bromm, V., & Loeb, A. 2003, ApJ, 596, 34

Brown, G. E., & Bethe, H. A. 1994, ApJ, 423, 659

Brown, W. R. 2015, ARA&A, 53, 15

Brown, W. R., Geller, M. J., Kenyon, S. J., & Kurtz, M. J. 2005, ApJ, 622, L33

Buenzli, E., Apai, D., Radigan, J., Reid, I. N., & Flateau, D. 2014, ApJ, 782, 77

Cantat-Gaudin, T., et al. 2018, A&A, 618, A93

Carpenter, J. M. 2000, AJ, 120, 3139

Castro-Ginard, A., et al. 2020, A&A, 635, A45

Catchpole, R. M., Whitelock, P. A., Feast, M. W., Hughes, S. M. G., Irwin, M., & Alard, C. 2016, MNRAS, 455, 2216

Cavanagh, M. K., Bekki, K., Groves, B. A., & Pfeffer, J. 2022, MNRAS, 510, 5164

Chakrabarti, S., et al. 2020, ApJ, 902, L28

Chakrabarti, S., et al. 2023, AJ, 166, 6

Chakrabarti, S., Stevens, D. J., Wright, J., Rafikov, R. R., Chang, P., Beatty, T., & Huber, D. 2022, ApJ, 928, L17

Chaplin, W. J., & Miglio, A. 2013, ARA&A, 51, 353

Chatzopoulos, S., Fritz, T. K., Gerhard, O., Gillessen, S., Wegg, C., Genzel, R., & Pfuhl, O. 2015, MNRAS, 447, 948

Chiappini, C., et al. 2019, Messenger, 175, 30

Chiba, R., Friske, J. K. S., & Schönrich, R. 2021, MNRAS, 500, 4710

Chiba, R., & Schönrich, R. 2021, MNRAS, 505, 2412

Chilingarian, I. V., Katkov, I. Y., Zolotukhin, I. Y., Grishin, K. A., Beletsky, Y., Boutsia, K., & Osip, D. J. 2018, ApJ, 863, 1

Ciambur, B. C., Graham, A. W., & Bland-Hawthorn, J. 2017, MNRAS, 471, 3988

Cirasuolo, M., Afonso, J., Bender, R., Bonifacio, P., Evans, C., Kaper, L., Oliva, E., & Vanzi, L. 2011, Messenger, 145, 11

Ciucă, I., Kawata, D., Ando, S., Calore, F., Read, J. I., & Mateu, C. 2018, MNRAS, 480, 2284

Ciucă, I., Kawata, D., Miglio, A., Davies, G. R., & Grand, R. J. J. 2021, MNRAS, 503, 2814

Clarke, J. P., & Gerhard, O. 2022, MNRAS, 512, 2171

Clarkson, W., et al. 2008, ApJ, 684, 1110

Clarkson, W. I., Ghez, A. M., Morris, M. R., Lu, J. R., Stolte, A., McCrady, N., Do, T., & Yelda, S. 2012, ApJ, 751, 132

Clavel, M., Terrier, R., Goldwurm, A., Morris, M. R., Ponti, G., Soldi, S., & Trap, G. 2013, A&A, 558, A32

Cole, A. A., & Weinberg, M. D. 2002, ApJ, 574, L43

Cole, D. R., Debattista, V. P., Erwin, P., Earp, S. W. F., & Roškar, R. 2014, MNRAS, 445, 3352

Colombo, D., et al. 2022, A&A, 658, A54

Combes, F., Debbasch, F., Friedli, D., & Pfenniger, D. 1990, A&A, 233, 82

Crocker, R. M., & Aharonian, F. 2011, Phys. Rev. Lett., 106, 101102

Crockett, C. J., Mahmud, N. I., Prato, L., Johns-Krull, C. M., Jaffe, D. T., Hartigan, P. M., & Beichman, C. A. 2012, ApJ, 761, 164

Cropper, M., et al. 2018, A&A, 616, A5

Crossfield, I. J. M. 2013, A&A, 551, A99

Crossfield, I. J. M. 2014, A&A, 566, A130

Curtis, J. L., et al. 2020, ApJ, 904, 140

Das, P., Hawkins, K., & Jofré, P. 2020, MNRAS, 493, 5195

Das, P., & Sanders, J. L. 2019, MNRAS, 484, 294

David, T. J., Petigura, E. A., Luger, R., Foreman-Mackey, D., Livingston, J. H., Mamajek, E. E., & Hillenbrand, L. A. 2019, ApJ, 885, L12

Davies, M. B., Benz, W., & Hills, J. G. 1991, ApJ, 381, 449

Davis, B. L., & Graham, A. W. 2021, Publ. Astron. Soc. Australia, 38, e030

de Jong, R. S., et al. 2019, Messenger, 175, 3

De Martino, I., Broadhurst, T., Henry Tye, S. H., Chiueh, T., & Schive, H.-Y. 2020, Phys. Dark Universe, 28, 100503

De Simone, R., Wu, X., & Tremaine, S. 2004, MNRAS, 350, 627

Debattista, V. P., Earp, S. W. F., Ness, M., & Gonzalez, O. A. 2018, MNRAS, 473, 5275

Debattista, V. P., Ness, M., Earp, S. W. F., & Cole, D. R. 2015, ApJ, 812, L16

Dehnen, W. 1999, ApJ, 524, L35

Dehnen, W. 2000, AJ, 119, 800

Dékány, I., et al. 2015, ApJ, 812, L29

Delrez, L., et al. 2018, in Proc. SPIE, 10700, Ground-based and Airborne Telescopes VII, ed. H. K. Marshall & J. Spyromilio (Bellingham, WA: SPIE), 107001I

Deming, D., & Knutson, H. A. 2020, Nature Astron., 4, 453

Demorest, P. B., Pennucci, T., Ransom, S. M., Roberts, M. S. E., & Hessels, J. W. T. 2010, Nature, 467, 1081

Di Matteo, P., Haywood, M., Combes, F., Semelin, B., & Snaith, O. N. 2013, A&A, 553, A102

Di Matteo, P., Haywood, M., Lehnert, M. D., Katz, D., Khoperskov, S., Snaith, O. N., Gómez, A., & Robichon, N. 2019, A&A, 632, A4

Do, T., et al. 2019, ApJ, 882, L27

Dobbs, C., & Baba, J. 2014, Publ. Astron. Soc. Australia, 31, e035

Dominik, M., & Sahu, K. C. 2000, ApJ, 534, 213

D'Onghia, E., Springel, V., Hernquist, L., & Keres, D. 2010, ApJ, 709, 1138

Dressing, C. D., & Charbonneau, D. 2013, ApJ, 767, 95

Dressing, C. D., & Charbonneau, D. 2015, ApJ, 807, 45

Dupuy, T. J., Brandt, G. M., & Brandt, T. D. 2022, MNRAS, 509, 4411

Dupuy, T. J., Brandt, T. D., Kratter, K. M., & Bowler, B. P. 2019, ApJ, 871, L4

El-Badry, K., et al. 2023a, MNRAS, 518, 1057

El-Badry, K., et al. 2023b, MNRAS, 521, 4323

Erwin, P. 2004, A&A, 415, 941

Evans, D. W., et al. 2018, A&A, 616, A4

Fabrycky, D. C., et al. 2014, ApJ, 790, 146

Farrell, S. A., Webb, N. A., Barret, D., Godet, O., & Rodrigues, J. M. 2009, Nature, 460, 73

Feast, M., & Whitelock, P. 1997, MNRAS, 291, 683

Feldmeier, A., et al. 2014, A&A, 570, A2

Feldmeier-Krause, A., et al. 2020, MNRAS, 494, 396

Feldmeier-Krause, A., Zhu, L., Neumayer, N., van de Ven, G., de Zeeuw, P. T., & Schödel, R. 2017, MNRAS, 466, 4040

Feltzing, S., Bowers, J. B., & Agertz, O. 2020, MNRAS, 493, 1419

Feng, F., Anglada-Escudé, G., Tuomi, M., Jones, H. R. A., Chanamé, J., Butler, P. R., & Janson, M. 2019, MNRAS, 490, 5002

Fernández-Trincado, J. G., et al. 2022, A&A, 663, A126

Ferrara, A., Salvadori, S., Yue, B., & Schleicher, D. 2014, MNRAS, 443, 2410

Ferrarese, L., & Merritt, D. 2000, ApJ, 539, L9

Ferreira, E. G. M. 2021, A&AR, 29, 7

Figer, D. F., et al. 2002, ApJ, 581, 258

Figer, D. F., McLean, I. S., & Morris, M. 1999, ApJ, 514, 202

Filippenko, A. V., & Ho, L. C. 2003, ApJ, 588, L13

Fisher, D. B., & Drory, N. 2010, ApJ, 716, 942

Fox, A. J., et al. 2015, ApJ, 799, L7

Fragkoudi, F., et al. 2019, MNRAS, 488, 3324

Fragkoudi, F., et al. 2020, MNRAS, 494, 5936

Frankel, N., Rix, H.-W., Ting, Y.-S., Ness, M., & Hogg, D. W. 2018, ApJ, 865, 96

Frankel, N., Sanders, J., Ting, Y.-S., & Rix, H.-W. 2020, ApJ, 896, 15

Freeman, K., et al. 2013, MNRAS, 428, 3660

Freeman, K., & Bland-Hawthorn, J. 2002, ARA&A, 40, 487

Friedli, D., & Benz, W. 1993, A&A, 268, 65

Friedli, D., & Martinet, L. 1993, A&A, 277, 27

Friske, J. K. S., & Schönrich, R. 2019, MNRAS, 490, 5414

Fritz, T. K., et al. 2011, ApJ, 737, 73

Fritz, T. K., et al. 2016, ApJ, 821, 44

Fritz, T. K., et al. 2021, A&A, 649, A83

Fujii, M., Iwasawa, M., Funato, Y., & Makino, J. 2008, ApJ, 686, 1082

Fujii, M. S., Bédorf, J., Baba, J., & Portegies Zwart, S. 2019, MNRAS, 482, 1983

Fukui, A., et al. 2019, AJ, 158, 206

Fulton, B. J., et al. 2017, AJ, 154, 109

Gadotti, D. A., et al. 2019, MNRAS, 482, 506

Gadotti, D. A., Seidel, M. K., Sánchez-Blázquez, P., Falcón-Barroso, J., Husemann, B., Coelho, P., & Pérez, I. 2015, A&A, 584, A90

Gaia Collaboration 2016, A&A, 595, A1

Gaia Collaboration 2018a, A&A, 616, A1

Gaia Collaboration 2018b, A&A, 616, A11

Gaia Collaboration 2021, A&A, 649, A1

Gaia Collaboration 2023, A&A, 674, A1

Gallart, C., Bernard, E. J., Brook, C. B., Ruiz-Lara, T., Cassisi, S., Hill, V., & Monelli, M. 2019, Nat. Astron., 3, 932

Gallego-Cano, E., Schödel, R., Nogueras-Lara, F., Dong, H., Shahzamanian, B., Fritz, T. K., Gallego-Calvente, A. T., & Neumayer, N. 2020, A&A, 634, A71

García Pérez, A. E., et al. 2018, ApJ, 852, 91

Gardner, J. P., et al. 2006, Space Sci. Rev., 123, 485

Gaudi, B. S., et al. 2020, arXiv:2001.06683

Gebhardt, K., et al. 2000, ApJ, 539, L13

Genzel, R., Thatte, N., Krabbe, A., Kroker, H., & Tacconi-Garman, L. E. 1996, ApJ, 472, 153

Gerhard, O., & Martinez-Valpuesta, I. 2012, ApJ, 744, L8

Gilbert, E. A., et al. 2020, AJ, 160, 116

Gilbert, E. A., et al. 2023, ApJ, 944, L35

Gillon, M., et al. 2016, Nature, 533, 221

Gillon, M., et al. 2017, Nature, 542, 456

Gilmore, G., et al. 2012, Messenger, 147, 25

Gonzalez, O. A., Rejkuba, M., Minniti, D., Zoccali, M., Valenti, E., & Saito, R. K. 2011, A&A, 534, L14

Gonzalez, O. A., Rejkuba, M., Zoccali, M., Valent, E., Minniti, D., & Tobar, R. 2013, A&A, 552, A110

Gouda, N. 2011, Scholarpedia, 6, 12021

Grady, J., Belokurov, V., & Evans, N. W. 2019, MNRAS, 483, 3022

Grady, J., Belokurov, V., & Evans, N. W. 2020, MNRAS, 492, 3128

Graham, A. W. 2016a, in Galactic Bulges, ed. E. Laurikainen et al. (Cham: Springer), 263

Graham, A. W. 2016b, in IAU Symp. 312, Star Clusters and Black Holes in Galaxies across Cosmic Time, ed. Y. Meiron et al. (Cambridge: Cambridge University Press), 269

Graham, A. W. 2020, MNRAS, 492, 3263

Graham, A. W. 2023a, MNRAS, 518, 6293

Graham, A. W. 2023b, MNRAS, 521, 1023

Graham, A. W., Ciambur, B. C., & Soria, R. 2016, ApJ, 818, 172

Graham, A. W., Erwin, P., Caon, N., & Trujillo, I. 2001, ApJ, 563, L11

Graham, A. W., Erwin, P., Trujillo, I., & Asensio Ramos, A. 2003, AJ, 125, 2951

Graham, A. W., & Guzmán, R. 2003, AJ, 125, 2936

Graham, A. W., & Sahu, N. 2023a, MNRAS, 518, 2177

Graham, A. W., & Sahu, N. 2023b, MNRAS, 520, 1975

Graham, A. W., & Scott, N. 2015, ApJ, 798, 54

Graham, A. W., Soria, R., Ciambur, B. C., Davis, B. L., & Swartz, D. A. 2021a, ApJ, 923, 146

Graham, A. W., Soria, R., Davis, B. L., Kolehmainen, M., Maccarone, T., Miller-Jones, J., Motch, C., & Swartz, D. A. 2021b, ApJ, 923, 246

Graham, A. W., & Spitler, L. R. 2009, MNRAS, 397, 2148

Grand, R. J. J., Kawata, D., & Cropper, M. 2012, MNRAS, 421, 1529

Grand, R. J. J., Pakmor, R., Fragkoudi, F., Gómez, F. A., Trick, W., Simpson, C. M., van de Voort, F., & Bieri, R. 2023, MNRAS, 524, 801

GRAVITY Collaboration 2021, A&A, 647, A59

Greene, J. E., & Ho, L. C. 2004, ApJ, 610, 722

Greene, J. E., Strader, J., & Ho, L. C. 2020, ARA&A, 58, 257

Grimm, S. L., et al. 2018, A&A, 613, A68

Grindlay, J. E., et al. 2005, ApJ, 635, 920

Guo, F., & Mathews, W. G. 2012, ApJ, 756, 181

Habouzit, M., Volonteri, M., Latif, M., Dubois, Y., & Peirani, S. 2016, MNRAS, 463, 529

Halle, A., Di Matteo, P., Haywood, M., & Combes, F. 2015, A&A, 578, A58

Halle, A., Di Matteo, P., Haywood, M., & Combes, F. 2018, A&A, 616, A86

Haqq-Misra, J., Wolf, E. T., Joshi, M., Zhang, X., & Kopparapu, R. K. 2018, ApJ, 852, 67

Hayden, M. R., et al. 2015, ApJ, 808, 132

Haywood, M., Di Matteo, P., Lehnert, M., Snaith, O., Fragkoudi, F., & Khoperskov, S. 2018a, A&A, 618, A78

Haywood, M., Di Matteo, P., Lehnert, M. D., Snaith, O., Khoperskov, S., & Gómez, A. 2018b, ApJ, 863, 113

Helmi, A., Babusiaux, C., Koppelman, H. H., Massari, D., Veljanoski, J., & Brown, A. G. A. 2018, Nature, 563, 85

Henshaw, J. D., et al. 2016, MNRAS, 457, 2675

Hernquist, L. 1990, ApJ, 356, 359

Hills, J. G. 1988, Nature, 331, 687

Hirano, S., Hosokawa, T., Yoshida, N., Umeda, H., Omukai, K., Chiaki, G., & Yorke, H. W. 2014, ApJ, 781, 60

Hirano, T., et al. 2020a, ApJ, 890, L27

Hirano, T., et al. 2020b, ApJ, 899, L13

Hobbs, D., et al. 2021, Exp. Astron., 51, 783

Hong, J. 2012, MNRAS, 427, 1633

Horta, D., et al. 2021a, MNRAS, 500, 1385

Horta, D., et al. 2021b, MNRAS, 500, 5462

Horta, D., et al. 2023, MNRAS, 520, 5671

Hosek, M. W., Do, T., Lu, J. R., Morris, M. R., Ghez, A. M., Martinez, G. D., & Anderson, J. 2022, ApJ, 939, 68

Howard, C. D., Rich, R. M., Reitzel, D. B., Koch, A., De Propris, R., & Zhao, H. 2008, ApJ, 688, 1060

Hsu, D. C., Ford, E. B., & Terrien, R. 2020, MNRAS, 498, 2249

Huang, Y., et al. 2017, ApJ, 847, L9

Hunt, J. A. S., & Bovy, J. 2018, MNRAS, 477, 3945

Hunt, J. A. S., Bub, M. W., Bovy, J., Mackereth, J. T., Trick, W. H., & Kawata, D. 2019, MNRAS, 490, 1026

Hunt, J. A. S., Hong, J., Bovy, J., Kawata, D., & Grand, R. J. J. 2018, MNRAS, 481, 3794

Hunt, J. A. S., Price-Whelan, A. M., Johnston, K. V., & Darragh-Ford, E. 2022, MNRAS, 516, L7

Hunt, J. A. S., Stelea, I. A., Johnston, K. V., Gandhi, S. S., Laporte, C. F. P., & Bédorf, J. 2021, MNRAS, 508, 1459

Ida, S., & Lin, D. N. C. 2004, ApJ, 604, 388

Ida, S., & Lin, D. N. C. 2005, ApJ, 626, 1045

Imig, J., et al. 2023, ApJ, 954, 124

Inayoshi, K., Omukai, K., & Tasker, E. 2014, MNRAS, 445, L109

Irwin, J., Charbonneau, D., Nutzman, P., & Falco, E. 2009, in IAU Symp. 253, Transiting Planets, ed. F. Pont et al. (Cambridge: Cambridge University Press), 37

Ivezić, Ž., et al. 2019, ApJ, 873, 111

Izquierdo-Villalba, D., et al. 2022, MNRAS, 514, 1006

Javanmardi, B., et al. 2016, A&A, 588, A89

Jiang, N., et al. 2018, ApJ, 869, 49

Johnstone, C. P., Bartel, M., & Güdel, M. 2021, A&A, 649, A96

Kawahara, H., & Masuda, K. 2020, ApJ, 900, 48

Kawahara, H., Matsuo, T., Takami, M., Fujii, Y., Kotani, T., Murakami, N., Tamura, M., & Guyon, O. 2012, ApJ, 758, 13

Kawanaka, N., Yamaguchi, M., Piran, T., & Bulik, T. 2017, in IAU Symp. 324, New Frontiers in Black Hole Astrophysics, ed. A. Gomboc (Cambridge: Cambridge University Press), 41

Kawata, D., Baba, J., Ciucă, I., Cropper, M., Grand, R. J. J., Hunt, J. A. S., & Seabroke, G. 2018, MNRAS, 479, L108

Kawata, D., Hunt, J. A. S., Grand, R. J. J., Pasetto, S., & Cropper, M. 2014, MNRAS, 443, 2757

Khanna, S., et al. 2019, MNRAS, 489, 4962

Khoperskov, S., Di Matteo, P., Gerhard, O., Katz, D., Haywood, M., Combes, F., Berczik, P., & Gomez, A. 2019, A&A, 622, L6

Khoperskov, S., Di Matteo, P., Haywood, M., Gómez, A., & Snaith, O. N. 2020, A&A, 638, A144

Khoperskov, S., & Gerhard, O. 2022, A&A, 663, A38

Kikuchihara, S., et al. 2020, ApJ, 893, 60

Kim, S. Y., Peter, A. H. G., & Hargis, J. R. 2018, Phys. Rev. Lett., 121, 211302

King, A., & Pounds, K. 2015, ARA&A, 53, 115

Kisku, S., et al. 2021, MNRAS, 504, 1657

Klioner, S. A. 2018, Classical Quantum Gravity, 35, 045005

Kobayashi, Y., Okuda, H., Sato, S., Jugaku, J., & Dyck, H. M. 1983, PASJ, 35, 101

Kollmeier, J. A., et al. 2017, arXiv:1711.03234

Koposov, S. E., et al. 2020, MNRAS, 491, 2465

Kopparapu, R. K., Wolf, E. T., Arney, G., Batalha, N. E., Haqq-Misra, J., Grimm, S. L., & Heng, K. 2017, ApJ, 845, 5

Kormendy, J., Fisher, D. B., Cornell, M. E., & Bender, R. 2009, ApJS, 182, 216

Kormendy, J., & Ho, L. C. 2013, ARA&A, 51, 511

Kormendy, J., & Kennicutt, R. C., Jr. 2004, ARA&A, 42, 603

Kotani, T., et al. 2018, in Proc. SPIE, 10702, Ground-based and Airborne Instrumentation for Astronomy VII, ed. C. J. Evans et al. (Bellingham, WA: SPIE), 1070211

Koyama, K., Maeda, Y., Sonobe, T., Takeshima, T., Tanaka, Y., & Yamauchi, S. 1996, PASJ, 48, 249

Koyama, K., Makishima, K., Tanaka, Y., & Tsunemi, H. 1986, PASJ, 38, 121

Kunder, A., et al. 2012, AJ, 143, 57

Laine, S., Shlosman, I., Knapen, J. H., & Peletier, R. F. 2002, ApJ, 567, 97

Lam, C. Y., et al. 2022, ApJ, 933, L23

Langer, N., Baade, D., Bodensteiner, J., Greiner, J., Rivinius, T., Martayan, C., & Borre, C. C. 2020, A&A, 633, A40

Laporte, C. F. P., Minchev, I., Johnston, K. V., & Gómez, F. A. 2019, MNRAS, 485, 3134

Launhardt, R., Zylka, R., & Mezger, P. G. 2002, A&A, 384, 112

Laycock, S., Grindlay, J., van den Berg, M., Zhao, P., Hong, J., Koenig, X., Schlegel, E. M., & Persson, S. E. 2005, ApJ, 634, L53

Ledo, H. R., Sarzi, M., Dotti, M., Khochfar, S., & Morelli, L. 2010, MNRAS, 407, 969

Li, Z., Shen, J., Gerhard, O., & Clarke, J. P. 2022, ApJ, 925, 71

Li, Z., Shen, J., & Kim, W.-T. 2015, ApJ, 806, 150

Li, Z., Shen, J., & Schive, H.-Y. 2020, ApJ, 889, 88

Lin, C. C., & Shu, F. H. 1964, ApJ, 140, 646

Luger, R., Agol, E., Kruse, E., Barnes, R., Becker, A., Foreman-Mackey, D., & Deming, D. 2016, AJ, 152, 100

Lundkvist, M. S., et al. 2016, Nature Commun., 7, 11201

Lustig-Yaeger, J., Meadows, V. S., & Lincowski, A. P. 2019, AJ, 158, 27

Mackereth, J. T., et al. 2019, MNRAS, 489, 176

Maeder, A. 1992, A&A, 264, 105

Magorrian, J., et al. 1998, AJ, 115, 2285

Majewski, S. R., et al. 2017, AJ, 154, 94

Maleki, A., Baghram, S., & Rahvar, S. 2020, Phys. Rev. D, 101, 103504

Mann, A. W., et al. 2016, AJ, 152, 61

Mann, A. W., et al. 2017, AJ, 153, 64

Mann, A. W., et al. 2018, AJ, 155, 4

Mann, A. W., Feiden, G. A., Gaidos, E., Boyajian, T., & von Braun, K. 2015, ApJ, 804, 64

Mao, Y.-Y., Geha, M., Wechsler, R. H., Weiner, B., Tollerud, E. J., Nadler, E. O., & Kallivayalil, N. 2021, ApJ, 907, 85

Martel, H., Kawata, D., & Ellison, S. L. 2013, MNRAS, 431, 2560

Martell, S. L., et al. 2017, MNRAS, 465, 3203

Martig, M., et al. 2016, MNRAS, 456, 3655

Masseron, T., & Gilmore, G. 2015, MNRAS, 453, 1855

Massey, P., Levine, S. E., Neugent, K. F., Levesque, E., Morrell, N., & Skiff, B. 2018, AJ, 156, 265

Matsunaga, N., et al. 2011, Nature, 477, 188

Matsunaga, N., et al. 2015, ApJ, 799, 46

Matsunaga, N., Kawadu, T., Nishiyama, S., Nagayama, T., Hatano, H., Tamura, M., Glass, I. S., & Nagata, T. 2009, MNRAS, 399, 1709

Mauerhan, J. C., Muno, M. P., Morris, M. R., Bauer, F. E., Nishiyama, S., & Nagata, T. 2009, ApJ, 703, 30

McConnachie, A. W., & Venn, K. A. 2020, AJ, 160, 124

McWilliam, A., & Zoccali, M. 2010, ApJ, 724, 1491

Metchev, S. A., et al. 2015, ApJ, 799, 154

Middleton, H., Clearwater, P., Melatos, A., & Dunn, L. 2020, Phys. Rev. D, 102, 023006

Miglio, A., et al. 2017, Astron. Nachrichten, 338, 644

Miglio, A., et al. 2021a, A&A, 645, A85

Miglio, A., et al. 2021b, Exp. Astron., 51, 963

Miller, M. C. 2013, arXiv:1312.0029

Minchev, I., et al. 2018, MNRAS, 481, 1645

Minchev, I., & Famaey, B. 2010, ApJ, 722, 112

Minniti, D., et al. 2010, New Astron., 15, 433

Minowa, Y., et al. 2020, in Proc. SPIE, 11450, Modeling, Systems Engineering, and Project Management for Astronomy IX, ed. G. Z. Angeli & P. Dierickx (Bellingham, WA: SPIE), 114500O

Mirabel, I. F. 2012, Science, 335, 175

Miroshnichenko, A. S., Bjorkman, K. S., & Krugov, V. D. 2002, PASP, 114, 1226

Miyakawa, K., Hirano, T., Fukui, A., Mann, A. W., Gaidos, E., & Sato, B. 2021, AJ, 162, 104

Miyakawa, K., Hirano, T., Sato, B., & Okuzumi, S. 2022, AJ, 164, 209

Monari, G., Famaey, B., Siebert, A., Bienaymé, O., Ibata, R., Wegg, C., & Gerhard, O. 2019a, A&A, 632, A107

Monari, G., Famaey, B., Siebert, A., Wegg, C., & Gerhard, O. 2019b, A&A, 626, A41

Morales, J. C., et al. 2019, Science, 365, 1441

Morelli, L., Cesetti, M., Corsini, E. M., Pizzella, A., Dalla Bontà, E., Sarzi, M., & Bertola, F. 2010, A&A, 518, A32

Morgado, B. E., et al. 2022, A&A, 664, L15

Morgado, B. E., et al. 2023, Nature, 614, 239

Morihana, K., Tsujimoto, M., Dubath, P., Yoshida, T., Suzuki, K., & Ebisawa, K. 2016, PASJ, 68, 57

Morley, C. V., Fortney, J. J., Marley, M. S., Visscher, C., Saumon, D., & Leggett, S. K. 2012, ApJ, 756, 172

Motch, C., Lopes de Oliveira, R., & Smith, M. A. 2015, ApJ, 806, 177

Muno, M. P., et al. 2009, ApJS, 181, 110

Nagata, T., Woodward, C. E., Shure, M., & Kobayashi, N. 1995, AJ, 109, 1676

Nagata, T., Woodward, C. E., Shure, M., Pipher, J. L., & Okuda, H. 1990, ApJ, 351, 83

Nagayama, T., et al. 2003, in Proc. SPIE, 4841, Instrument Design and Performance for Optical/Infrared Ground-based Telescopes, ed. M. Iye & A. F. M. Moorwood (Bellingham, WA: SPIE), 459

Nakanishi, H., & Sofue, Y. 2006, PASJ, 58, 847

Nakaya, H., Komiyama, Y., Kashikawa, N., Uchida, T., Nagayama, T., & Yoshida, M. 2016, in Proc. SPIE, 9915, High Energy, Optical, and Infrared Detectors for Astronomy VII, ed. A. D. Holland & J. Beletic (Bellingham, WA: SPIE), 99151O

Namekata, D., Habe, A., Matsui, H., & Saitoh, T. R. 2009, ApJ, 691, 1525

Nascimbeni, V., et al. 2022, A&A, 658, A31

National Academies of Sciences, Engineering, & Medicine 2021, Pathways to Discovery in Astronomy and Astrophysics for the 2020s (Washington, DC: National Academies Press)

Navarro, M. G., Minniti, D., Pullen, J., & Ramos, R. C. 2020, ApJ, 889, 56

Nazé, Y., & Motch, C. 2018, A&A, 619, A148

Nemravová, J., et al. 2012, A&A, 537, A59

Ness, M., et al. 2013, MNRAS, 430, 836

Ness, M., et al. 2016a, ApJ, 819, 2

Ness, M., Debattista, V. P., Bensby, T., Feltzing, S., Roškar, R., Cole, D. R., Johnson, J. A., & Freeman, K. 2014, ApJ, 787, L19

Ness, M., Hogg, D. W., Rix, H. W., Martig, M., Pinsonneault, M. H., & Ho, A. Y. Q. 2016b, ApJ, 823, 114

Neumayer, N., Seth, A., & Böker, T. 2020, A&AR, 28, 4

Nguyen, D. D., et al. 2019, ApJ, 872, 104

Nicastro, F., Senatore, F., Krongold, Y., Mathur, S., & Elvis, M. 2016, ApJ, 828, L12

Nidever, D. L., et al. 2012, ApJ, 755, L25

Nishiyama, S., et al. 2005, ApJ, 621, L105

Nishiyama, S., et al. 2006, ApJ, 638, 839

Nishiyama, S., et al. 2013, ApJ, 769, L28

Nobukawa, M., Uchiyama, H., Nobukawa, K. K., Yamauchi, S., & Koyama, K. 2016, ApJ, 833, 268

Nogueras-Lara, F., et al. 2018, A&A, 610, A83

Nogueras-Lara, F., et al. 2019, Nature Astron., 4, 377

Nogueras-Lara, F., Schödel, R., & Neumayer, N. 2021, A&A, 653, A133

Nogueras-Lara, F., Schultheis, M., Najarro, F., Sormani, M. C., Gadotti, D. A., & Rich, R. M. 2023, A&A, 671, L10

Nucita, A. A., Licchelli, D., De Paolis, F., Ingrosso, G., Strafella, F., Katysheva, N., & Shugarov, S. 2018, MNRAS, 476, 2962

Oka, T., Tsujimoto, S., Iwata, Y., Nomura, M., & Takekawa, S. 2017, Nature Astron., 1, 709

Okuda, H., et al. 1990, ApJ, 351, 89

Omukai, K. 2001, ApJ, 546, 635

Ona, K., Sakaguchi, N., Ohno, H., & Utsunomiya, S. 2020, Trans. Jpn. Soc. Aeronautical Space Sci. Aerospace Technol. Jpn., 18, 32

Ono, Y., et al. 2023, ApJ, 951, 72

Ortiz, J. L., et al. 2015, A&A, 576, A18

Özel, F., Psaltis, D., Narayan, R., & McClintock, J. E. 2010, ApJ, 725, 1918

Paumard, T., et al. 2006, ApJ, 643, 1011

Penny, M. T., Gaudi, B. S., Kerins, E., Rattenbury, N. J., Mao, S., Robin, A. C., & Calchi Novati, S. 2019, ApJS, 241, 3

Penoyre, Z., Belokurov, V., & Evans, N. W. 2022, MNRAS, 513, 2437

Perets, H. B., & Mastrobuono-Battisti, A. 2014, ApJ, 784, L44

Pérez-Villegas, A., Portail, M., Wegg, C., & Gerhard, O. 2017, ApJ, 840, L2

Perryman, M., Hartman, J., Bakos, G. Á., & Lindegren, L. 2014, ApJ, 797, 14

Petigura, E. A. 2020, AJ, 160, 89

Pettitt, A. R., Dobbs, C. L., Acreman, D. M., & Price, D. J. 2014, MNRAS, 444, 919

Pettitt, A. R., Tasker, E. J., & Wadsley, J. W. 2016, MNRAS, 458, 3990

Pfuhl, O., et al. 2011, ApJ, 741, 108

Plavchan, P., et al. 2020, Nature, 582, 497

Poggio, E., et al. 2021, A&A, 651, A104

Ponti, G., Morris, M. R., Terrier, R., & Goldwurm, A. 2013, in Cosmic Rays in Star-Forming Environments, ed. D. F. Torres & O. Reimer (Berlin: Springer), 331

Ponti, G., Terrier, R., Goldwurm, A., Belanger, G., & Trap, G. 2010, ApJ, 714, 732

Portail, M., Gerhard, O., Wegg, C., & Ness, M. 2017, MNRAS, 465, 1621

Portail, M., Wegg, C., Gerhard, O., & Martinez-Valpuesta, I. 2015, MNRAS, 448, 713

Portegies Zwart, S. F., Baumgardt, H., McMillan, S. L. W., Makino, J., Hut, P., & Ebisuzaki, T. 2006, ApJ, 641, 319

Poulton, C. J., Robitaille, T. P., Greaves, J. S., Bonnell, I. A., Williams, J. P., & Heyer, M. H. 2008, MNRAS, 384, 1249

Predehl, P., et al. 2020, Nature, 588, 227

Purcell, C. W., Bullock, J. S., Tollerud, E. J., Rocha, M., & Chakrabarti, S. 2011, Nature, 477, 301

Queiroz, A. B. A., et al. 2021, A&A, 656, A156

Quillen, A. C., Dougherty, J., Bagley, M. B., Minchev, I., & Comparetta, J. 2011, MNRAS, 417, 762

Ramos, P., Antoja, T., & Figueras, F. 2018, A&A, 619, A72

Rattenbury, N. J., Mao, S., Debattista, V. P., Sumi, T., Gerhard, O., & de Lorenzi, F. 2007, MNRAS, 378, 1165

Rauer, H., et al. 2014, Exp. Astron., 38, 249

Rebull, L. M., Stauffer, J. R., Cody, A. M., Hillenbrand, L. A., Bouvier, J., Roggero, N., & David, T. J. 2020, AJ, 159, 273

Rees, M. J. 1984, ARA&A, 22, 471

Regan, M. W., & Teuben, P. 2003, ApJ, 582, 723

Reid, M. J., et al. 2019, ApJ, 885, 131

Reines, A. E., Greene, J. E., & Geha, M. 2013, ApJ, 775, 116

Renzini, A. 1999, in The Formation of Galactic Bulges, ed. C. M. Carollo et al. (New York: Cambridge University Press), 9

Renzini, A., et al. 2018, ApJ, 863, 16

Revnivtsev, M., Sazonov, S., Churazov, E., Forman, W., Vikhlinin, A., & Sunyaev, R. 2009, Nature, 458, 1142

Revnivtsev, M., Sazonov, S., Gilfanov, M., Churazov, E., & Sunyaev, R. 2006, A&A, 452, 169

Rich, R. M., Ryde, N., Thorsbro, B., Fritz, T. K., Schultheis, M., Origlia, L., & Jönsson, H. 2017, AJ, 154, 239

Ricker, G. R., et al. 2014, in Proc. SPIE, 9143, Space Telescopes and Instrumentation 2014: Optical, Infrared, and Millimeter Wave, ed. J. M. Oschmann, Jr., et al. (Bellingham, WA: SPIE), 914320

Rix, H.-W., et al. 2022, ApJ, 941, 45

Rodler, F., & López-Morales, M. 2014, ApJ, 781, 54

Rodriguez-Fernandez, N. J., & Combes, F. 2008, A&A, 489, 115

Román-Zúñiga, C. G., Elston, R., Ferreira, B., & Lada, E. A. 2008, ApJ, 672, 861

Rybicki, K. A., Wyrzykowski, Ł., Klencki, J., de Bruijne, J., Belczyński, K., & Chruślińska, M. 2018, MNRAS, 476, 2013

Safarzadeh, M., & Spergel, D. N. 2020, ApJ, 893, 21

Sahu, K. C., et al. 2022, ApJ, 933, 83

Sakai, D., Oyama, T., Nagayama, T., Honma, M., & Kobayashi, H. 2023, PASJ, 75, 937

Sanders, J. L., Matsunaga, N., Kawata, D., Smith, L. C., Minniti, D., & Lucas, P. W. 2022, MNRAS, 517, 257

Sanders, J. L., Smith, L., & Evans, N. W. 2019, MNRAS, 488, 4552

Sarkar, K. C., Nath, B. B., & Sharma, P. 2015, MNRAS, 453, 3827

Satyapal, S., Böker, T., Mcalpine, W., Gliozzi, M., Abel, N. P., & Heckman, T. 2009, ApJ, 704, 439

Schiavon, R. P. 2007, ApJS, 171, 146

Schiavon, R. P., et al. 2017, MNRAS, 465, 501

Schive, H.-Y., Chiueh, T., & Broadhurst, T. 2014, Nature Phys., 10, 496

Schlichting, H. E., Ofek, E. O., Wenz, M., Sari, R., Gal-Yam, A., Livio, M., Nelan, E., & Zucker, S. 2009, Nature, 462, 895

Schneider, F. R. N., et al. 2014, ApJ, 780, 117

Schödel, R., et al. 2023, arXiv:2310.11912

Schödel, R., Merritt, D., & Eckart, A. 2009, A&A, 502, 91

Schönrich, R., Aumer, M., & Sale, S. E. 2015, ApJ, 812, L21

Schönrich, R., & Dehnen, W. 2018, MNRAS, 478, 3809

Schultheis, M., et al. 2021, A&A, 650, A191

Secchi, A. 1866, Astron. Nachr., 68, 63

Secrest, N. J., et al. 2015, ApJ, 798, 38

Secrest, N. J., Satyapal, S., Gliozzi, M., Cheung, C. C., Seth, A. C., & Böker, T. 2012, ApJ, 753, 38

Sellwood, J. A. 2011, MNRAS, 410, 1637

Sellwood, J. A., & Binney, J. J. 2002, MNRAS, 336, 785

Sellwood, J. A., & Masters, K. L. 2022, ARA&A, 60, 73

Seo, W.-Y., Kim, W.-T., Kwak, S., Hsieh, P.-Y., Han, C., & Hopkins, P. F. 2019, ApJ, 872, 5

Shen, J., Rich, R. M., Kormendy, J., Howard, C. D., De Propris, R., & Kunder, A. 2010, ApJ, 720, L72

Shen, Y., et al. 2015, ApJ, 805, 96

Sheth, K., et al. 2008, ApJ, 675, 1141

Shibuya, T., Ouchi, M., & Harikane, Y. 2015, ApJS, 219, 15

Shibuya, T., Ouchi, M., Harikane, Y., & Nakajima, K. 2019, ApJ, 871, 164

Shikauchi, M., Tanikawa, A., & Kawanaka, N. 2022, ApJ, 928, 13

Shlosman, I., Frank, J., & Begelman, M. C. 1989, Nature, 338, 45

Showman, A. P., Wordsworth, R. D., Merlis, T. M., & Kaspi, Y. 2013, in Comparative Climatology of Terrestrial Planets, Part II, ed. S. J. Mackwell et al. (Tucson: University of Arizona Press), 277

Simon, J. D., & Geha, M. 2007, ApJ, 670, 313

Skowron, D. M., et al. 2019, Science, 365, 478

Skrutskie, M. F., et al. 2006, AJ, 131, 1163

Skumanich, A. 1972, ApJ, 171, 565

Smith, L. C., et al. 2018, MNRAS, 474, 1826

Smith, M. A. 2019, PASP, 131, 044201

Snellen, I. A. G., de Kok, R. J., le Poole, R., Brogi, M., & Birkby, J. 2013, ApJ, 764, 182

Sofue, Y., & Handa, T. 1984, Nature, 310, 568

Sormani, M. C., et al. 2022, MNRAS, 512, 1857

Sormani, M. C., Binney, J., & Magorrian, J. 2015, MNRAS, 454, 1818

Sormani, M. C., Sobacchi, E., Fragkoudi, F., Ridley, M., Treß, R. G., Glover, S. C. O., & Klessen, R. S. 2018, MNRAS, 481, 2

Sormani, M. C., Tress, R. G., Glover, S. C. O., Klessen, R. S., Battersby, C. D., Clark, P. C., Hatchfield, H. P., & Smith, R. J. 2020, MNRAS, 497, 5024

Spergel, D., et al. 2015, arXiv:1503.03757

Stassun, K. G., et al. 2019, AJ, 158, 138

Steinmetz, M., et al. 2006, AJ, 132, 1645

Stolte, A., et al. 2014, ApJ, 789, 115

Takada, M., et al. 2014, PASJ, 66, R1

Takekawa, S., Oka, T., Iwata, Y., Tsujimoto, S., & Nomura, M. 2020, ApJ, 890, 167

Tan, X., & Showman, A. P. 2021, MNRAS, 502, 2198

Tanikawa, A., Hattori, K., Kawanaka, N., Kinugawa, T., Shikauchi, M., & Tsuna, D. 2023, ApJ, 946, 79

Tanikawa, A., & Umemura, M. 2014, MNRAS, 440, 652

Tavrov, A., et al. 2018, J. Astron. Telesc. Instrum. Syst., 4, 044001

Taylor, P., & Kobayashi, C. 2014, MNRAS, 442, 2751

Tepper-Garcia, T., et al. 2021, arXiv:2111.05466

Thao, P. C., et al. 2020, AJ, 159, 32

The LUVOIR Team 2019, arXiv:1912.06219

Thompson, T. A., et al. 2019, Science, 366, 637

Tinetti, G., et al. 2018, Exp. Astron., 46, 135

Toguz, F., Kawata, D., Seabroke, G., & Read, J. I. 2022, MNRAS, 511, 1757

Toki, S., & Takada, M. 2021, arXiv:2103.13015

Torrealba, G., et al. 2019, MNRAS, 488, 2743

Tremaine, S. D., Ostriker, J. P., & Spitzer, L. J. 1975, ApJ, 196, 407

Tsuboi, M., Inoue, M., Handa, T., Tabara, H., & Kato, T. 1985, PASJ, 37, 359

Tsuboi, M., Kitamura, Y., Tsutsumi, T., Miyawaki, R., Miyoshi, M., & Miyazaki, A. 2019, PASJ, 71, 105

Tsuboi, M., Kitamura, Y., Tsutsumi, T., Uehara, K., Miyoshi, M., Miyawaki, R., & Miyazaki, A. 2017, ApJ, 850, L5

Tsuboi, M., Tsutsumi, T., Miyazaki, A., Miyawaki, R., & Miyoshi, M. 2022, PASJ, 74, 738

Tsujimoto, M., Morihana, K., Hayashi, T., & Kitaguchi, T. 2018, PASJ, 70, 109

Tsujimoto, T., & Baba, J. 2020, ApJ, 904, 137

Tu, L., Johnstone, C. P., Güdel, M., & Lammer, H. 2015, A&A, 577, L3

Umeda, H., Hosokawa, T., Omukai, K., & Yoshida, N. 2016, ApJ, 830, L34

Valinia, A., & Marshall, F. E. 1998, ApJ, 505, 134

van Dokkum, P., Conroy, C., Villaume, A., Brodie, J., & Romanowsky, A. J. 2017, ApJ, 841, 68

van Leeuwen, F. 2007, A&A, 474, 653

Volonteri, M. 2010, A&AR, 18, 279

Volonteri, M., et al. 2020, MNRAS, 498, 2219

Vos, J. M., et al. 2020, AJ, 160, 38

Walcher, C. J., Böker, T., Charlot, S., Ho, L. C., Rix, H. W., Rossa, J., Shields, J. C., & van der Marel, R. P. 2006, ApJ, 649, 692

Wang, F., et al. 2021, ApJ, 907, L1

Ward, J. L., Kruijssen, J. M. D., & Rix, H.-W. 2020, MNRAS, 495, 663

Wegg, C., & Gerhard, O. 2013, MNRAS, 435, 1874

Weinberg, M. D. 1985, MNRAS, 213, 451

WFIRST Astrometry Working Group 2019, J. Astron. Telesc. Instrum. Syst., 5, 044005

Wielen, R., Fuchs, B., & Dettbarn, C. 1996, A&A, 314, 438

Willman, B., et al. 2005, ApJ, 626, L85

Woods, T. E., et al. 2019, Publ. Astron. Soc. Australia, 36, e027

Woods, T. E., Heger, A., & Haemmerlé, L. 2020, MNRAS, 494, 2236

Worrall, D. M., Marshall, F. E., Boldt, E. A., & Swank, J. H. 1982, ApJ, 255, 111

Wozniak, H. 2007, A&A, 465, L1

Wozniak, H., & Michel-Dansac, L. 2009, A&A, 494, 11

Wright, N. J., & Mamajek, E. E. 2018, MNRAS, 476, 381

Wylie, S. M., Clarke, J. P., & Gerhard, O. E. 2022, A&A, 659, A80

Wylie, S. M., Gerhard, O. E., Ness, M. K., Clarke, J. P., Freeman, K. C., & Bland-Hawthorn, J. 2021, A&A, 653, A143

Yamaguchi, M. S., Kawanaka, N., Bulik, T., & Piran, T. 2018a, ApJ, 861, 21

Yamaguchi, M. S., Yano, T., & Gouda, N. 2018b, MNRAS, 474, 4756

Yamauchi, S., Ebisawa, K., Tanaka, Y., Koyama, K., Matsumoto, H., Yamasaki, N. Y., Takahashi, H., & Ezoe, Y. 2009, PASJ, 61, S225

Yang, H., et al. 2015, ApJ, 798, L13

Yang, J., et al. 2020, ApJ, 897, L14

Yang, J., Cowan, N. B., & Abbot, D. S. 2013, ApJ, 771, L45

Yanny, B., et al. 2009, AJ, 137, 4377

Yu, Q., & Tremaine, S. 2003, ApJ, 599, 1129

Yuasa, T., Makishima, K., & Nakazawa, K. 2012, ApJ, 753, 129

Zasowski, G., et al. 2019, ApJ, 870, 138

Zasowski, G., Ness, M. K., García Pérez, A. E., Martinez-Valpuesta, I., Johnson, J. A., & Majewski, S. R. 2016, ApJ, 832, 132

Zhang, H., & Sanders, J. L. 2023, MNRAS, 521, 1462

Zhao, G., Zhao, Y.-H., Chu, Y.-Q., Jing, Y.-P., & Deng, L.-C. 2012, Res. Astron. Astrophys., 12, 723

Zheng, Z., et al. 2014, ApJ, 785, L23

Zucker, D. B., et al. 2006, ApJ, 643, L103